UNIVERSITAT DE BARCELONA

Optimization and degradation of supercapacitors in aqueous and super-concentrated "water-in-salt" electrolytes

José Miguel Delgado Galindo

Doctoral Thesis

Optimization and degradation of supercapacitors in aqueous and super-concentrated "water-in-salt" electrolytes

Author

José Miguel Delgado Galindo

Directors

Dr. Jordi Jacas Biendicho

Prof. Joan Ramon Morante Lleonart

UNIVERSITAT DE BARCELONA

Optimización y degradación de supercapacitores en electrolitos acuosos y superconcentrados “water-in-salt”

Programa de doctorado en Nanociencias

Autor: José Miguel Delgado Galindo

Directores: Dr. Jordi Jacas Biendicho
Prof. Joan Ramon Morante Lleonart

Tutor: Prof. Joan Ramon Morante Lleonart

Institut de Recerca en Energia de Catalunya (IREC)

UNIVERSITAT DE BARCELONA

A mi familia

por su amor y apoyo incondicional

Agradecimientos

Quiero aprovechar estas líneas para dar las gracias a todas las personas que me han ayudado y brindado su apoyo durante el proceso de gestación de esta tesis. Ha sido un largo y lento camino de aprendizaje, investigación y asimilación de conocimientos, no exento de contratiempos, dificultades y altibajos, hasta llegar finalmente a este momento.

Quiero agradecer a mis directores de tesis por darme la oportunidad de llevarla a cabo, proporcionarme los medios materiales, y también, lo más importante, por compartir su conocimiento y consejo, sin los cuales no habría podido llegar a buen puerto.

A mis compañeros de IREC por su inestimable ayuda y paciencia ¡gracias! Siempre habéis estado disponibles para resolver cualquier duda, dándome siempre ánimos y apoyo durante el proceso de redacción de esta tesis. Gracias por los buenos momentos que hemos pasado juntos trabajando dentro de IREC o más relajadamente en nuestros encuentros fuera de él, que han hecho que nos conozcamos mejor creando vínculos de amistad.

Finalmente, quiero agradecer a mi familia por haber estado siempre ahí, animándome y brindándome su apoyo en todo momento, por ser mi revulsivo en los momentos de desánimo y, sobre todo, por hacerme sentir todo su amor y cariño.

Contents

Summary

Supercapacitors are electrochemical energy storage devices. Its energy comes from the electrostatic accumulation of ionic charge on the surface of an electrode, compensated by an opposite electrical charge on the inner surface of the electrode, for this reason they are also called electrochemical double layer capacitors. Since no chemical reactions are involved, these devices can be charged and discharged rapidly. This makes them ideal for high-power applications such as powering camera flashes, starting engines, or managing power peaks in electrical grids. They are also used for energy recovery in regenerative braking systems of trains or electric vehicles. Although capacitors provide great power, their energy density is an order of magnitude lower than that of batteries, which limits their extensive use.

One of the objectives of this thesis is to increase the energy, power, and energy efficiency of capacitors based on activated carbon electrodes in aqueous electrolytes. To this end, different strategies have been addressed to increase capacitance and voltage, which are directly related to the increase in energy, as well as to reduce resistance, which is related to performance and lifespan.

Using the aqueous electrolyte 1 M KOH, the following aspects have been studied: 1) optimizing the mass balance between the positive and negative electrodes to improve energy efficiency and cycle life, 2) thermally treating the electrodes at temperatures below the melting point of the binder to increase energy, 3) investigating the impact of two membranes, fibreglass, and polypropylene, on rate-capacitance performance. Optimizations conducted in Chapter 3 using YP50 as electrode show that the positive to negative mass ratio should be adjusted to 0.6, the thermal treatment should be set to 240 ºC, and fibreglass membranes should be used to achieve a better capacitor response.

In Chapter 4, we used super-concentrated aqueous solutions based on potassium acetate, called "water-in-salt" electrolytes, to increase the voltage of the devices. Concentrations from 1 m to 32 m (mol/Kg) have been studied, verifying an increase in the potential window up to 1.8 V and finding a compromise between capacitance, rate capability, cycle life, and cost for the 27 m KAc electrolyte. The use of the 27 m KAc electrolyte showed a capacitance of 26.3 F/g and 19.6 F/g when increasing the scan rate from 5 to 100 mV/s, with a retention of 74.5%, a capacitance of 13 F/g over 10,000 charge cycles at 1 A/g, and the estimated electrolyte cost was €4.42 to produce 1,000 cells.

In chapter 6 we prepared hybrid capacitors, composed of a capacitive activated carbon electrode and a faradaic electrode using lithium oxides. Lithium titanium oxide (LTO), commonly used as anode for its well-defined phase transition around 1.6 V vs Li/Li^+, was used as the negative electrode and YP50 as the positive. Lithium iron phosphate (LFP), commonly used as cathode for its well-defined phase transition around 3.5 V vs Li/Li^+, was used as the positive electrode and YP50 as the negative. The YP50/LTO capacitor with the 1 M $LiPF_6$ organic electrolyte showed a high capacitance of 30.2 F/g at a low rate of 0.6 mV/s and 7.7 F/g at a medium rate of 20 mV/s in a potential window of 2 V. The LFP/YP50 capacitor showed with the organic electrolyte 1 M $LiPF_6$ a capacitance of 20.9 F/g at a low rate of 0.1 mV/s and 8.7 F/g at a medium rate of 20 mV/s in a potential window of 2.9 V and with the super-concentrated water-in-salt electrolyte 32 m KAc + 6 m LiAc it showed a very high capacitance of 52.4 F/g at 0.1 mV/s and 13.3 F/g at 10 mV/s in a potential window of 1.8 V.

The other objective of this thesis, discussed in chapter 5, is the study of degradation mechanisms involving irreversible reactions in aqueous capacitor components, which reduce its performance. These mechanisms are accelerated by operating conditions such as temperature, humidity, and working potential window. We studied the degradation mechanism of activated carbon capacitors in two aqueous electrolytes: super-concentrated "water-in-salt" 27 m KAc and dilute 1 M KOH. To accelerate their degradation, we have performed an electrochemical characterization of the cells by means of a series of 10,000 charge and discharge cycles at 1 A/g in a potential window of 2 V, which, being larger than the stability window of the electrolytes, ensures a rapid degradation. Once the cells were degraded, we proceeded to disassemble and study with SEM, EDS, FTIR, XRD and XPS methods.

A reassembly of the cells with 27 m KAc was also performed after degradation, changing the electrolyte and the membrane and maintaining the electrodes and current collectors, cycled again and studied with the method of failure mode and effects analysis (FMEA) to identify and evaluate the potential failure modes, analyse their causes and its severity and create strategies to mitigate them. The main failure modes analysed are related to the decomposition of the electrolytes, leading to water splitting and the generation of hydrogen and oxygen. Oxygen would oxidize the current collectors and the electrodes, increasing the resistance and reducing the electrical conductivity and capacitance. The oxidation of the activated carbon electrodes would generate CO_2, which together with O_2 and H_2 would block the pores of the electrodes, making electrical contact difficult and reducing capacitance. The decomposition of the electrolytes would limit their stability and cause their precipitation on the electrodes, as well as decomposition of the electrode binder with loss of cohesion.

Resumen

Los supercapacitores son dispositivos de almacenamiento de energía electroquímica. Su energía proviene de la acumulación electrostática de carga iónica en la superficie de un electrodo, compensada por una carga eléctrica opuesta en la superficie interna del electrodo, por lo que también se les llama capacitores de doble capa electroquímica. Dado que no hay reacciones químicas involucradas, estos dispositivos pueden cargarse y descargarse rápidamente. Esto los hace ideales para aplicaciones de alta potencia, como alimentar flashes de cámara, arrancar motores o gestionar picos de energía en redes eléctricas. También se utilizan para la recuperación de energía en sistemas de frenado regenerativo de trenes o vehículos eléctricos. Aunque los capacitores proporcionan una gran potencia, su densidad de energía es un orden de magnitud menor que la de las baterías, lo que limita su uso extensivo.

Uno de los objetivos de esta tesis es aumentar la energía, la potencia y la eficiencia energética de los capacitores basados en electrodos de carbón activado en electrolitos acuosos. Para ello, se han abordado diferentes estrategias para aumentar la capacitancia y el voltaje, que están directamente relacionados con el aumento de energía, así como para reducir la resistencia, relacionada con el rendimiento y la vida útil.

Usando el electrolito acuoso 1 M KOH, se han estudiado los siguientes aspectos: 1) optimización del balance de masa entre los electrodos positivo y negativo para mejorar la eficiencia energética y la vida útil, 2) tratamiento térmico de los electrodos a temperaturas por debajo del punto de fusión del aglutinante para aumentar la energía, 3) investigación del impacto de dos membranas, fibra de vidrio y polipropileno, en el rendimiento de la capacitancia a altas tasas de escaneo. Las optimizaciones realizadas en el Capítulo 3 utilizando YP50 como electrodo muestran que la relación de masa entre el electrodo positivo y negativo debe ajustarse a 0.6, el tratamiento térmico debe establecerse a 240 ºC, y se deben utilizar membranas de fibra de vidrio para lograr una mejor respuesta del capacitor.

En el Capítulo 4, utilizamos soluciones acuosas superconcentradas a base de acetato de potasio, denominadas electrolitos “water-in-salt”, para aumentar el voltaje de los dispositivos. Se estudiaron concentraciones desde 1 m hasta 32 m (mol/Kg), verificando un aumento en la ventana de potencial de hasta 1.8 V y encontrado un compromiso entre capacitancia, capacidad de respuesta, vida útil y costo para el electrolito de 27 m KAc. El uso del electrolito de 27 m KAc mostró una capacitancia de 26.3 F/g y 19.6 F/g al aumentar la velocidad de escaneo de 5 a

100 mV/s, con una retención del 74.5 %, una capacitancia de 13 F/g durante 10,000 ciclos de carga a 1 A/g, y un costo estimado del electrolito de 4.42 € para producir 1,000 celdas.

En el Capítulo 6, preparamos capacitores híbridos, compuestos por un electrodo capacitivo de carbón activado y un electrodo faradaico utilizando óxidos de litio. El óxido de litio y titanio (LTO), comúnmente utilizado como ánodo por su transición de fase bien definida alrededor de 1.6 V vs Li/Li^+, se utilizó como electrodo negativo y YP50 como electrodo positivo. El fosfato de hierro y litio (LFP), generalmente utilizado como cátodo por su transición de fase bien definida alrededor de 3.5 V vs Li/Li^+, se utilizó como electrodo positivo y YP50 como electrodo negativo. El capacitor YP50/LTO con el electrolito orgánico 1 M $LiPF_6$ mostró una alta capacitancia de 30,2 F/g a una baja velocidad de 0,6 mV/s y 7,7 F/g a una velocidad media de 20 mV/s en una ventana de potencial de 2 V. El capacitor LFP/YP50, con el electrolito orgánico 1 M $LiPF_6$, mostró una capacitancia de 20,9 F/g a una baja velocidad de 0,1 mV/s y 8,7 F/g a una velocidad media de 20 mV/s en una ventana de potencial de 2,9 V. Con el electrolito superconcentrado “water-in-salt” 32 m KAc + 6 m LiAc, mostró una capacitancia muy alta de 52,4 F/g a 0,1 mV/s y 13,3 F/g a 10 mV/s en una ventana de potencial de 1,8 V.

El otro objetivo de esta tesis, discutido en el capítulo 5, es el estudio de los mecanismos de degradación que involucran reacciones irreversibles en los componentes de capacitores acuosos, las cuales reducen su rendimiento. Estos mecanismos se ven acelerados por condiciones operativas como la temperatura, la humedad y la ventana de potencial de trabajo. Se estudió el mecanismo de degradación de capacitores de carbón activado en dos electrolitos acuosos: el electrolito superconcentrado "water-in-salt" 27 m KAc y el electrolito diluido 1 M KOH. Para acelerar su degradación, realizamos una caracterización electroquímica de las celdas mediante series de 10,000 ciclos de carga y descarga a 1 A/g en una ventana de potencial de 2 V, la cual, al ser mayor que la ventana de estabilidad de los electrolitos, asegura una degradación rápida. Una vez degradadas las celdas, procedimos a su desensamblaje y estudio utilizando SEM, EDS, FTIR, XRD y XPS.

Después de la degradación, las celdas con el electrolito 27 m KAc fueron reensambladas cambiando el electrolito y la membrana, pero manteniendo los electrodos y los colectores de corriente. Las celdas se ciclaron nuevamente y se estudiaron utilizando el método de análisis modal de fallos y efectos (FMEA) para identificar y evaluar los posibles modos de fallo, analizar sus causas y su gravedad, y desarrollar estrategias de mitigación. Los principales modos de fallo identificados estuvieron relacionados con la descomposición de los electrolitos, lo que lleva a la división del agua y a la generación de hidrógeno y oxígeno. El oxígeno oxidaría los colectores de corriente y los electrodos, aumentando la resistencia y reduciendo la conductividad eléctrica y la capacitancia. La oxidación de los electrodos de carbón activado produciría CO_2, que, junto con el O_2 y el H_2 bloquearía los poros de los electrodos, dificultando el contacto eléctrico y disminuyendo la capacitancia. La descomposición de los electrolitos también limitaría su estabilidad, causando precipitación sobre los electrodos, así como degradando el aglutinante de los electrodos, lo que llevaría a una pérdida de cohesión de los mismos.

1 Introduction

1.1 Electricity and its early forms of storage

Knowledge of the effects of electricity dates back to the beginning of history. In ancient Egyptian texts dating back more than 4,500 years, the numbing effects of electric fish discharges were already described. About 2,600 years ago, in ancient Greece, Thales of Miletus discovered static electricity. He generated electrostatic charges by rubbing a piece of amber (*ἤλεκτρον* or *elektron* in ancient Greek) with a cloth.

The first battery, the so-called Baghdad battery, dates to the time of the Parthians at the beginning of the 3rd century AD. The device consists of a terracotta pot containing a copper cylinder, which houses an iron rod and filled with acid. During the 20th century, various reproductions were performed using an electrolyte made with grape juice or a mixture of vinegar and quinones naturally produced by beetles, obtaining a voltage between one and two volts. Other reproductions were also used for electroplating.

In 1600 William Gilbert built the first electroscope, an instrument capable of measuring the influence of electrical charge on light objects such as amber when rubbed with a wool cloth. To name this effect, he relied on the Greek name for amber, e*lektron*, to create the term *electricus* which means “like amber”. Otto von Guericke invented in 1663 the first electrostatic generator that was capable of storing electrical charges and producing sparks. In 1729 Stephen Gray, while studying static electricity, realised that it could be conducted through some materials. He classified the materials into conductive and non-conductive or insulating materials. In 1733, Charles du Fay was the first to realise that there were two types of electrical charges which he called vitreous charge and resinous charge, which we now call positive and negative. The vitreous charge was formed by rubbing the glass with a silk cloth and the resinous one by rubbing, with a skin, certain resinous substances like amber. Du Fay observed that objects charged with the same type of electricity repel each other, while objects charged with different types of electricity attract each other [1].

Experiments with static electricity led to the fabrication of different devices that ended with the construction by the German physicist E.G. von Kleist in 1745 of what is considered the *first electric capacitor* in history. A Dutch professor at the Leiden university made a similar device, which is why it is known as the Leiden jar. It consists of a glass bottle into which a metal foil connects to the outside using a metal nail. Holding the bottle with one hand and touching the nail with an electrostatically charged object, the charges pass into the bottle, leaving it loaded. Later, another metallic sheet was placed on the outside of the bottle, thus avoiding having to take it by hand. Experiments with the Leiden bottle led to connecting them in various arrangements. Benjamin Franklin called these arrangements an *electrical battery* in a case similar to the arrangement of a cannon battery (Figure 1.1). Franklin was the first to use the terms *positive* and *negative* for electricity and discovered the principle of *charge conservation*. Alessandro Volta called these devices *"condensatore di elettricità"* which is why capacitors are known as *"condensers"* [2].

Figure 1.1 A battery of four Leiden jars. Boerhaave Museum, Leiden (Wikimedia commons)

We must wait until 1800, at the dawn of the Contemporary Age, to see the *first battery* as we understand it today, the voltaic pile of Alessandro Volta. The device consists of alternating zinc and copper discs separated by cardboard or felt and impregnated with brine; it is stacked in series, increasing the tension at will. In the voltaic pile, the metallic zinc dissolves into the electrolyte (oxidation) in the ion form, Zn^{2+}, and the electrons (e^-) travel through the cable that closes the circuit to the copper disk where two protons (H^+) of the electrolyte absorb them (reduction) forming hydrogen gas (H_2) that is released to the atmosphere [3].

In the following years, all kinds of tests were carried out with different combinations of metals, electrolytes and separators arranged in the most varied forms, being the most important the Daniell cell in 1836. The Daniel cell uses two liquid electrolytes, zinc sulphate with a zinc plate and copper sulphate with a copper plate, separated by a porous jar. The plates act as electrodes and are connected by a wire. In this combination, the Cu^{2+} ions absorb the electrons, avoiding hydrogen production of Volta pile, being the first battery used in practical applications to provide electricity to telegraphs [3].

Since the 19th century, two kinds of devices capable of storing and supplying electricity were developed. The condensers are based on the accumulation of electrostatic charges and are today called capacitors. The voltaic piles can transform chemical energy into electricity and are today known as batteries.

1.2 Historical development of capacitors

We refer to *capacity* as the ability of capacitors to store electrical charges. Capacitance, which is measured in farads (F) in honour of Michael Faraday, who studied electromagnetism and electrochemistry during the first half of the 19th century, is the maximum capacity. A capacitor charged with an amount of electricity equal to one coulomb (C) and having an electric potential difference of 1 volt (V) between its plates has a capacity of one farad. One coulomb is the charge obtained with 6.24×10^{18} electrons.

The first electrostatic capacitors consisted of metal plates that internally and externally lined a glass bottle that served as an insulator, like the Leiden jar. Ceramics, paper, and mica were tested as insulators and different arrangements were used. Paper capacitors, in which a paper sheet separated the metal plates and then rolled into a cylinder, had a capacity close to a nano farad (nF).

Later, aluminium plates were separated by an electrolyte with a noticeable increase in capacitance. These types of devices were called *wet capacitors*, the origin of *electrolytic capacitors*. A great improvement was obtained in the mid-1920s when the metal plates were covered with an electrochemically formed insulating film, being called *dry capacitors* due to the low amount of water required for the electrolyte, reaching capacities of a few microfarads (µF). Numerous tests were done with different metals, and a paper separator impregnated with the electrolyte was used to reduce the distance between the plates. In modern *electrolytic capacitors*, the dielectric film is achieved by creating an insulating oxide layer on the positive electrode (anode) by anodisation [4]. The dielectric layer would be similar to the solid electrolyte interphase (SEI) of lithium batteries but without allowing the electrolyte ions to intercalate in it [5]. Dielectric film is in contact with a paper soaked with the electrolyte. The electrolyte and the plate without the insulating layer form the negative electrode (cathode). Although solid electrolytes were discovered by Michael Faraday in 1834, the first commercial applications in capacitors had to wait until the early 1950s [6]. Aqueous electrolytes became popular in the 1980s to reduce costs. Modern electrolytic capacitors may have capacitances reaching a few farads (F).

An important breakthrough was made in the 1950s when H.I. Becker patented *"a new low-voltage electrolytic capacitor"* (Figure 1.2). He used activated charcoal electrodes immersed in an electrolyte of ammonium salts or diluted sulphuric acid that, unlike electrolytic capacitors, did not need an insulating oxide coating and had a capacitance of 6 F. This high capacitance was attributed to the large specific surface area offered by the activated carbons used since they are a very porous material. NEC (under license of SOHIO) fabricated the first commercial device in 1978, used for computer memory backup, and gave it the current name of supercapacitor. In 1982, the Pinnacle Research Institute (PRI) developed the first pseudocapacitor, called the ultracapacitor, for military use by incorporating metal oxides into carbon electrodes, and achieving an energy density of 0.6 Wh/Kg and a power density of 200 W/Kg [7]. Supercapacitors can deliver energy densities of 10 Wh/kg and power densities up to 10 kW/kg, while batteries typically exceed 300 Wh/kg in energy density but have lower power densities, below 1 kW/kg [8]. Pseudocapacitors, with energy densities exceeding 100 Wh/Kg and power densities between 1-10 Kw/Kg, are placed between supercapacitors and batteries in terms of performance [9].

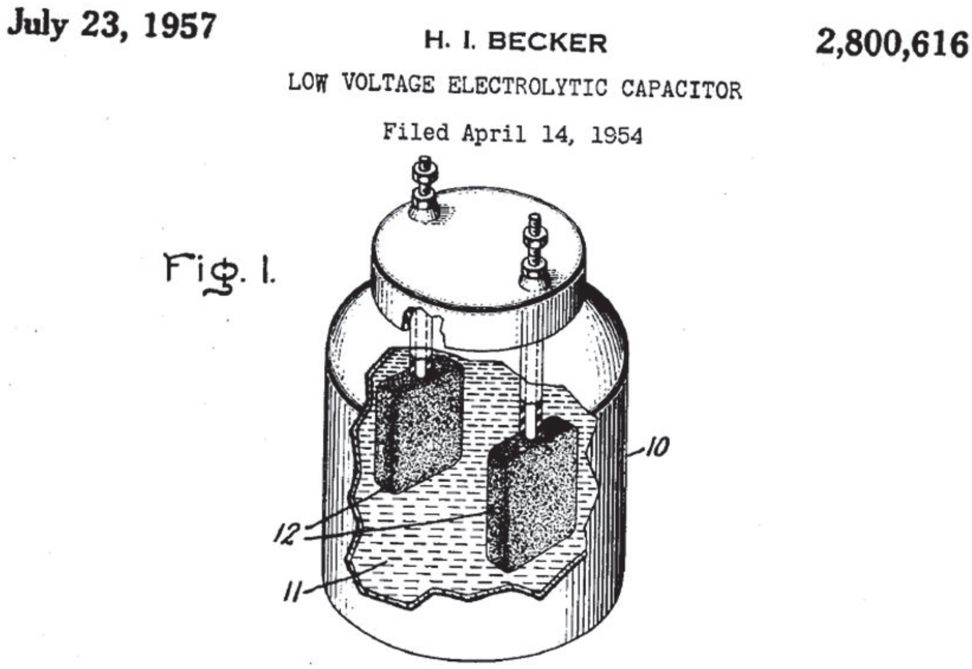

Figure 1.2 First supercapacitor [10].

1.3 Electrostatic capacitors

Electrostatic capacitors are characterized by a very fast response (high power) and low capacitance, which is why they are used as filters. Its operation is based on the accumulation of electric charges of opposite signs in two conductive plates facing each other and separated by a dielectric material by applying a potential difference between them. In physics, capacitors are classified according to their capacitance (C), which is equal to the charge (Q) divided by the potential (V) (Eq. 1.1).

$$C = \frac{Q}{V} \qquad \text{(Eq. 1.1)}$$

The capacitance of an electrostatic capacitor (Figure 1.3) is also defined as the product of the permittivity of the medium between the plates (ε) multiplied by their area (A) and divided by the distance that separates them (d) (Eq. 1.2).

$$C = \varepsilon \frac{A}{d} \qquad \text{(Eq. 1.2)}$$

This formula is usually given related to the permittivity of the vacuum $\varepsilon_0 = 8{,}85 \times 10^{-12}$ F/m and the relative permittivity (ε_r) of the dielectric material between electrodes (Eq. 1.3). A high permittivity allows the capacitor to store more electrical charge at a lower potential.

$$C = \varepsilon_0 \varepsilon_r \frac{A}{d} \qquad \text{(Eq. 1.1)}$$

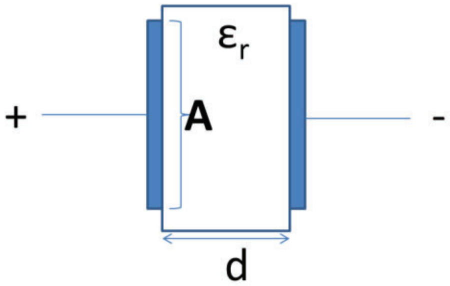

Figure 1.3 Scheme of an electrostatic capacitor.

An electrostatic capacitor can be represented as an electrical circuit with a resistor (R) and a capacitor (C) in series (Figure 1.4). Applying Kirchhoff's first law, which says that the sum of the currents that enter or leave the capacitor and the resistance must be equal but with the opposite sign, we have.

$$C\frac{dV}{dt} + \frac{V}{R} = 0 \qquad \text{(Eq. 1.2)}$$

$$V = V_{\circ}\ e^{-\frac{t}{RC}} \qquad \text{(Eq. 1.3)}$$

Showing that the voltage decay is exponential. The time constant, $\tau = RC$, is the time required for the potential to decay to a value V_0/e. The resistance is usually called equivalent series resistance (ESR) and is related to the loss of energy in an electronic circuit.

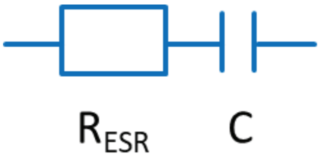

Figure 1.4. RC equivalent circuit of a capacitor.

The work done by increasing the electric charge from zero to its final value Q is given by.

$$W = \int_0^Q V\,dq = \frac{1}{C}\int_0^Q q\,dq = \frac{1}{2}\frac{Q^2}{C} = \frac{1}{2}CV^2 \qquad \text{(Eq. 1.4)}$$

The power of a capacitor is the amount of work done per unit of time.

$$P = \frac{W}{t} \qquad \text{(Eq. 1.5)}$$

1.4 Supercapacitors

Supercapacitors, also known as electrochemical capacitors, electric double-layer capacitors, ultracapacitors, or high-capacity capacitors, are energy storage electronic devices that have gained significant importance in recent years due to their ability to store large amounts of electrical energy in a short period of time and release it very quickly, which means that they are ideal devices to delivering high power. This high power is justified by its low equivalent series resistance (ESR), which translates into a very small time constant (charge time) and a very high life expectancy (more than one million cycles).

Supercapacitors are similar to electrostatic capacitors, where the dielectric material is replaced by a membrane soaked in an electrolyte. It allows the accumulation of an ion layer on each electrode. Its operation can be explained similarly to electrostatic capacitors, but assuming we have two capacitors connected in series and the total capacitance of the device is given by:

$$\frac{1}{C} = \frac{1}{C_1} + \frac{1}{C_2} \qquad \text{(Eq. 1.6)}$$

In supercapacitors, we assume that ESR is mainly due to the opposition of an electrolyte to the free flow of ions when a voltage is applied between the electrodes. It depends on its viscosity and ionic conductivity. It also depends on contributions of the cables, the current collector and the electrode-electrolyte interface [11].

Electrolytes are in charge of supplying the ions that intervene in the reactions that take place in the electrodes, either their simple accumulation as in supercapacitors, or their intervention in faradaic reactions as in pseudocapacitors. Electrolytes are also responsible for the transport and exchange of ions between the electrodes of batteries. Additionally, the type of electrolyte used is also responsible for the amplitude of the potential window, which is the most important parameter to determine the available energy, as reflected in formula 1.4.

Aqueous electrolytes have high ionic conductivity, are cheap and environmentally friendly. When compared to organic electrolytes, aqueous electrolytes have higher capacitance values because the dielectric constant of water is one of the highest, $\varepsilon \approx 80$, although its energy density is low due to its small potential window. Water splitting, that occurs for pure water at 1.23 V, limits the cell voltage to less than 1.5 V. Expansion of the potential window can be accomplished using water-in-salt electrolytes, asymmetric devices, or neutral electrolytes [12]. The use of aqueous electrolytes is also limited by their melting and boiling points, which restrict the range of temperatures at which they can be used [13].

Organic electrolytes can reach potential values of 2.7 V, thereby achieving greater energy density than aqueous electrolytes, but are expensive, potentially more polluting, and having lower ionic conductivity and lower dielectric constant, they have lower capacitance. Organic electrolytes must avoid traces of water, so they require special equipment for handling, which greatly increases their cost and difficulty of use [12], [13].

The stability of electrolytes is also crucial when selecting them to extend the lifespan of the devices. The stability of organic electrolytes is severely compromised by the presence of contaminants or traces of water molecules, while aqueous electrolytes show instability near their freezing temperature [14].

Supercapacitors use a dielectric material to separate the electrodes and avoid a short circuit. Usually, this separator is a porous membrane soaked with the electrolyte and permeable to the passage of the ions. When a potential difference is applied between the electrodes, the inner part of its surface is electrostatically charged, attracting, and adsorbing the ions of the opposite sign in the electrolyte. If the ions are stored and do not react with the electrodes, a physisorption phenomenon occurs, and the device is called an electrochemical double-layer capacitor (EDLC). EDLCs usually use electrodes made with activated carbon (AC) that are highly valued for their large specific surface area (SSA), which is achieved by their huge porosity, reaching in some cases up to 2000 m^2 / g [15]. The electrolyte ions fill the pores very close to the surface, at a molecular size distance, forming an electrical double layer with the electrons accumulated on the surface of the electrodes. The high surface area and the small width of the double layer increase the capacitance to values several orders of magnitude higher than electrostatic capacitors [13], [15].

1.4.1 Historical approach of double layer

In 1853, H. Helmholtz gave the first explanation of the electric double-layer [16], [17] for solid electrodes placed face to face and separated by air or a dielectric material. It was in 1879 [18] when he explained the effect of electrodes immersed in an electrolyte where ionic charges can move freely. These charges are attracted by the electrodes, accumulate, and attach to their surface at a fixed distance. Consequently, counterions are repelled towards the other electrode. Between 1910 and 1913, L. Gouy and D. Chapman [19] used Maxwell-Boltzmann statistic to propose the exponential decrease of the surface potential. His theory formulates that the thickness of the double layer would not be that of an ion but would extend a certain distance in the electrolyte, calling this zone the diffuse layer. In 1924, O. Stern [20] presented his model as a hybrid of both, with a stationary layer, the so-called Stern layer, where the ions remain immobile very close to the surface, and a less ordered and moving layer with charges of opposite sign forming a diffuse layer. Later, in 1947, Grahame [21] proposed that some ions would lose their solvation shell and be adsorbed by the metal, forming the compact double layer or the inner Helmholtz layer. On top of this, a layer of solvated ions would accumulate, corresponding to the diffuse double layer as defined by Stern or the outer Helmholtz layer. He also defined the inner and outer Helmholtz planes that would pass respectively through the charge centres of the inner and outer Helmholtz layers.

The current model (Figure 1.5) was presented in 1963 by Bockris, Devanathan and Müller (BDM) [22]. In this model, the first layer consists of water molecules and specifically adsorbed anions, with the internal Helmholtz plane passing through their centres. A second layer composed of water molecules and solvated cations would be situated above the first, with the Gouy plane or external Helmholtz plane passing through the centre of these ions, beyond which the diffuse layer would extend.

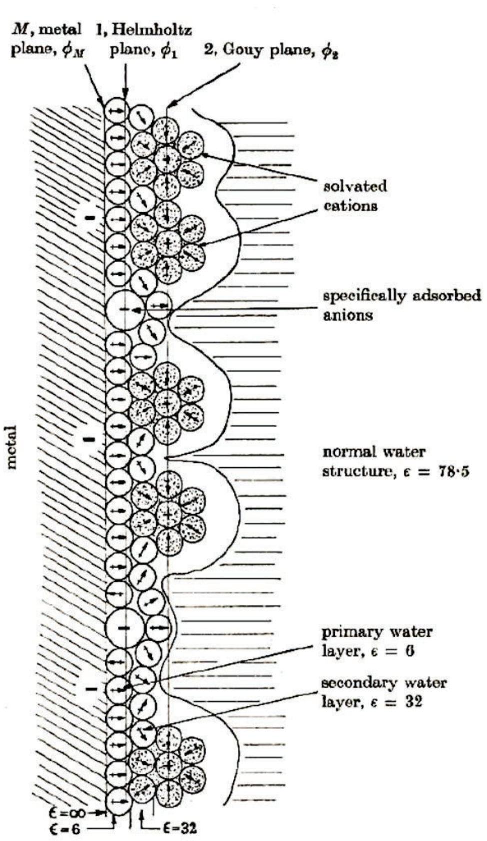

[23]

Figure 1.5 BMD model of double layer [22].

With the introduction of carbon as electrode (supercapacitors), the model was further elaborated and adapted to materials with high surface area. The carbon particles have sizes in the micrometre range, and each particle is filled with pores with diameters of nanometres. IUPAC classifies nanoporous materials in three categories depending on the pore size diameter: macropores are larger than 50 nm, mesopores are between 2 and 50 nm and micropores are less than 2 nm [23]. The large specific surface area has a small contribution from the surface of the particles and a big contribution from the pores. In 2006 Chmiola [24] observed an anomalous increase in the capacitance in organic electrolytes for titanium carbide-derived carbons with a pore size of less than 1 nm. Huang et al. proposed in 2008 [25] a universal theory to explain the charge storage mechanism in organic electrolytes for different pore size. Mesopores are capable of store solvated counterions in contact with the pore walls on one side and solvated ions, which would occupy the central part of the pore, on the other side (Figure 1.6 a). Micropores only form a line of solvated (Figure 1.6 b) or desolvated (Figure 1.6 c) counterions along the axis of the pore. For aqueous electrolytes, they found that the model is still applicable even though the ions always remain solvated in the micropores.

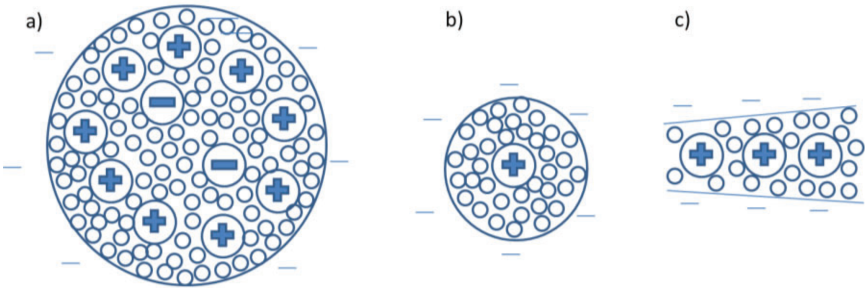

Figure 1.6. Double layer in macropores (a), mesopores (b) and micropores (c).

Supercapacitors outperform conventional capacitors in terms of energy density, storing several orders of magnitude higher, although their power and lifetime are lower. Compared to batteries, supercapacitors can be charged in seconds while batteries have charging times in the order of hours. For this reason, supercapacitors can surpass batteries in terms of power, making them ideal for applications that require rapid charge or discharge, like energy recovery during braking. The life expectancy of the batteries is only few thousand cycles [12], being also widely surpassed in this aspect by supercapacitors. However, batteries can vastly outperform supercapacitors in terms of specific energy. The relatively high amount of stored energy and short charging times place supercapacitors between electrostatic capacitors and batteries, filling the gap between them (Figure 1.7).

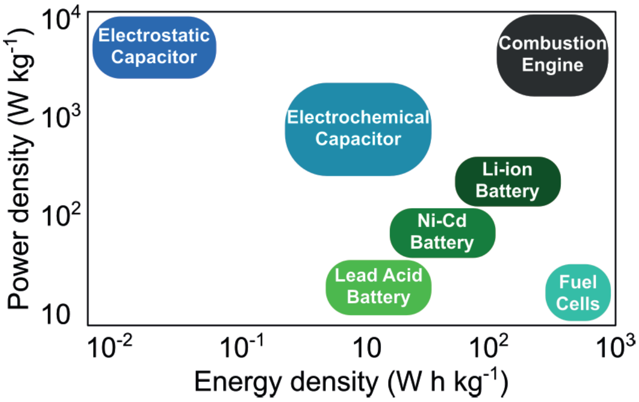

Figure 1.7 Ragone plot of different energy storage devices [26].

1.5 Pseudocapacitors and hybrid capacitors

If the ions react chemically with the surface of the electrodes through fast and reversible redox reactions, i.e., surface redox or intercalation of ions, a faradaic current is obtained at the interface between the electrolyte and the electrode, and the device is called a pseudocapacitor [27], storing more energy but having a slower response (low power) and shorter cycle life than EDLCs. The behaviour of pseudocapacitors differs from batteries, being similar to that of capacitors where a) the voltage varies almost linearly when adding or removing charge and b) an almost constant current is produced when the voltage undergoes a linear change with time, dV/dt = constant [28]. It is assumed that 1-5% of the capacitance of EDL carbon capacitors comes from pseudocapacitance due to a faradaic reaction of the surface oxygen functionalities [29]. Three types of reversible redox mechanisms are contemplated in pseudocapacitance: (1) underpotential deposition of adatoms, such as those of H on Pt or Pb on Au, (2) intercalation pseudocapacitance reactions, such as TiS_2 or CoO_2 hosts accommodating Li, and (3) redox pseudocapacitance, which includes the conversion of some oxidized species into reduced (or vice versa) in a redox system in solution, such as aqueous $\mathrm{Fe(CN)}_6^{4-}/\mathrm{Fe(CN)}_6^{3-}$, or in a hydrous oxide, such as $RuO_2 \cdot nH_2O$, $IrO_2 \cdot nH_2O$, $Co_3O_4 \cdot nH_2O$ [29], [30]. Other examples of pseudocapacitive materials are conductive polymers and transition metals such as Ru, Mn, Co, Fe, Ni, Mo, V, or Ti, used in metal oxides, metal sulphides, metal nitrides, metal hydroxides, or metal carbides [31].

A hybrid capacitor is composed of a capacitive electrode and a battery-type electrode. In the battery-type electrode, redox processes produce phase changes during which the potential remains constant, showing a pair of well-defined peaks in cyclic voltammetry (CV) and a flat profile (plateau) in galvanostatic charges-discharge [32]. Typical battery materials have a phase change at a well-defined potential by changing from one oxidation state to another such as $PbO_2 \rightarrow Pb$, $PbSO_4 \rightarrow Pb$ [28]. To maximize the specific and volumetric capacity, graphite anodes, which is a very abundant non-metallic material, or metallic Li, Na, Mg or Al can be used in batteries, although as the latter are very reactive, they are usually used in alloys with Si, Sn or Sb. The cathodes can be made of metal sulphides or oxides, such as V, Mo or Ti or use oxygen from an air flow in the so-called air cathodes in the Zn-air and Li-air batteries [33]. Typical commercial batteries are lithium iron phosphate battery (LFP), nickel cobalt manganese lithium battery (NMC) or lithium titanate battery (LTO). New solid-state batteries (SSBs), still in development, are capable of using a solid electrolyte thus eliminating the liquid electrolyte solution and separator. Examples of materials for SSBs are lithium lanthanum zirconium oxide (LLZO) and the used in lithium iron battery (Li-FeS_2) [34].

The main energy storage mechanisms and the typical forms they show in electrochemical experiments, cyclic voltammetry (CV) and galvanostatic charge-discharge (CD), are shown in Figure 1.8.

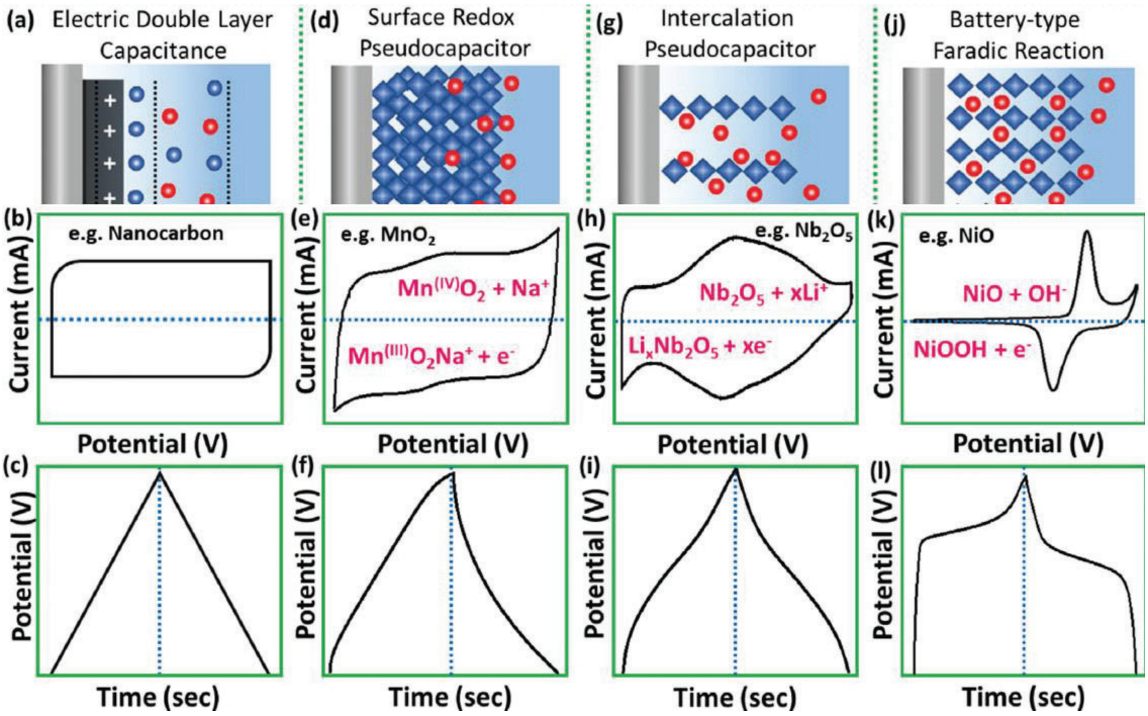

Figure 1.8. Scheme of the main energy storage mechanisms and corresponding CV and CD curves: a–c) electrical double layer capacitance, d–f) surface redox capacitance, g–i) intercalation capacitance, and j–l) faradic battery-type (adapted from [32]).

1.6 Conclusions and thesis objectives

To fill the gap in Ragone's plot between EDLC and batteries (Figure 1.7), much effort has been devoted to increasing the specific power of the batteries and the specific energy in the supercapacitors. Different strategies have been followed in the latter case, such as using carbons with a large surface area, nanostructured electrodes or materials that display pseudocapacitance, and the search for electrolytes with a larger potential window.

The first objective of this thesis is the increase of energy and power in activated carbon-based supercapacitors in aqueous electrolytes. We have sought to reduce impedance and increase energy efficiency to achieve this, verifying that both values are closely related. Several strategies have been taken into account: 1) The mass balance of the electrodes to compensate for the electrical charge, 2) the thermal treatment of the electrodes, which has a special impact on reducing impedance and increasing power by considerably reducing charging and discharging times, 3) the use of super-concentrated electrolytes, that can expand the potential window, 4) the choice of the most suitable membrane and 5) the combination of capacitive and faradaic materials in the same device.

The other main objective of this thesis is to study the degradation of the materials that make up supercapacitors based on activated carbon, especially those based on the super-concentrated 27 m KAc electrolyte. An extensive post-mortem study of the electrodes has been carried out and some cells have been reassembled, which has helped to understand the degradation mechanisms and has served to open the possibility of a second life for the degraded devices.

2 Experimental and methods

2.1 Introduction

This chapter presents the preparation methods and characterisation techniques of the materials and cells used in this thesis. Section 2.2 presents the materials used, their preparation method, and the cells used for electrochemical characterization. Sections 2.3 and 2.4 present the techniques used for the physicochemical and structural characterisation of the electrolytes and materials. Section 2.5 presents the electrochemical techniques applied in this thesis.

2.2 Preparation of electrodes, electrolytes, and cell assembly

This section is dedicated to the manufacture of the electrodes, the preparation of the electrolytes and the assembly method of the supercapacitors with the description of their main components.

2.2.1 Manufacture of the electrodes

Activated carbon is the material of choice for supercapacitors due to its high surface area, easy control of pore size distribution, low cost, and simple management. For the manufacture of the electrodes, we used YP-50F (Kuraray, Japan) activated carbon as active material, carbon black Super P (>99%, Alfa Aesar, Germany) as electronic conductor and polyvinylidene fluoride (PVDF) (Sigma-Aldrich, France) or polytetrafluoroethylene (PTFE) (60 wt % dispersion in H_2O, Sigma-Aldrich, USA) as binder with 85: 10: 5 mass ratios weighted with a microbalance (Figure 2.1.a). We also used *N*-Methyl-2-pyrrolidone (NMP) (1-Metil-2-pirrolidinone-anhydrous, 99.5%, Sigma-Aldrich, USA) or ethanol absolute (≥99.8%, Sigma-Aldrich, UK) as solvents for PVDF and PTFE, respectively. The paste with PTFE was prepared using the following two methods, and the paste with PVDF was prepared using only 2-b.

1) A homogeneous mixture is obtained using magnetic stirring (Figure 2.1.a) at 60 ° C until the ethanol evaporates. The dry paste is then spread on a glass surface using some drops of ethanol to facilitate paste rolling and then pressed with the help of a bottle until a self-standing film of about 50-60 microns is obtained (Figure 2.5.b) as measured with a micrometre (Figure 2.1.b).

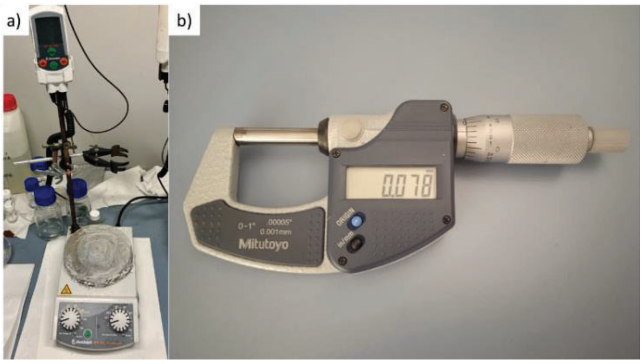

Figure 2.1. a) Magnetic stirring. b) Micrometre.

2) Mixing and grinding with a Retsch ball mill, model MM400, with a maximum frequency of 30 Hz (Figure 2.2), which breaks the particles and homogenizes the mixture. After some tests, we chose 20 Hz for 10 minutes.

Figure 2.2. Ball milling machine.

By selecting the grinding speed of the ball mill, a fine paste is achieved so that the sample spreads easily. Electrodes were made with two different techniques:

a. Roll and press the wet paste to fabricate a self-standing electrode as in 1).
b. Adjusting the viscosity by adding a small amount of solvent, if necessary, and coating on an EQ-bcaf 15μm aluminium foil with doctor blade (tape casting) technique using a BYK automatic film applicator (Figure 2.3) with a speed of 60 mm/s.

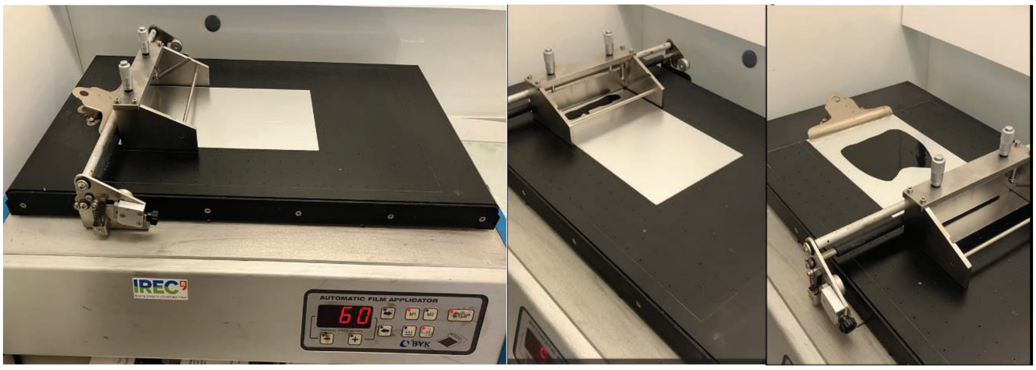

Figure 2.3. Dr. Blade's casting process.

The films are then dried between 60 ° C and 110 ° C in a NRTL vacuum oven (Figure 2.4) for 24 hours and then stored in an oven at 60-80 ° C until use. For the preparation of the electrodes, an electrode puncher is used (Figure 2.5.a) to cut 8-12 mm discs (Figure 2.5.b) and weighed them just before their use (Figure 2.5.c).

Figure 2.4. Vacuum oven used to dry the electrodes.

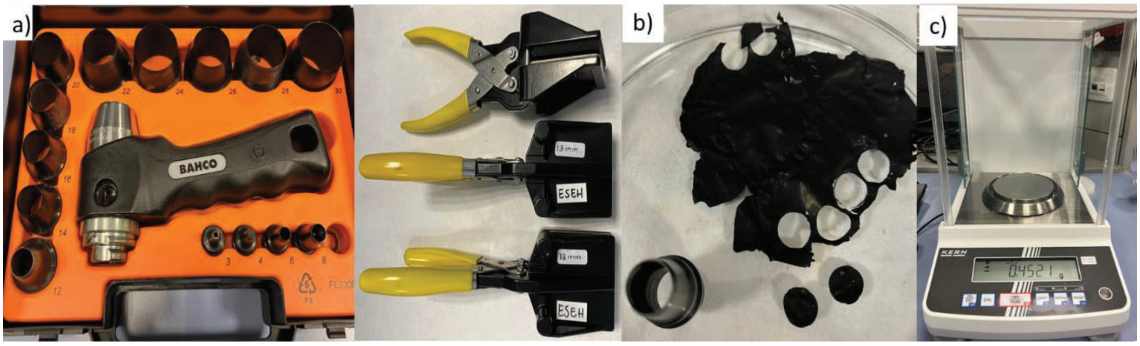

Figure 2.5. a) Punchers used to cut the discs. b) Self-standing electrodes and discs. c) Balance.

2.2.2 Electrolytes

The electrolyte in a supercapacitor plays a crucial role in determining its performance. The choice of electrolyte affects the electrochemical behaviour of the supercapacitor, including its capacitance, energy density, power density and cycle life. Other parameters to consider are the operating temperature, electrochemical stability, safety requirements and environmental considerations. The stability over time is also decisive when choosing them to prolong the life of the devices.

Basic and slightly basic aqueous electrolytes were prepared using different salts starting from the baseline electrolyte, 1M KOH (reagent grade, 90 %, Sigma-Aldrich, France) and anhydrous potassium acetate (CH_3COOK, > 99%, Alfa Aesar). Formulations were weighed and dissolved to prepare diluted and water-in-salt electrolytes (chapters 3 and 4, respectively) using milli-Q ultra-pure water (18.2 MΩ·cm), previously degassed with nitrogen to remove any dissolved oxygen content. Once prepared, the bottles were sealed to avoid oxygen contamination with a flexible cap that allowed the electrolyte extraction with a syringe (Figure 2.6).

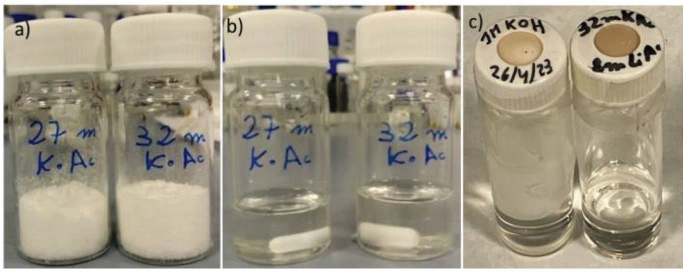

Figure 2.6. Formulation of water-in-salt electrolytes a) Salt weighting. b) Mixing with ultra-pure water and c) bottle sealing

2.2.3 Cell assembly

The materials and components were assembled using two types of electrochemical cells for electrochemical characterisation. In most of the studies presented in this thesis, CR2032-type stainless steel coin cells (Figure 2.7.a) were used; the stack made of punched electrodes (Figure 2.7.b) and the membrane (Figure 2.7.c) soaked with the electrolyte is pressed and sealed with a coin cell crimping machine (Figure 2.7.d). The coin cells are allowed to rest for 24 hours before use to allow the diffusion of the electrolyte into the electrodes' pores. The Figure 2.7.e represents a scheme of the coin cell assembly.

The separator is a porous and permeable membrane that separates the electrodes. It allows the passage of ions from one side to the other but prevents the passage of electrons, thus avoiding the cell's short circuit. In this thesis, we have used mainly non-commercial glass fibre (GF), commercial glass fibre Whatman GF/A or GF/C, and polypropylene membrane (PP) Celgard 3501. Glass fibre is hydrophilic and suitable for aqueous electrolytes, so it was mainly used in this thesis. PP and glass-fibre separators were used for aqueous and organic electrolytes.

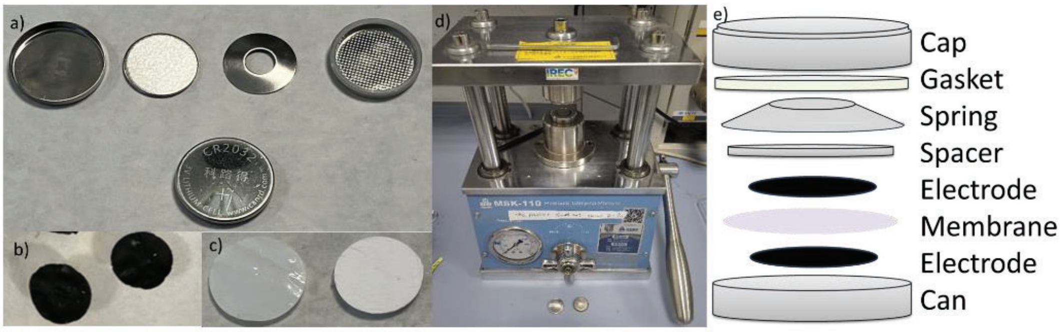

Figure 2.7. Coin cell. a) Components. b) Electrodes. c) Membranes. d) Hydraulic crimping machine. e) Coin cell scheme.

The second type of electrochemical cell used in this thesis was the Swagelok cell (Figure 2.8). It was equipped with 3 mm glassy carbon current collectors. This type of cell can be easily assembled and disassembled to study its components. It was used to study electrolyte stability (Chapter 4) and electrode degradation as part of the post-mortem studies (Chapter 5).

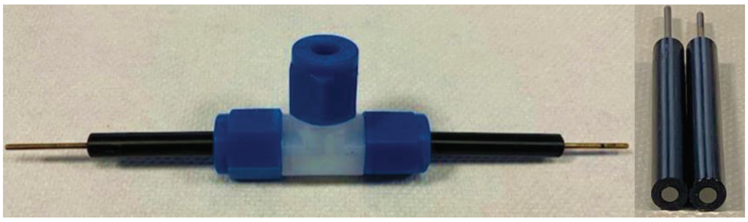

Figure 2.8. Swagelok cell with glassy carbon current collectors.

2.3 Electrolytes characterisation

This section contemplates the physical characterization of the electrolytes in terms of viscosity and conductivity. Viscosity has a large impact on the mobility of ions in electrolytes. The search for a balance between concentration and conductivity seeks to achieve a large number of charge carriers without reducing mobility due to viscosity [35]. Viscosity was measured at room temperature with a Brookfield DV2T viscometer (Figure 2.9.a). Measures were taken three times with a ramp between 0 and 200 rpm taking the average of them. The conductivity of the electrolytes plays a crucial role in the operation of batteries and supercapacitors, as it determines the efficiency of the flow of ions between the electrodes. This flow is determined by the type of electrolyte and its concentration. It is essential to maintain high conductivity to improve the performance and reduce the resistance [35]. The conductivity of electrolytes was measured at room temperature with a Lutron conductivity meter (Figure 2.9.b). Measures were taken three times, taking the average of them.

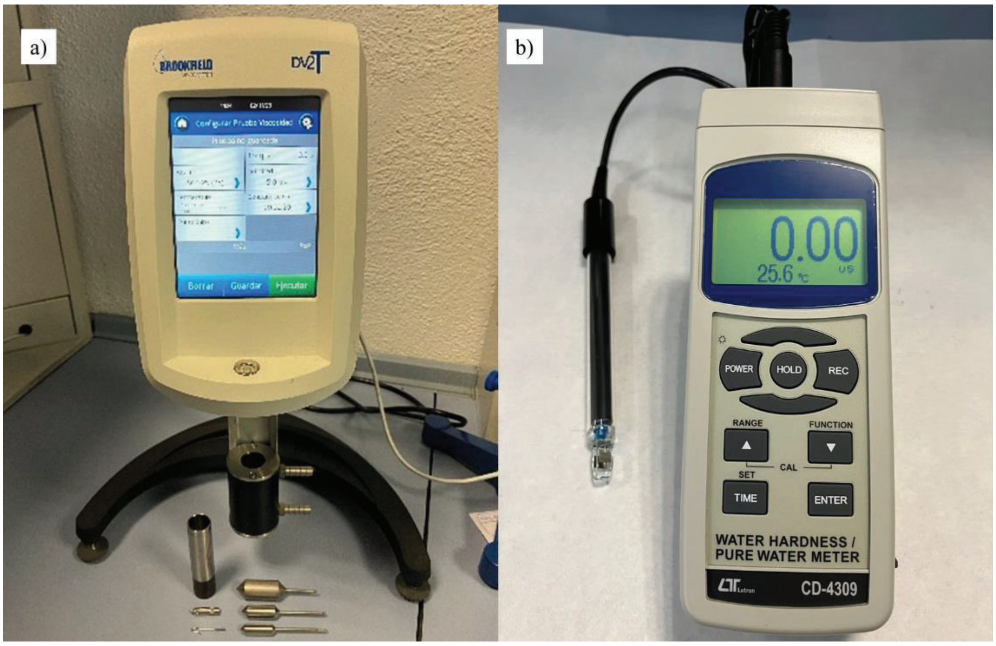

Figure 2.9. a) Viscometer Brookfield DV2T and b) Lutron CD-4309 conductivity meter.

2.4 Materials characterisation

Different techniques have been employed to understand material properties and the changes in morphology, physicochemical, and structural characteristics after cycling. The following sub-sections present these techniques.

2.4.1 Particle Size Distribution

Particle Size Distribution (PSD) is a technique used to measure the sizes of the particles. A Malvern Mastersizer 2000 particle size analyser (Figure 2.10.a) was used for the studies. PSD uses laser diffraction or low-angle light scattering to measure particle size distribution. It uses a combination of red and blue lasers for different wavelengths of light to create a large particle size range. The analyser has a deposit that contains a liquid (water in our case) to make a suspension with the particles to be analysed. The results display a particle size distribution from nanometre to millimetre range and its volume distribution. The volume distribution of YP50 shows the following particle size values: d(0.1) = 1.657 µm, d(0.5) = 5.839 µm and d(0.9) = 12.088 µm (Figure 2.10.b).

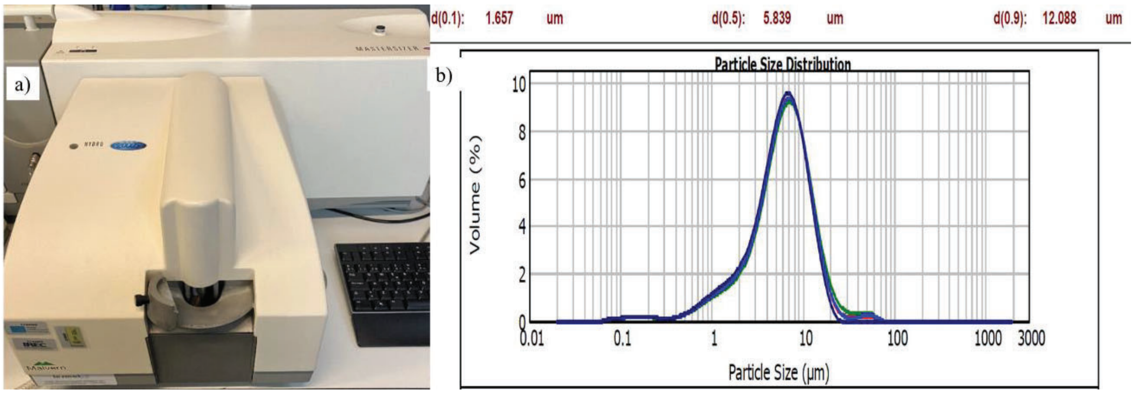

Figure 2.10. a) Malvern Mastersizer 2000 particle size analyser. b) PSD of YP50 particles.

2.4.2 Surface area and pore size and volume

The nitrogen (N_2) physisorption technique was applied for the textural analysis of the materials and electrodes using a Micromeritics TriStar II physisorption instrument with a FlowPrep060 degassing unit (Figure 2.11). The technique consists of degassing the samples at 90 ºC for 5 hours in an N_2 flow, and then the sample is transferred to the physisorption instrument, where a vacuum is created, and the sample tube is cooled down to 77 K (196 ºC below zero) by immersing it into the N_2 dewar. The isotherm points are recorded by applying precise N_2 gas injections into the sample tube and then measuring the actual pressure in the tube after stabilisation; the difference between the dosed N_2 gas and the actual measured pressure in the sample tube will account for the adsorbed N_2 onto the surface of the sample. The adsorption branch of the isotherm is obtained by repeating this procedure for several target pressure values, up to relative pressure $p/p_0 = 1$, where p is the equilibrium pressure reached and p_0 is the saturation pressure. The desorption branch is recorded by applying the reverse scan down to lowest vacuum. Data is shown in the adsorption-desorption isotherm, that graphs the amount of gas adsorbed/desorbed versus the relative pressure p/p_0. At low T (77 K), N_2 molecules adsorb onto the sample surface, and as N_2 pressure increases, more N_2 molecules will be adsorbed. At low relative pressures, a monolayer of N_2 molecules starts to form on the sample. As the pressure increases, the gas molecules fill the smaller pores and begin a multilayer coverage. When the pressure increases even more, the N_2 molecules fill all the pores and cover the external surface of the sample. Studying absorption-desorption curves provides information on size, volume, and surface area.

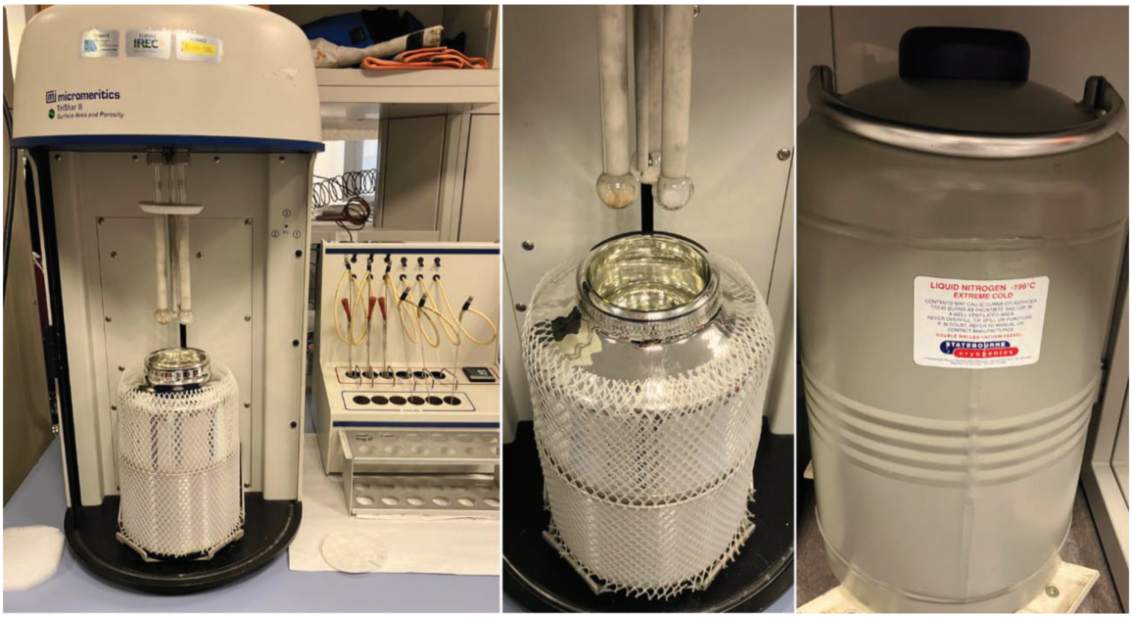

Figure 2.11. Micromeritics TriStar II physisorption instrument for B.E.T. analysis.

According to the IUPAC, the isotherms are classified into six types to guide in their identification. The isotherms are studied through mathematical models that allow obtaining the specific surface area and the size and pore volume. The surface area was calculated with the Brunauer–Emmett–Teller (BET) method, that uses the low relative pressure part of the graph, adsorption with multilayer coverage. The pore size was determined by de Barrett-Joyner-Halenda (BJH) method using the high relative pressure part of the graph and Kelvin model, valid for mesopores (pores between 2-50 nm) and small macropores (> 50 nm), been not valid in our equipment for micropores (< 2 nm) [36], additionally, the appearance of a fictitious peak in the desorption isotherm necessitates selecting the pore size calculated from the adsorption isotherm. An estimation of the pore volume was taken from the accumulative of the isotherm. The YP50 active material and electrodes were studied by nitrogen physisorption technique (Figure 2.12).

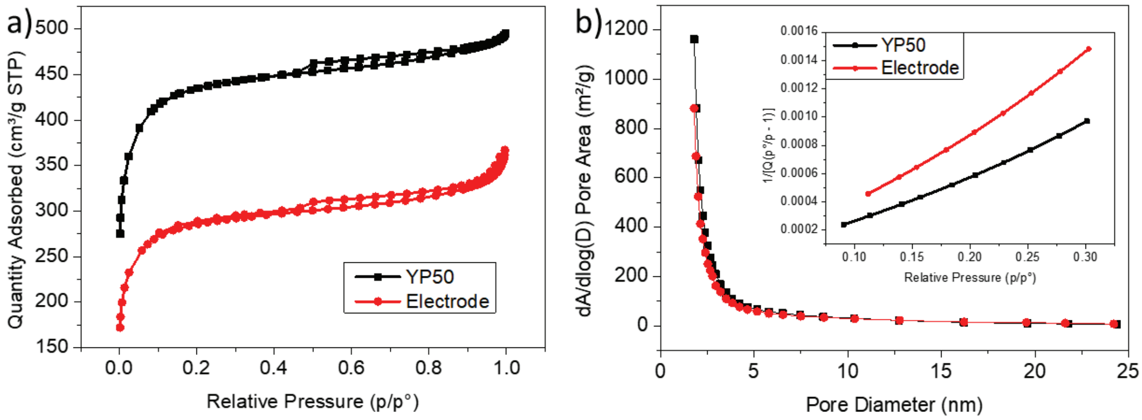

Figure 2.12. (a) Nitrogen adsorption isotherm plot. (b) Pore size distribution and surface area (inside).

Comparing the YP50 active material and electrodes by N_2 physisorption technique, we found a surface area of 1,683 and 1,100 m²/g, a pore volume of 0.77 and 0.57 cm³/g, and a pore size of 3.80 and 4.91 nm, respectively (Table 2.1). The active material (YP50) possesses a larger surface area and pore volume compared to the electrode, but a smaller pore size. This is due to the Super P particles blocking some of the small pores, making them inaccessible and thereby decreasing both the surface area and pore volume. While the smaller pores are easily obstructed by the Super P particles, the larger pores remain accessible, leading to an overall increase in the average pore size.

Table 2.1 Surface are, pore volume and pore size of YP50 and electrodes.

Material	Surface area (m^2/g)	Pore volume (cm^3/g)	Pore size (nm)
YP50	1683	0.77	3.80
Electrode	1100	0.57	4.91

2.4.3 Scanning Electron Microscopy

A Field Emission Scanning Electron Microscope (FE-SEM) Zeiss Series Auriga 60, equipped with SE2 and In-Lens secondary electron detectors, as well as a coupled EDS (Energy Dispersive Spectroscopy) detector model INCA from Oxford Instruments, was used to study the different morphologies of activated carbon particles and electrodes (Figure 2.13). In FE-SEM, a strong electrostatic field of 1-20 KV induce electron emission in the sharp tip of a tungsten wire, where the electric field is of the order of 10^9 V/m and accelerated them. These electrons, called primary electrons, are focused with electronic lenses on the materials to be studied. The electron beam sweeps across the sample from which it extracts electrons, called secondary electrons, which the detectors collect. The SE2 secondary electron detector offers a large depth of field (z-axis) with high acceleration potentials (> 5 KV), usually used at low magnifications. The In-Lens secondary electron detector is located within the electron column (hence its name), obtaining optimal results at low acceleration potentials (< 5 KV), having good spatial resolution (x-y axis), and being able to work with high magnifications. Energy dispersive X-ray spectroscopy (EDS) is a detector coupled with SEM that allows the study of the chemical composition of the visualised area. It was used to identify the chemical changes after material degradation (Chapter 5). EDS spectra were obtained with an x-ray intensity of 20 KV and a working distance of 8.5 mm.

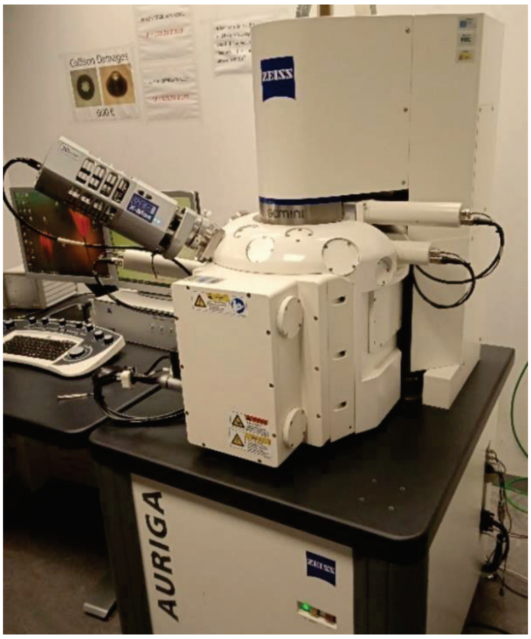

Figure 2.13. FE-SEM Zeiss Series Auriga 60.

Scanning Electron Microscopy (SEM) was used to study the morphology and size of the electrodes and their components. YP50 particles have an irregular shape, resembling irregular rocks, and the particle size is consistent with PSD experiments (Figure 2.10.b), there are many particles smaller than 1 μm, several particles between 1 and 10 μm and a few larger than 10 μm (Figure 2.14.a). The high porosity, responsible for their large specific surface area, is illustrated in Figure 2.14.b, matching well with PSD analysis. Super P conductive carbon appears as small spheres of 30-50 μm with a tendency to agglomerate (Figure 2.14.c). All components of the complete electrode are clearly distinguishable in Figure 2.14.b, with YP50 big particles surrounded by smaller spherical super P particles, interconnected by white lines corresponding to PTFE binder.

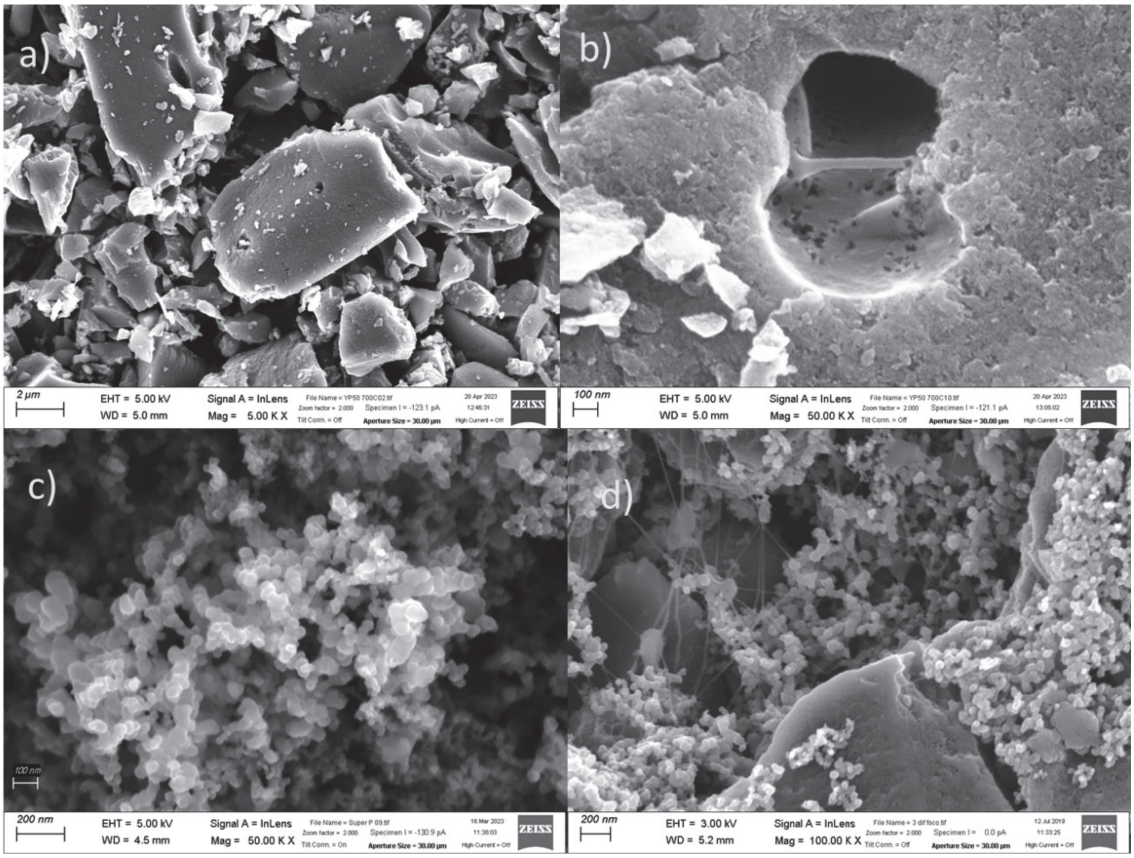

Figure 2.14. SEM images of a), b) YP50 activated carbon. c) Super P conductive carbon. d) YP50:Super P:PTFE electrode.

2.4.4 X-Ray Diffraction

X-Ray Diffraction (XRD) is used to determine the materials phase-purity, composition, and crystalline structure. When an X-ray beam is incident on a crystalline structure, the incident rays are diffracted in multiple directions, cancelling out by destructive interference in most directions. Only a few directions add waves constructively, forming a diffraction pattern that satisfy Bragg's law.

$$n\lambda = 2d\mathrm{Sin}\theta \qquad \text{(Eq. 2.1)}$$

Where n is a positive integer, λ is the wavelength of the incident beam, d is the distance between the crystallographic planes, identified by the Miller indices (hkl) and θ is the angle of the incident beam (the angle between incident ray and the scatter plane).

By applying Scherrer's law:

$$L = \frac{k\lambda}{\beta\cos(\theta)} \qquad \text{(Eq. 2.2)}$$

it is possible to calculate the thickness of the stacked layers, L_c, and the crystallite size, L_a,

$$L_c = \frac{0.9\lambda}{\beta_{00l}\cos(\theta_{00l})} \qquad \text{(Eq. 2.3)}$$

$$L_a = \frac{1.84\lambda}{\beta_{100}\cos(\theta_{100})} \qquad \text{(Eq. 2.4)}$$

where, for activated carbon, the values of k_c and k_a are 0.9 and 1.84 and β is the full width at half maximum (FWHM) of the hkl peak in radians [37].

The number of aromatic layers is calculated by the formula below [38]

$$N = \frac{L_c}{d_{00l}} + 1 \qquad \text{(Eq. 2.5)}$$

XRD measurements presented in this thesis were conducted using a Bruker D8 Advance with Bragg-Brentano configuration and Cu Kα radiation (λ = 1.5406 Å) using 40 KV and 40 mA. (Figure 2.15). The XRD patterns were analysed with the X'Pert HighScore Plus software [39].

Figure 2.15. XRD Bruker D8 Advance.

Crystalline graphite has a hexagonal structure arranged in layers with an interatomic distance of 3.35 Å [40]. In X-Ray Diffraction experiments (XRD), graphite shows a well-defined peak around 26-28º corresponding to the (002) plane. From this angle, the different parameters of the crystal can be known, such as the interplanar distance d, the dimensions of the crystal L_a and the thickness of the packed layers L_c [38]. When graphite loses its crystallinity, the layers rotate and separate, increasing the disorder and forming the so-called turbostratic structures [41], characterized by a shift towards lower angles of the (002) peak. XRD of YP50 particles (Figure 2.16.a) shows the typical shape of non-graphitizing carbon (hard carbons with high porosity and low density) with a broad peak assigned to (002) plane around 22.7°. Super P peak of (002) plane appears around 25°, is better defined than YP50 and less shifted to low angle values, indicating higher crystallinity (Figure 2.16.b). Both carbon materials show a clear peak around 44°, indexed to (100) and (101) planes [38]. The interplanar distance was 3.91 Å for YP50 and 3.55 Å for Super P (Table 2.2). Crystallite sizes L_c and L_a where 10.52 and 49.04 Å for YP50 and 22.92 and 50.02 for Super P. The number of aromatic layers per carbon crystallite of 3.69 for YP50 and 7.46 for Super P. All these results are in good agreement with the literature [42], [43]. XRD of PTFE binder (CF_2=CF_2) shows a complex pattern of well-defined peaks (Figure 2.16.c), exhibiting a pronounced intensity at the (100) peak, around 18º, indicating its high crystallinity [44]. The pattern of the electrodes (Figure 2.16.d) shows a rich mixed pattern where we can identify the 18º peak of PTFE and another one in 21.26º, the (002) peak of YP50 remains in the same position of 22.7º, but that corresponding to Super P has moved down to 23.7º. Several sharp peaks appear around 27º, 36º, 54º and 56º and a broad one around 30º reflecting the influence of PTFE. The broad carbon peak assigned to (100) and (101) planes appear around 44° (Table 2.2).

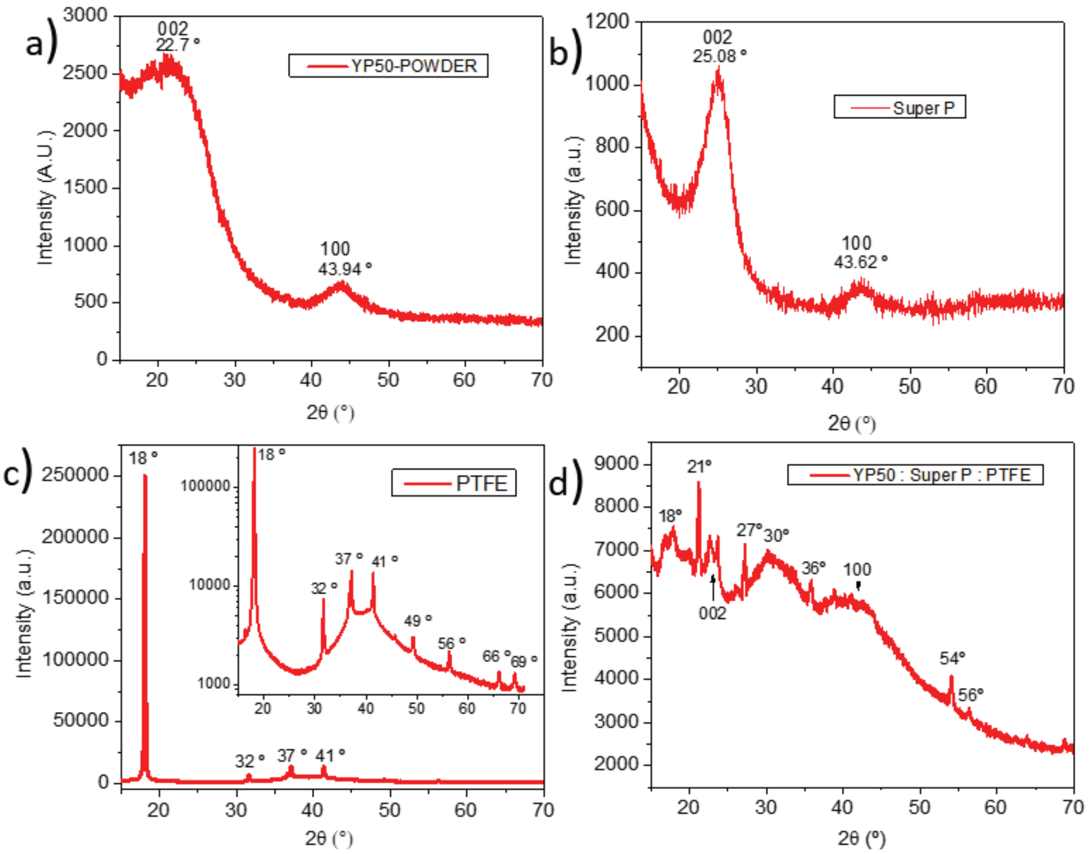

Figure 2.16. XRD of a) YP50, b) Super P, c) PTFE (linear and log scale) and d) full electrode.

Table 2.2. Crystallite parameters

Sample ID	$2\theta_{002}$ (deg)	$2\theta_{100}$ (deg)	β_{002} (deg)	β_{100} (deg)	d_{002} (Å)	L_c (Å)	L_a (Å)	N_{ave} (-)
YP50	22.70	43.94	7.70	3.57	3.91	10.52	49.04	3.69
Super P	25.08	43.62	3.55	3.50	3.55	22.92	50.02	7.46
Electrode	22.70-23.70	43.08	1.40	5.40	3.91	57.85	32.32	15.79

2.4.5 Fourier Transform Infrared Spectroscopy

Infrared Spectroscopy (IR) is a non-destructive technique widely used for rapid material identification. A Bruker Alpha-P Attenuated Total Reflectance (ATR) Fourier Transform InfraRed spectrometer (FTIR) with a diamond-ATR crystal (Figure 2.17) was used to study the materials and the electrodes in a wavenumber of the mid-infrared region (MIR) range from 4000 cm^{-1} to 375 cm^{-1}. The ATR technique uses the property of light called total internal reflection, which occurs when light travelling in one medium encounters, at a certain angle, another medium with a very different refractive index. In ATR, light travels through the diamond crystal at such an angle that it is reflected between its two faces and creates evanescent waves that can leave the crystal and penetrate the sample placed on top of it for a distance of the order of microns, which depends on the wavelength of the light, the angle of incidence and the refractive indices of the ATR crystal and the medium being analysed. The incident light causes vibrations at the molecular level, dipole moment change, that provide qualitative information about the functional groups present in the molecule and its structure. Quantitative information can be extracted with Beer's law, which relates the intensities of light that enters and leaves after absorption, establishing a relationship between absorption A and the path length l, the molar decadic absorption coefficient ε, and the concentration c

$$A = l\,\varepsilon\,c = -\log_{10}(T) \qquad \text{(Eq. 2.6)}$$

where T is the transmittance of the sample, that is, the ratio between the light intensity measured before (I_0) and after (I) the interaction with the sample [45]. In the interferometer, the light produced by the infrared source goes to a beam splitter that reflects 50% of the light towards a stationary mirror and the other 50%, which crosses the beam splitter, is directed towards a moving mirror. The light returning from both mirrors is recombined in the beam splitter. Since there is a moving mirror, the wavelengths return to the beam splitter in or out of phase, causing constructive or destructive interferences directed to the detector. The detector collects the signal and records at regular and precise intervals as interferograms of I_0 (Δl) and I (Δl), which are mathematically transformed into a unique spectrum of I_0 and I using the Fourier transform. FTIR is the most used technique in MIR spectroscopy due to its high signal-to-noise ratio (SNR) and higher optical performance compared to dispersive instruments, achieving short analysis times and the possibility of finding molecular fingerprints.

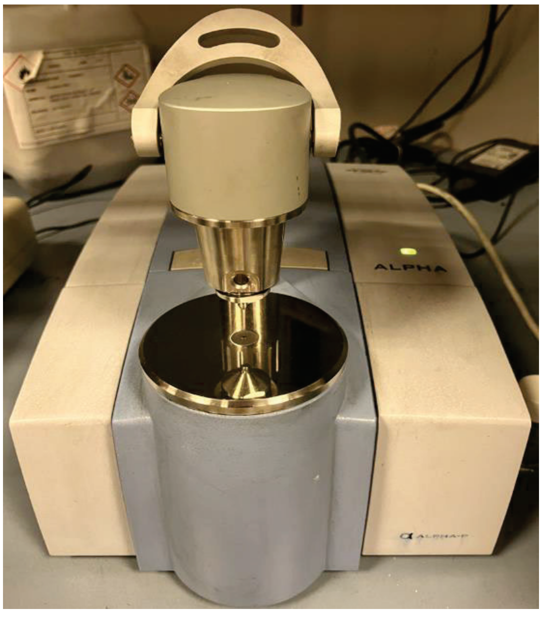

Figure 2.17. Bruker Alpha-P ATR-FTIR.

Fourier Transform Infrared (FTIR) spectroscopy was used to detect the surface functional groups of materials and electrodes investigated in this thesis. Figure 2.18 shows the FTIR spectra of a typical supercapacitor electrode based on YP50 active carbon and its components (Super P and Teflon). The peak around 2670 cm^{-1} is assigned to C-H stretches of aldehyde peak. Peaks around 2300 cm^{-1}, 1990 cm^{-1} and 2120-2055 cm^{-1} are assigned to stretching of C≡C triple bond. The peaks in the range 1760-1635 cm^{-1} are attributed to carbonyl (C=O) stretching vibration of aldehyde groups and ketones [46]. Peaks in the range 1555-1450 cm^{-1} are assigned to C=C vibrations.[47]. The two sharp bands in 1205 cm^{-1} and 1147 cm^{-1} are assigned to asymmetrical and symmetrical stretching of CF_2 coming from PTFE binder [48].

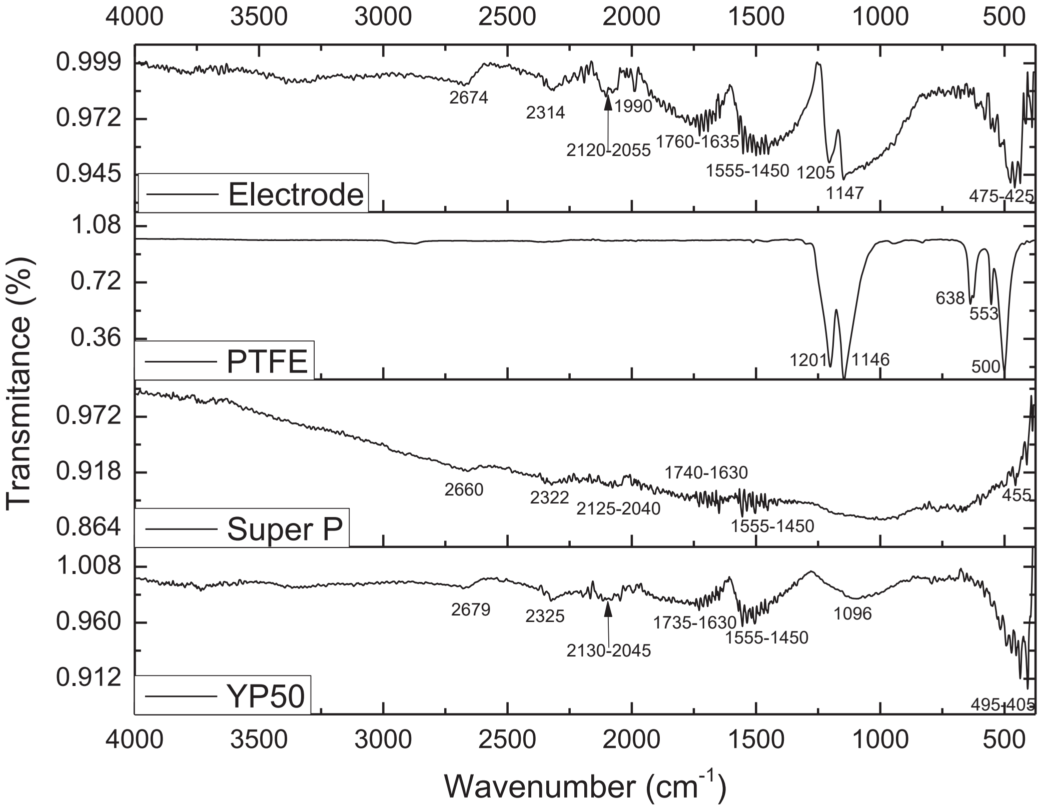

Figure 2.18. FTIR of the electrode and its components.

2.4.6 X-Ray Photoelectron Spectroscopy

The XPS technique is based on the photoelectric effect, which was discovered by Hertz in 1887, and Einstein was able to explain it in 1905 by assuming that light was quantised, for which he received the Nobel Prize in 1921. When a beam of electromagnetic radiation is irradiated on a material with an energy (frequency) greater than the ionisation energy of the atoms, it can eject a photoelectron. Knowing the energy of the incident ray and the kinetic energy of the photoelectron measured by the XPS detector, we can know the binding energy (E_B) of the orbital from which the electron comes.

$$E = h\nu = E_k + \Phi \qquad \text{(Eq. 2.7)}$$

where E is the energy of the incident photon, h is the Planck constant defined as:

$$h = 6{,}626\ 070\ 15 \times 10^{-34}\ \text{J·s} = 4{,}135\ 667\ 696 \times 10\text{-}15\ \text{eV·s} \qquad \text{(Eq. 2.8)}$$

ν is the frequency of the incident light, and Φ is the binding energy or work function, and it is the minimum energy that the photon must have to remove an electron from its orbit. If the frequency of the incident photon is too low, no emission occurs even if there are many photons. Once the minimum energy threshold is exceeded, the emission of photons is proportional to the intensity of the light, that is, to the number of incident photons. The XPS technique uses energetic X-rays capable of extracting core electrons (those that do not participate in chemical reactions), which have a well-known binding energy and can be used to know the composition of the samples. The XPS analysis is first done covering a wide range of about 1400 eV, and later, smaller ranges of about 20 eV are analysed in more detail, performing a high-resolution spectrum. When irradiating the material with x-rays, the radiation emitted can be of 3 types: x-ray fluorescence that is not recorded, Auger electrons that are used for quantitative analysis, and photoelectrons from which the desired information is extracted. The photoelectrons used in XPS come from the first shell, or k shell, and are identified with the symbol of the element followed by the shell number and the initial of the orbital, C1s refers to the s orbital of the first shell of the carbon atom [49]. The binding energy is affected by neighbouring atoms and their electronegativity or oxidation state, which affects the peaks of photoelectrons and Auger electrons. It is observed that the C1s binding energy increases as the number of bonds of the carbon atoms increases. This bond is done with more electronegative elements, and carbon atom is the more positively charged. In the case of the C1s peak, the area under the curve of the different peaks is proportional to the number of carbon atoms that have a specific type of bond (C-C, C=C, C-N, C-O, C=O, O-C=O, CF_2, CF_3) as the binding energy increases from 284.5 to 292.0 eV). It is important to emphasize the discrepancy in the results reported in the literature, as highlighted in [50].

Samples for analysis were sent to the Catalan Institute of Nanoscience and Nanotechnology (ICN2). The main components of the instrument used for the analysis are an ultra-high vacuum chamber, an x-ray source that passes through a monochromator to ensure the frequency of the incident radiation, a sample holder that is controlled from the outside, and the detector of the radiation coming from the sample (Figure 2.19).

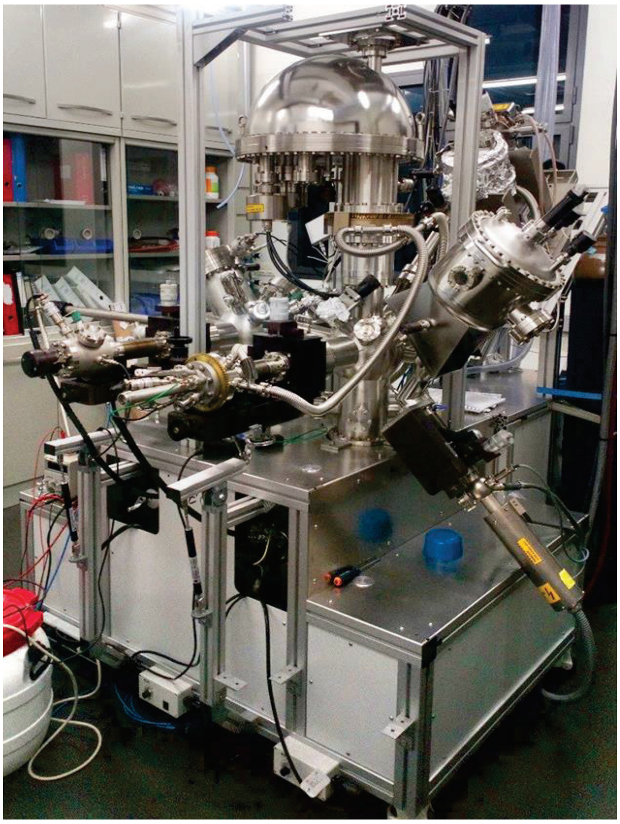

Figure 2.19. XPS at ICN2.

2.5 Electrochemical characterisation

Electrochemical measurements were performed with a VMP-3 potentiostat/galvanostat (BioLogic, France) (Figure 2.20.a). The device can be used in two or three-electrode connection mode. In two-electrode mode, the cell includes a Working electrode (WE) and a counter electrode (CE). The potential difference between WE and CE is measured, while the current is equal and opposite at the two electrodes. In the three-electrode mode, a reference electrode with a known, stable potential is connected to measure the potential of the WE. The RE (Figure 2.20.c) is usually used to study the redox reactions that occur in the WE since it is only used to control the potential and there is no current passing through it that could produce some type of reaction, as could happen in the CE. For this reason, the RE must have its redox potential and be stable against any change in the electrolyte, such as pH. The standard hydrogen electrode (SHE) is used as a reference for all electrodes, 0 V by definition. It consists of a platinum wire immersed in a hydrochloric acid solution into which hydrogen is injected. The saturated calomel electrode (SCE) in which mercury chloride (calomel) in a solid state, immersed in a saturated solution of KCl, reacts to give neutral mercury and chlorine ions with a potential of 0.244 V at 25 ºC with respect to the SHE, its use is in decline due to the toxicity of mercury. The silver/silver chloride electrode has a silver wire immersed in a silver chloride solution placed in a saturated KCl solution. with a potential of 0.222 V at 25 ºC compared to the SHE, it is the most used today. Pseudo reference electrodes are wires made of noble metals such as gold, silver, or platinum whose potential in a certain electrolyte has been measured with respect to a conventional reference electrode, although they are not as stable or reliable as the latter [51]. During the development of this thesis, the potentiostat/galvanostat was used in two-electrode mode since most experiments were carried out with complete cells. The saturated calomel, silver/silver chloride reference electrodes and the silver wire pseudo reference electrode were used to study the potential window of the electrolytes (Chapter 4).

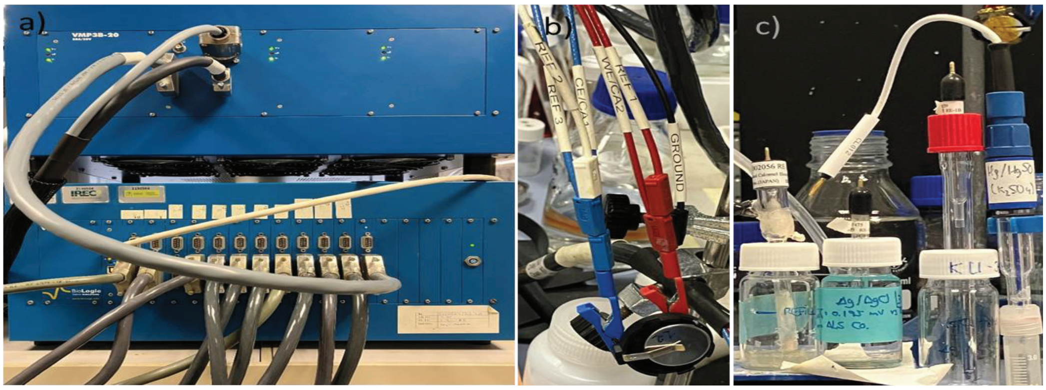

Figure 2.20. a) Potentiostat/galvanostat. b) Cables used: WE (red), CE (blue), RE (white) and ground (black). c) Reference electrodes.

2.5.1 Cyclic voltammetry

In a potentiostat, a constant voltage ramp is usually applied to study a material within the desired potential window; this is the potentiodynamic mode, with cyclic voltammetry (CV) being the most used technique. CV is a fast and easy-to-use technique commonly used in studies of electrochemical reactions, corrosion, batteries, and supercapacitors. In a supercapacitor it is usually applied a voltage ramp between 5 and 1000 mV/s, while if there are faradaic reactions is applied a ramp between 0.1 and a few mV/s. The constant voltage ramp is usually applied while measuring the current for several cycles, usually between 5 and 10, and then increases to higher voltage ramps to measure the rate capability, that gives the power response of the device. By varying the potential window at different rates, it is possible to explore the potential limit of the device. Long-term experiments, for a supercapacitor usually between 5,000 and 10,000 cycles, are carried out at different rates to study the capacitance decay with cycling. Looking at the shape of cyclic voltammetry it is easy to identify the purely capacitive materials (chapters 3 and 4), almost rectangular shape, from the faradaic materials (chapter 6), which have symmetric humps and a distorted shape [52] [12] (Figure 2.21).

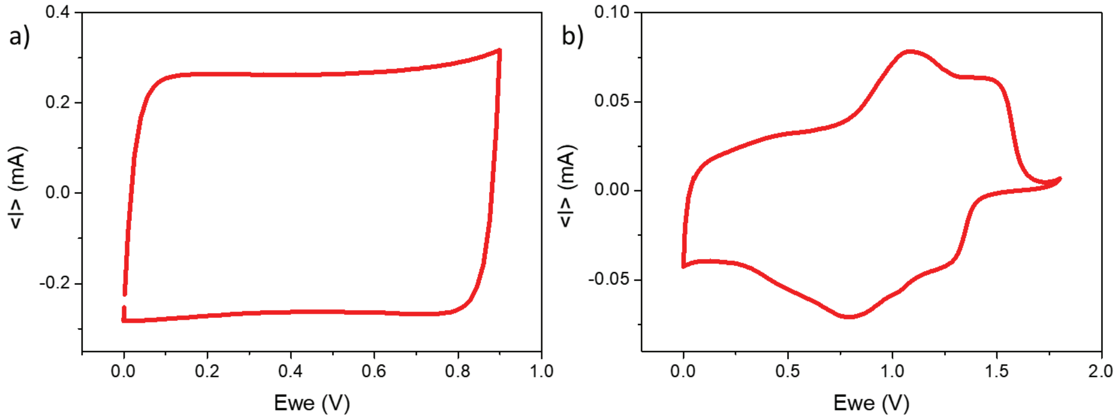

Figure 2.21. Cyclic voltammetry. a) Capacitive curve. b) Faradaic curve.

The capacitance of the full device is calculated by integrating the total area of the discharge curve.

$$C = \frac{1}{vV} \int_{V-}^{V+} I(V)dV \tag{Eq. 2.9}$$

Where C is the capacitance in farads (F), v is the scan rate in volts per second (Vs^{-1}), V is the potential window in volts (V), and I is the current in amperes (A).

The specific capacitance (C_{sp}) is given in farads per gram (F/g) and found by dividing the capacitance by the electrode’s mass (m) in grams (g).

$$C_{sp} = \frac{C}{m} \tag{Eq. 2.10}$$

In the literature, it is common to report the specific capacitance of a single electrode by multiplying the C_{sp} by 4. This result arises because a factor of 2 results from dividing only by the mass of one electrode, while the additional factor of 2 comes from not considering that the electrodes are connected in series [53].

2.5.2 Galvanostatic charge-discharge

Galvanostatic charge-discharge (GCD) is a complementary technique to CV for the electrochemical characterisation of supercapacitors. It is used to find the potential stability window or the device's capacitance. Current densities between 1 and 20 A/g are applied to evaluate a supercapacitor, while if there are faradaic reactions, current densities between 0.05 and 5 A/g are used. The constant current ramp is usually applied at a low rate while measuring the voltage for several cycles, usually between 5 and 10, and then increases the current ramps to higher values to measure the rate capability, which gives the power response of the device. By varying the potential window at different rates, it is possible to explore the maximum potential of the device, which is limited by the vertical voltage drop after achieving the maximum potential and the current is cut off, appearing as a sudden loss of voltage given by Ohm's law V = I·R. Long-term experiments for a supercapacitor, usually between 5,000 and 10,000 cycles, are carried out at different rates to study the capacitance decay with cycling. Looking at the shape of the GCH figures, it is possible to identify purely capacitive cells (Figure 2.22.a) from those that have faradaic materials and undergo some type of oxidation-reduction reaction (Figure 2.22.b) [54].

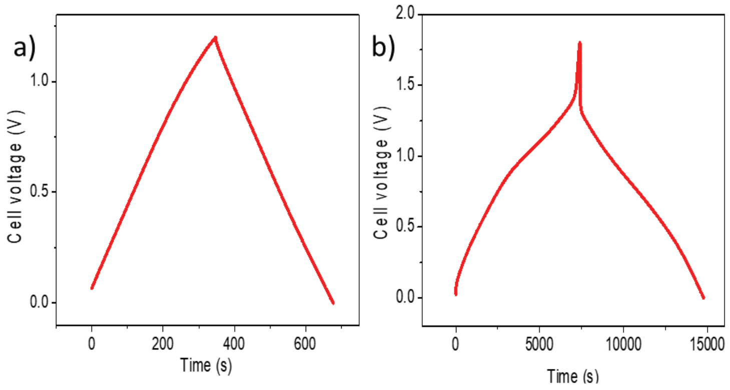

Figure 2.22. Galvanostatic charge-discharge: a) capacitive curve, b) faradaic curve.

Capacitance is calculated by multiplying the current by the discharge time divided by the voltage.

$$C = \frac{I\,t}{V} \tag{Eq. 2.11}$$

Where C is the capacitance in farads (F), I is the applied current in amperes (A), t is the discharge time in seconds (s), and V is the potential window in volts (V).

The specific capacitance (C_{sp}), in farads per gram (F/g), is found by dividing the capacitance *C* by the mass (m) of the electrodes in grams (g).

$$C_{sp} = \frac{I\,t}{V\,m} \tag{Eq. 2.12}$$

Energy is expressed in Wh and is given by the formula.

$$E = \frac{1}{2}CV^2 \tag{Eq. 2.13}$$

The specific energy is expressed in Wh kg^{-1} and is given by the formula.

$$E_{sp} = \frac{1}{2}\frac{CV^2}{m} \qquad \text{(Eq. 2.14)}$$

Power is the energy per unit of time and is expressed in W kg^{-1}.

$$P = \frac{E}{t} \qquad \text{(Eq. 2.15)}$$

The specific power is expressed in Wh kg^{-1} and is given by the formula.

$$P_{sp} = \frac{E}{t\,m} \qquad \text{(Eq. 2.16)}$$

A representation of specific power versus specific energy, called Ragone plot, allows us to compare the performance of different energy storage devices (Figure 2.23). Power and energy are presented in logarithmic scale and the diagonal lines are obtained by dividing the energy by the power, representing characteristic operation timescales.

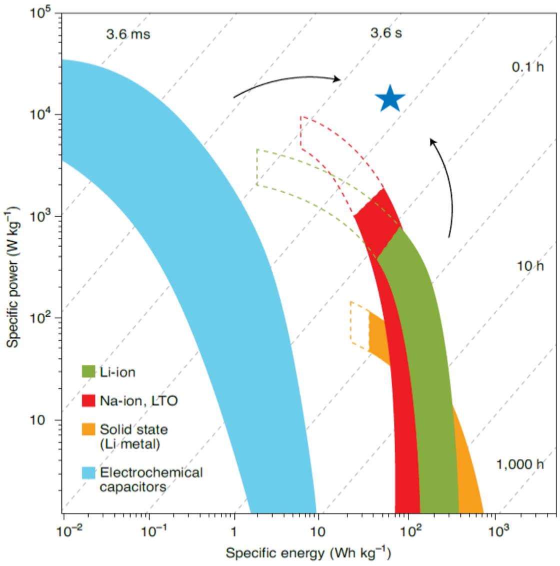

Figure 2.23. Ragone plot [12].

Coulombic efficiency (CE) or Faradaic efficiency is the ratio between the charge supplied and the charge extracted from a capacitor multiplied by 100. The CE can be extracted from the galvanostatic experiments, being greater than 99% in the capacitors, is defined as:

$$\eta_Q = \frac{Q_i}{Q_o} * 100 \qquad \text{(Eq. 2.17)}$$

Voltaic efficiency (VE) is the ratio between the discharge and charge voltage multiplied by 100. There are always losses because the charge voltage is always higher than the discharge voltage, is defined as:

$$\eta_U = \frac{U_i}{U_o} * 100 \quad \text{(Eq. 2.18)}$$

Energy efficiency (EE) is the ratio between the discharged energy and the energy needed to charge a capacitor multiplied by 100. It is one of the most important parameters to study in energy storage devices and is defined as the product of the coulombic and the voltage efficiencies as:

$$\eta_E = \eta_Q \cdot \eta_U \quad \text{(Eq. 2.19)}$$

2.5.3 Electrochemical impedance spectroscopy

Impedance (Z) is the ability of a system to oppose (resist) the flow of electric current. Electrochemical impedance spectroscopy (EIS) is an electrochemical technique that applies a low-amplitude sine wave, usually 10 mV, over a wide frequency range, usually between 10^{-2} and 10^6 Hz; the excitation signal can be expressed as a function time as:

$$E_t = E_0 \sin(\omega t) \quad \text{(Eq. 2.20)}$$

where E_t is the time dependent potential, E_0 is the amplitude of the signal, expressed both in V, and $\omega = 2\pi f$, where ω is the angular frequency, expressed in rad/s, and f is the frequency, expressed in Hz. The system measures the resulting alternating electrical current, $I_{t,}$ shifted in a phase, φ, and a current amplitude I_0 and can be expressed as:

$$I_t = I_0 \sin(\omega t + \varphi) \quad \text{(Eq. 2.21)}$$

Like in Ohm's law, it can be calculated the impedance of the system as:

$$Z_t = \frac{E_t}{I_t} = \frac{E_0 \sin(\omega t)}{I_0 \sin(\omega t + \varphi)} = Z_0 \frac{\sin(\omega t)}{\sin(\omega t + \varphi)} \quad \text{(Eq. 2.22)}$$

We can express the impedance as a magnitude Z_0 and a phase shift φ.

By applying Euler's formula that relates trigonometric and exponential functions, it is possible to go from an expression of impedance in the time domain to an expression in the frequency domain and could be expressed as a vector in the complex plane:

$$Z(\omega) = Z_0 \exp(j\Phi) = Z_0 (\cos\Phi + j \sin\Phi) \quad \text{(Eq. 2.23)}$$

Complex impedance can be separated into two parts, the real impedance Z' and the imaginary impedance Z'' as:

$$Z(\omega) = Z'(\omega) + j\,Z''(\omega) \quad \text{(Eq. 2.24)}$$

Where the real part is the resistive contribution, and the imaginary part is the sum of the inductive (L) and the capacitive (C) contributions, each given by:

$$Z'(\omega) = R \quad \text{(Eq. 2.25)}$$

$$Z_L''(\omega) = \omega L \quad \text{(Eq. 2.26)}$$

$$Z_C''(\omega) = -\frac{1}{\omega C} \quad \text{(Eq. 2.27)}$$

EIS data can be analysed as an electrical circuit, which, in the case of an ideal capacitor, is composed of resistances and capacitances. In the real case, the most appropriate equivalent electrical circuit is the Randles circuit [55], with different elements such as resistances (R), constant phase elements (CPE), which replaces the capacitor (C) for a non-ideal device, and a Warburg impedance (W) (Figure 2.24). It should be noted that different circuits can model the same impedance, so we must always look for the circuit that has a physical meaning, considering electrodes, electrolyte, current collectors and separator [56].

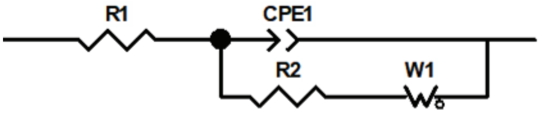

Figure 2.24. Randles equivalent electrical circuit.

The EIS technique generates an impedance spectrum from which information can be extracted about the kinetics of the processes at the electrode-electrolyte interface for a battery system. Impedance is usually given in the Nyquist plot form, the negative of the imaginary versus the real part of the complex impedance. In the Nyquist plot, most elements can be identified and related to the parts of an electrical circuit (Figure 2.25). The equivalent series resistance (ESR), also called solution resistance Rs, is due to the resistance of the electrolyte to the movement of ions and the resistance of the cell cables and connections. Charge transfer resistance (CTR) appears when an electron is transferred from one compound to another in a kinetically controlled oxidation-reduction reaction, and it can be modelled as a resistance parallel to a capacitance. A 45-degree line can be identified as a Warburg resistance (W) related to the concentration and diffusion of species in the electrolyte. It can be modelled in series with a resistance (R2) and parallel to the capacitance, or CPE1, for a non-ideal system (depressed semicircle). A vertical line can be identified as the electrochemical double layer (EDL), modelled by a capacitor, or a constant phase element (CPE).

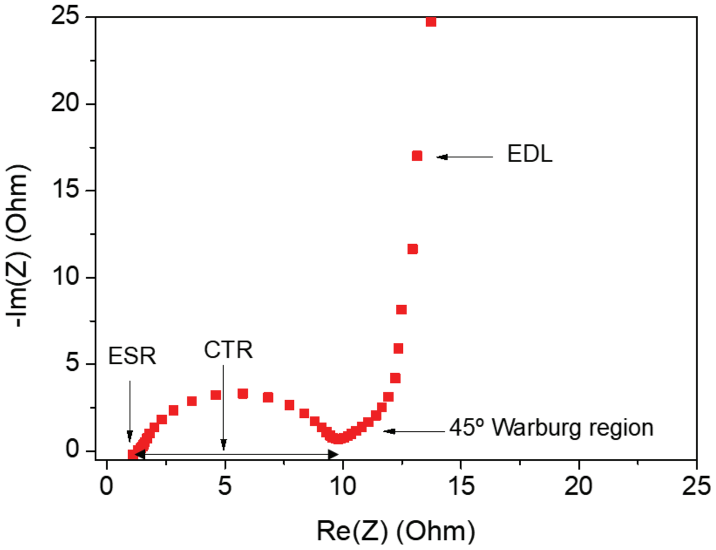

Figure 2.25. Nyquist plot impedance of a supercapacitor and its elements.

3 Electrode and component optimisation using YP50 and 1M KOH electrolyte

3.1 Introduction

In commercial supercapacitors, the most commonly used carbon materials for electrode manufacturing are high-surface area carbons such as activated carbon, carbon nanofibers, carbon nanotubes, and graphene [57]. Additionally, some commercial capacitors are also produced using carbon derived from biomass sources, which offers a sustainable and cost-effective alternative. Biomass-based carbons have gained attention due to their renewable nature, adjustable porosity, and potential for high performance, making them an increasingly viable option for environmentally friendly supercapacitor production [58]. These high-surface area materials have the ability to accumulate charges on their surface forming a double layer, giving its name to electrochemical double layer capacitors (EDLC). The electrodes are usually manufactured by mixing this high surface area material, the active material, with conductive carbon, such as carbon black or acetylene black, and a binder, such as polytetrafluoroethylene (PTFE) or polyvinylidene fluoride (PVDF), in a variable proportion (for example: 85% active material, 10% conductive, 5% binder). In commercial capacitors, this paste is deposited on a metal sheet, usually aluminium, which acts as the current collector [59]. In this chapter, self-supporting electrodes have been manufactured, thereby avoiding the use of aluminium sheets, resulting in a reduction in weight and materials, which in turn contributes to lowering the final cost of the capacitor. A membrane soaked with an electrolyte is placed between the electrodes, preventing short circuits but allowing the passage of ions. The most commonly used membranes in research are polyamide (PA), polypropylene (PP), fibreglass (GF), and cellulose [60]. In commercial capacitors typical membranes are made from polyethylene terephthalate (PET), polypropylene (PP) or polyethylene naphthalate (PEN) [61]. Commercial capacitors typically use organic [62] or aqueous [63] electrolytes , while both of these, along with the so-called ionic liquids, are frequently used in research applications [64]. In state-of-the-art aqueous capacitors, electrolyte composition, voltage window, capacitance, energy, and cyclability are typically presented to demonstrate improvements (Table 3.1).

Table 3.1. State-of-the-art of YP50 activated carbon aqueous supercapacitors.

Electrolyte	**Voltage (V)**	**Electrode capacitance F/g (only active material)**		**Cycles**	**Energy (J/g)**		**Reference**
		5-20 mV/s	**200 mV/s**		**5-20 mV/s**	**200 mV/s**	
0.5 M H_2SO_4	1.2	96	-	-	69	-	[85]
0.5 M KOH	1.3	87	-	-	74	-	[85]
0.5 M Li_2SO_4	1.8	61	-	-	99	-	[85]
6 M KOH	1	157	134	2,000	79	67	[86]

In this chapter we explore the use of aqueous electrolytes as an alternative to organic electrolytes as they are cheaper, safer, easier to handle and environmentally friendly.

Supercapacitors, like batteries, are energy storage devices. Compared to batteries, SCs provide higher power, longer cycle life, and can operate across a wider temperature range. However, batteries offer higher specific energy and maintain an almost constant voltage during discharge (Table 3.2).

Table 3.2. Comparative of commercial Li-ion batteries, lead-acid batteries and supercapacitors [65].

Energy Storage	Li-Ion Battery	Lead-AcidBattery	EDL Capacitors
Specific Power (W/Kg)	3000	250	14000
Specific Energy (Wh/Kg)	100-200	30-100	1-10
Cycle life	250-1000	500-1000	10^6
T Range (° C)	0 to 60	0 to 40	-40 to 60

Energy efficiency (η_E) is one of the most important parameters in energy storage devices. It is defined as the ratio between the energy supplied by the device during discharge and the energy it absorbs during charge multiplied by 100.

$$\eta_E = \frac{Energy_{discharge}}{Energy_{charge}} * 100 \qquad \text{(Eq. 3.1)}$$

The maximum energy efficiency can reach 95% in supercapacitors [59], 90% in Li-ion batteries [66], and 70% in lead-acid batteries [67]. However, factors such as the potential window, scanning rate, and temperature, influence the final energy efficiency of the device, which is a key limitation to power density [54], as it requires a very high energy supply in a short time. Energy efficiency drops to 85% in supercapacitors for discharge times under 20 seconds [59], whereas in lithium-ion batteries, this occurs at discharge times of 15 minutes and decreases to 55% in lead-acid batteries for the same discharge time [68]. This makes capacitors essential elements in electric vehicle or train applications such as energy recovery brake systems [59].

This chapter aims to optimise manufacturing conditions for symmetric supercapacitors based on activated carbon in a basic medium. Subsection 3.2 discusses the mass balance between the positive and negative electrodes, followed by subsection 3.3, which discusses the effect of applying different temperatures to the electrodes during processing. Subsection 3.4 presents the influence of the separator on supercapacitor performance, and subsection 3.5 includes a preliminary study on symmetric supercapacitor degradation, which is relevant to component optimisation for performance enhancement.

3.3 The influence of the mass balance

In this section, we study the effect of mass balance on the performance of symmetric supercapacitors assembled using self-standing YP50 electrodes prepared using Teflon as binder (section 2.2.1 recipe 1), standard 1 M KOH aqueous electrolyte (defined in section 2.2.2), and non-commercial glass fibre (GF) membrane in coin cells (defined in section 2.2.3).

Symmetrical capacitors have the same mass on both electrodes, which is the usual arrangement in commercial capacitors [62]. However, some works justify the benefits of the mass balance between the cathode and the anode. Anions and cations, together with their hydration shell, have different diameters, which would prevent them from taking advantage of their maximum capacitance as neither the electrodes nor the electrolyte are fully used [69]. To calculate the mass ratio, they give the formula:

$$\text{electrode mass ratio} = \frac{m_+}{m_-} = \frac{n_- \cdot r_-}{n_+ \cdot r_+} \qquad \text{(Eq. 3.2)}$$

Where m_+ and m_- are the mass of the positive and the negative electrodes, n_+ and n_- are the number of positive and negative ions and r_+ and r_- are the hydrated radius of positive and negative ions, respectively. In their experiments, they report an increase of the capacitance in different aqueous electrolytes, finding best results for mass ratios of 0.75 for Na_2SO_4 and H_2SO_4 acidic electrolytes and 0.86 and 1 for NaOH and KOH basic electrolytes [69].

Other works also use the balance of the cathode/anode mass ratio to improve the performance due to the extension of the potential window of asymmetric capacitors with a mass ratio of 2.46 in 0.5 M K_2SO_4 neutral electrolyte [70] or reduction of diffusion and charge transfer resistances in Li-ion capacitors based on activated carbon (AC) and $Li_4Ti_5O_{12}$ (LTO), finding an increase in the performance and cycling stability when the mass ratio of AC/LTO was 0.72 in 1 M $LiPF_6$ organic electrolyte [71].

Using the values of K^+ and OH^- hydrated radius given in [69], we find the theoretical mass ratio of KOH basic aqueous electrolyte.

$$\frac{m_+}{m_-} = \frac{1 \cdot 0.3}{1 \cdot 0.331} = 0.9 \qquad \text{(Eq. 3.3)}$$

To study the influence of the mass balance in symmetrical capacitors, coin cells with different mass ratios between the positive and negative electrode (m_+/m_-) were fabricated and tested electrochemically using impedance spectroscopy, cyclic voltammetry (CV) and long cycle galvanostatic charge-discharge aiming to optimise supercapacitor performance.

Coin cells with mass ratios between 1.8 and 0.6 were considered. The cells were activated using cyclic voltammetry (CV) with sets of 10 cycles at a scan rate of 5 mV/s between 0 and 0.5 V, increasing the upper voltage in steps of 0.1 V in each set until reaching 1.2 V. After the activation process, the cells were cycled from 0 V to different cut-off voltages of 1.2 to 1.6 V, with a current density of 1 A/g (Figure 3.1), and impedances interspersed between each cycle (Figure 3.2). Energy efficiency (EE) was checked as the key parameter [72] in galvanostatic experiments. It depends on the applied current and potential, decreases when the current intensity increases and increases when the potential window is reduced, especially if the total discharge of the capacitor is avoided. In commercial capacitors, energy efficiency of up to 95% can be achieved when operating at nominal current, which is drastically reduced to less than 85% under higher current conditions [73].

EE usually occurs for a maximum voltage between 1.2 and 1.3 V for all the mass ratios, been around 75% for mass ratios of 1.8 and 1.5, 80% for 1.24 and 82% for 0.6 (Figure 3.1). When the voltage window is gradually increased to 1.6 V, the energy efficiency decays to 67% for 1.5 mass ratio, 73% for 1.8 and 1.24 mass ratio, and 78% for the mass ratio of 0.6. We fix the maximum voltage window in 1.6 V after finding a degradation in the cell response and even a failure in some cells when we try to go beyond this value.

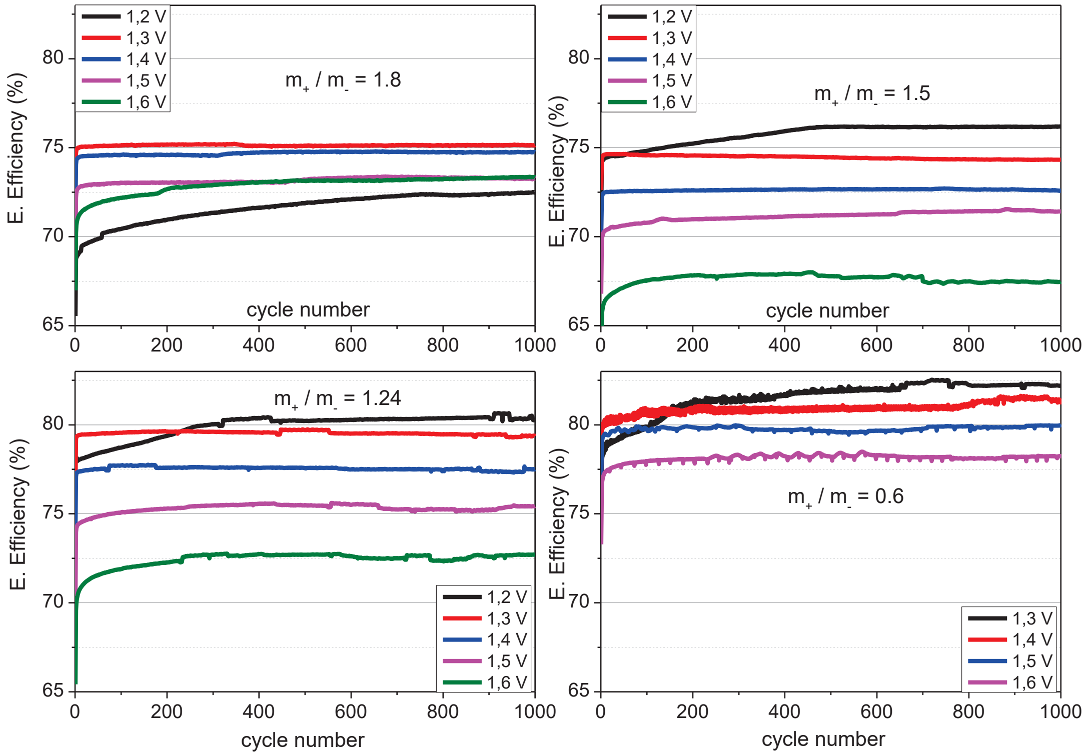

Figure 3.1. Energy efficiency of 1,000 galvanostatic charge-discharge cycles since 1.6 V for different mass ratio cells.

Energy efficiency values can be related to the impedances interspersed between charge and discharge experiments (Figure 3.2). Impedance is usually separated into three components. The first is the ohmic or series resistance (Rs), related to electronic and electrolyte resistance [74], which corresponds to the high-frequency interception with the real Z axis in the left part of the graph. This R_S corresponds to R1 in the Randles circuit presented in Figure 2.24. For coin cells cycled at 1.4 V, Rs increased from 0.7 to 5.5 Ohms for the cell with a mass ratio of 1.5. At 1.5 V, Rs increased from 3 to 9 Ohm and from 5.5 to 10 Ohm for cells with mass ratio 1.8 and 1.5 respectively. The cells with mass ratios 1.24 and 0.6 did not suffer any increase in Rs when the voltage increased to 1.6 V. The second component of the impedance is related to the width of the semicircle, is the charge transfer resistance (CTR), and corresponds to the Faradaic current related to electron transfer between electrode and electrolyte [75]. CTR usually decreases in the first cycles of the so-called activation process, and then stabilizes on cycling [76]. In our experiments, Figure 3.2, the CTR component remains stable with values around 8.5, 5.5, 6.5, and 4 Ohms for mass ratios 1.8, 1.5, 1.24, and 0.6 up to 1.6 V, except for the mass ratio 1.8, which doubled its value from 8.7 to 16.9 Ohms.

At lower frequencies appears an inclined line corresponding to Warburg impedance, linked to the diffusion of ions, followed by a pure capacitive response represented as a vertical tail. Figure 3.2 shows that the transition zone between the end of CTR and the capacitive zone is very small for all the samples, as expected for a supercapacitor. The almost vertical tail shows the capacitive behaviour of all mass ratios, however, for the device with a mass ratio of 1.8, the tail moves away from verticality for 1.6 V with a huge increment in the real part of impedance, with a value of 68.9 Ω, while it obtained a value of 28.5, 18.9 and 16.4 for the mass ratios 1.5, 1.24 and 0.6, respectively, been the last one the lowest value of all mass ratios.

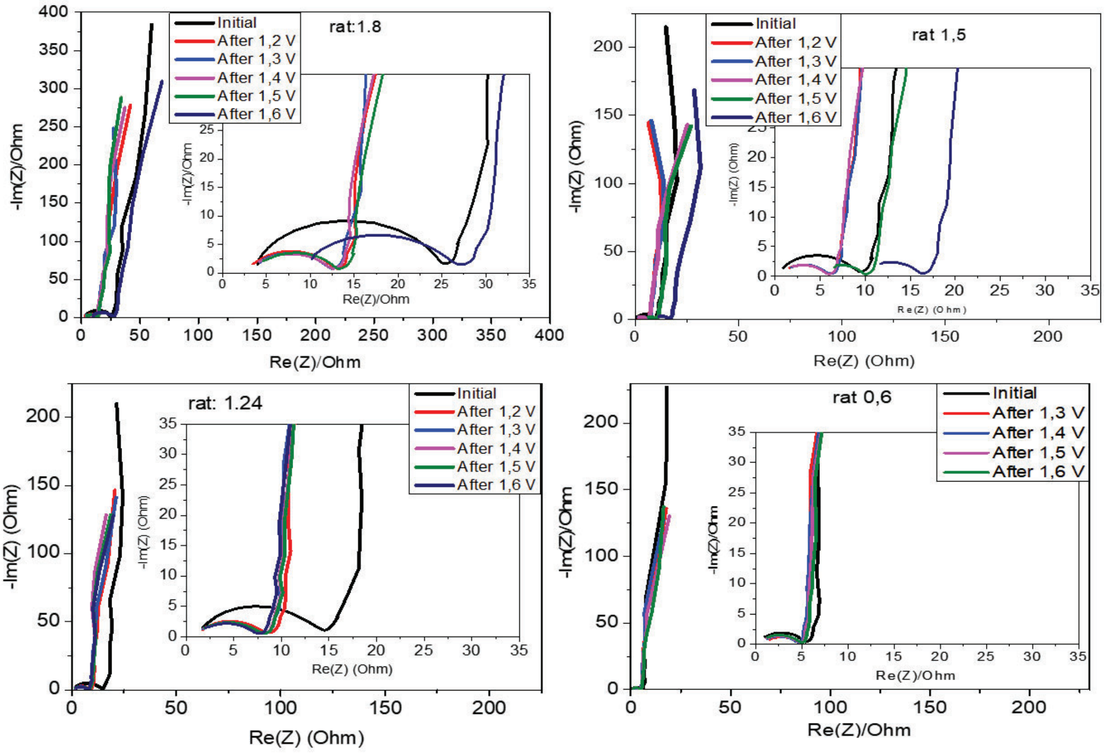

Figure 3.2. Impedance plots measured after cycling at different cutoff voltages for different mass ratio.

To have a better perspective of the impedances, Rs and CTR are plotted as a function of voltage (Figure 3.3). The cell with a mass ratio of 1.8 shows large Rs for low voltage values and a great increase in CTR when the potential window reaches 1.6 V. The cell with a mass ratio of 1.5 suffered a large increase in Rs for 1.5 and 1.6 V, although it kept the CTR unchanged even for 1.6 V. On the other hand, the cells with mass ratios of 1.24 and 0.6 barely suffered variation in the Rs and CTR, even when reaching 1.6 V, having the cell with a mass ratio of 0.6 the smallest total resistance with values of 0.7 Ω for ESR and 4 Ω for CTR, similar to those found in the literature [77].

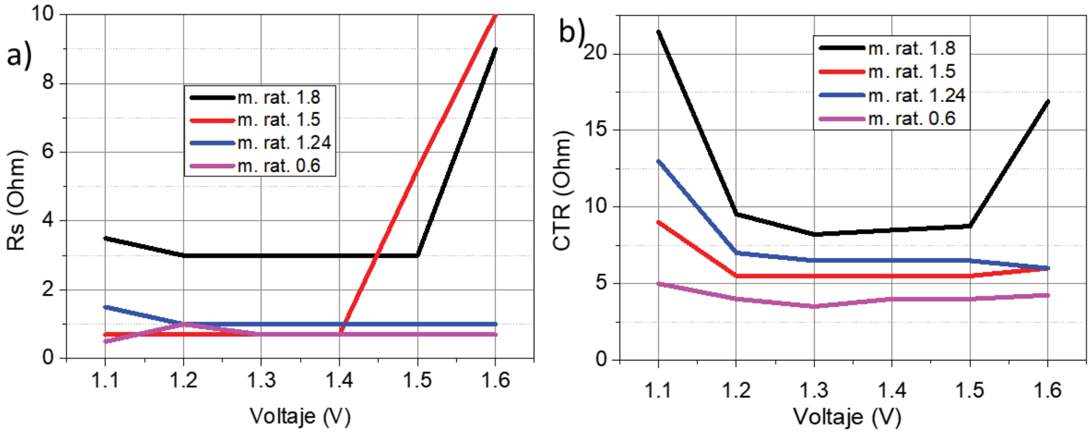

Figure 3.3. a) Rs and b) CTR values as a function of voltage for different mass ratios.

In this section, we have studied how mass balance can modulate the performance of a supercapacitor by reducing the impedance and improving energy efficiency. In our system using electrodes based on YP50 activated carbon in the basic electrolyte 1 M KOH, we found that the ratio m+/m- = 0.6 obtained the best results, maintaining a high energy efficiency close to 80% and low impedance, even at a voltage of 1.6 V.

3.4 Thermal processing of the electrodes

In all electrochemical systems, capacitance decreases as scan speed increases, which limits charge and discharge times. Therefore, increasing the retained capacitance when increasing the scanning speed is one of the biggest challenges. We investigated the effect of subjecting the electrodes to thermal treatment to increase scanning speed and reduce charge and discharge times. Thermal treatment is a process that consists of heating the electrodes in a furnace at a given temperature for the desired time in a controlled atmosphere. Thermal treatment at relatively low temperature can be used to increase the conductivity and optimize the electrodes by thermal annealing and the elimination of carboxylic groups [78].

Symmetric supercapacitors were assembled using self-standing YP50 electrodes prepared using Teflon as binder (section 2.2.1 recipe 1), standard 1 M KOH aqueous electrolyte (defined in section 2.2.2), and non-commercial glass fibre (GF) membrane in coin cells (defined in section 2.2.3).

Since PTFE is stable at 250 ºC and has its melting point above 330 ºC [44], four batches of electrodes were prepared and treated at 60 ºC, 200 ºC, 240 ºC, and 300 ºC for 1 hour in Ar atmosphere. The samples treated at 60 °C, 200 °C, and 240 °C had a similar appearance and good consistency. However, the sample treated at 300 ºC had to be handled carefully because it became brittle.

The cells were activated by applying 10 cycles of cyclic voltammetry (CV) with a scanning speed of 5 mV/S in the range of 0.5-1.2 V with steps of 0.1 V. After activation process, the device was cycled at scan rates of 5, 10, 20, 50, 100, and 200 mV/s, with 10 CVs performed at each rate, within a voltage window of 1.2 V.

Figure 3.4 shows CV plots of symmetric coin cells assembled using electrodes thermally treated at 60 ºC, 200 ºC, 240 ºC, and 300 ºC. When increasing the rate from 5 to 200 mV/s, CVs retained the almost typical square shape of capacitors for all the samples. Regarding the loss of capacitance when increasing the scanning speed from 5 to 200 mV/s, the capacitance retention was of 60% for 60 ºC, 68% for 200 ºC, 71% for 240 ºC and 78% for 300 ºC (Figure 3.4). The high-rate experiments at 1.2 V showed a direct relationship between the retained capacitance and the temperature increase of the electrodes.

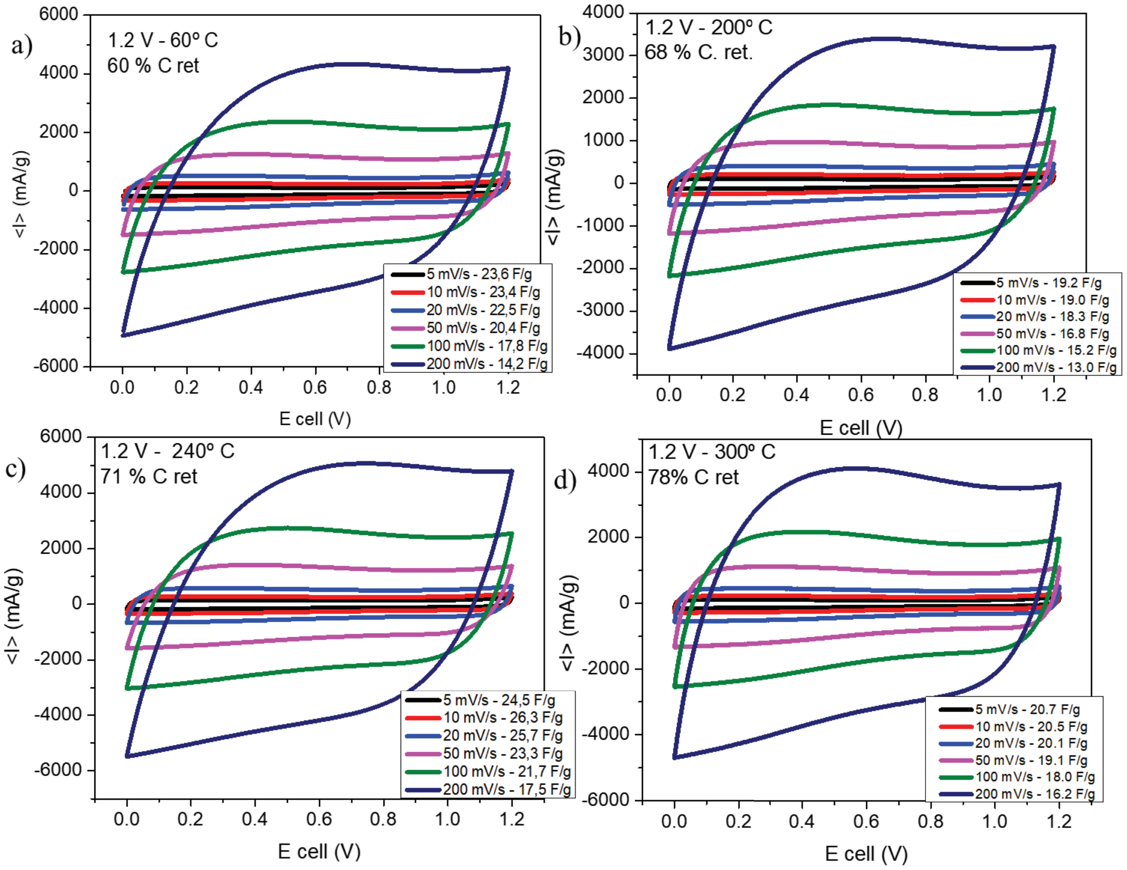

Figure 3.4. High-rate CVs and capacitance retained at 1.2 V for electrodes treated at a) 60 °C, b) 200 °C, c) 240 °C and d) 300 °C.

After cycling at 1.2 V, the cells were measured at higher voltages of 1.3, 1.4, 1.5 and 1.6 V, Figure 3.5, and impedance data sets were measured between each voltage series, Figure 3.6. A significant fact was that all the cells increased the capacitance as the potential window was increased. This seems to be due to better access of the ions to the pores and the appearance of faradaic reactions, observable in the shape of the discharge curve in the CV, that move away from the typically square shape of supercapacitors (Figure 3.5). The capacitance retained when the rate is increased from 5 to 200 mV/s in a voltage window of 1.6 V was 54% for 60 °C, 59% for 200 °C, 73% for 240 °C and 72% for 300 °C. Compared to the capacitance retained at 1.2 V, we observe a 10% drop for all temperatures except for 240 ºC with a slight increase of 1% and a large cell capacitance of 24.2 F/g at 200 mV/s.

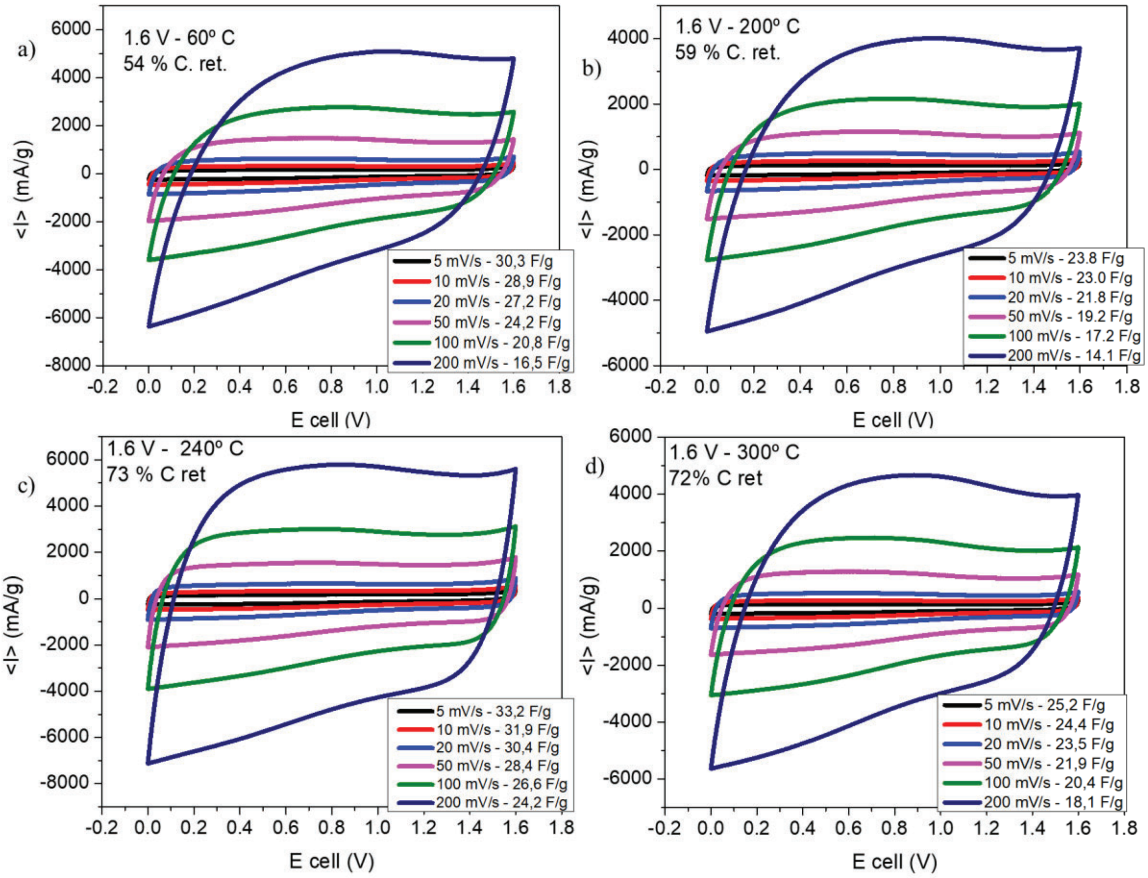

Figure 3.5. High-rate CVs and capacitance retained at 1.6 V for electrodes treated at a) 60 °C, b) 200 °C, c) 240 °C and d) 300 °C.

Impedance measurements were used to control how the potential window and electrode thermal treatment affect the value of charge transfer resistance (CTR). As CTR corresponds to the semicircle diameter that appears in impedance at high frequencies, it can be used to describe the evolution of the cells during cycling. It has been established that an increase in the electrical conductivity of the electrodes leads to a reduction in the CTR [79]. In this sense, we will try to relate our thermal treatment with the reduction in CTR and its relationship with cell performance.

After the activation process, all the cells show a reduction in the CTR in each cycling series, reaching a minimum at 1.4 V, Figure 3.6. When the potential increases to 1.5 and 1.6 V, the CTR increases for cells containing electrodes treated at 60 ºC and 300 ºC. Cells assembled using electrodes treated at 200 ºC show a small increment. For samples at 240 ºC, the CTR slightly decreases at 1.6 V. The lowest CTR values are obtained for the cell assembled with the electrodes treated at 240 ºC (Figure 3.6). A graph of CTR values versus voltage for coin cells containing thermally treated electrodes is presented in Figure 3.7 and Table 3.3. The CTR for the sample thermally treated at 240 ºC remains fairly unchanged, with a final value of 3.4 Ohms at 1.6 V, similar to literature [77].

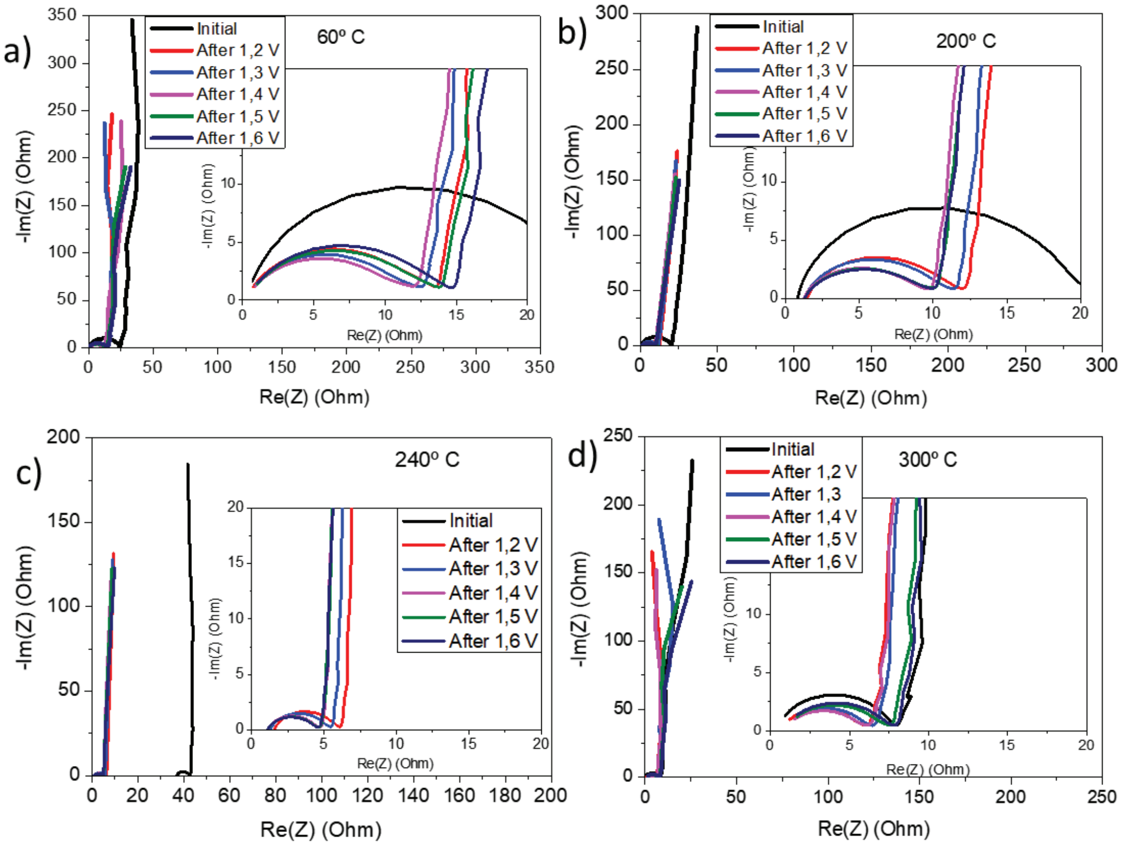

Figure 3.6. Impedance plots after high-rate series from 1.2 to 1.6 V for electrodes treated at a) 60 °C, b) 200 °C, c) 240 °C and d) 300 °C.

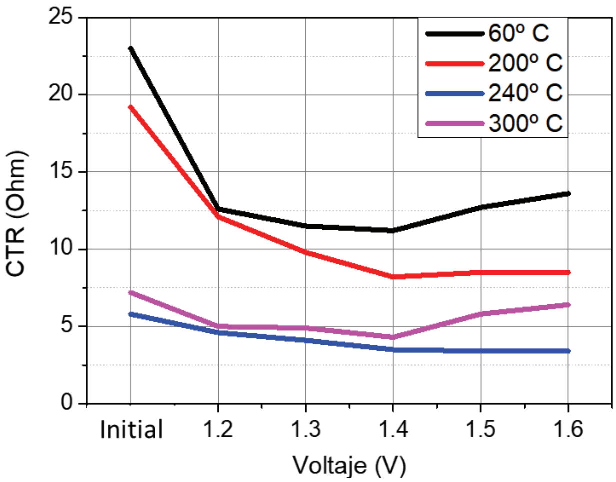

Figure 3.7. CTR values after high-rate series until 1.6 V for electrodes treated at 60 °C, 200 °C, 240 °C and 300 °C.

Table 3.3. CTR values after high-rate series.

	Initial	1.2 V	1.3 V	1.4 V	1.5 V	1.6 V
60° C	23	12.6	11.5	11.2	12.7	13.6
200° C	19.2	12.1	9.8	8.2	8.5	8.5
240° C	5.8	4.6	4.1	3.5	3.4	3.4
300° C	7.2	5	4.9	4.3	5.8	6.4

The samples were subjected to gas physisorption analysis, FTIR spectroscopy, XRD, and XPS studies to correlate their electrochemical and electrical performance with the thermal treatment effect. Gas physisorption was used to study the surface area, pore volume and pore size, and results are presented in Table 3.4. The average surface area for samples prepared at different temperatures is 1092 m^2/g, so there is no significant difference between the samples. However, there is a considerable reduction of approximately 25% of the surface area compared to the active material YP50, noting that YP50 constitutes 85% of the weight of the electrodes. This difference is attributed to the partial blocking of small pores by Super P particles. Single point adsorption gives a total pore volume of 0.57 cm^3/g with a reduction of 13% compared to the active material YP50. The BJH adsorption method used to find the pore size does not show significant differences between the two lowest temperatures, with an average of 4.88 nm. However, for higher temperatures of 250 ºC and 300 ºC, pore sizes are 5.19 nm and 5.44 nm, respectively. The increase in pore size can be attributed to a more even distribution of small Super P particles, likely caused by a partial melting of the binder, which blocks smaller pores.

Table 3.4. Surface area, pore volume and pore size of YP50 and electrodes prepared at different temperatures.

	B.E.T. m^2/g	pore V (cm^3/g)	pore size (nm)
YP50	1683.42	0.77	3.80
110° C	1099.51	0.57	4.91
200° C	1106.50	0.56	4.85
250° C	1065.59	0.56	5.19
300° C	1097.86	0.59	5.44

The Fourier Transform Infrared Spectroscopy (FTIR) was discussed in chapter 2 for YP50 and electrode made at 110 ºC. Figure 3.8 presents the FTIR spectra of samples treated at different temperatures, all of which exhibit a similar pattern. The most significant changes with the increasing temperature occur at the band around 1200 cm^{-1}, which becomes sharper, and the band around 1140 cm^{-1}, which diminishes. These bands correspond to asymmetrical and symmetrical stretching of CF_2 coming from PTFE binder [48], been assigned the changes to degradation caused by partial melting and redistribution of the binder at elevated temperatures. Additionally, the fingerprint region (low wavenumber) becomes flatter, with a reduction in band around 500 cm^{-1}.

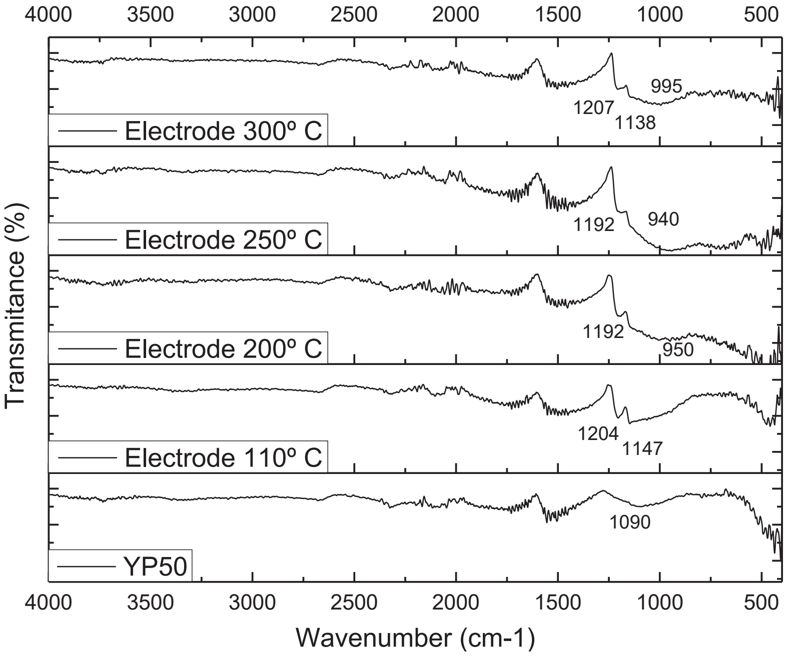

Figure 3.8. FTIR spectrum of electrodes treated at different temperatures and YP50.

All the samples were analysed using X-Ray Diffraction (XRD), and the results are shown in Figure 3.9. The XRD spectra do not reveal any significant patterns associated with the various thermal treatments. The (0 0 2) peaks, located at 23º and 24º, show similar 2theta position across all samples, but appear closer together and are difficult to separate for 300 ºC. The (1 0 0) peak at 43º appears flattened and difficult to distinguish in all the analysed samples. The peaks appearing at 21º, 26º, 36º and 54º were attributed to the PTFE binder, appearing sharper for the 300 ºC electrode, which is associated with an increase in crystallinity [80].

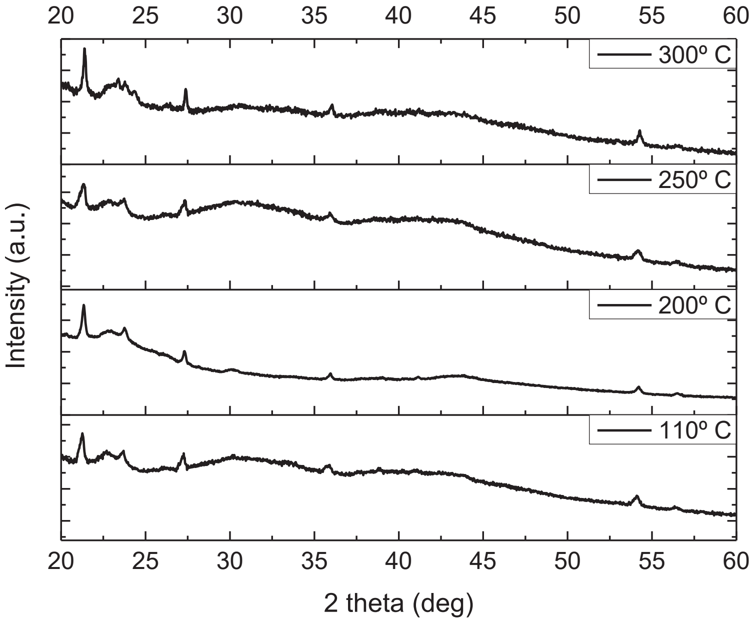

Figure 3.9. XRD spectrum of electrodes treated at different temperatures.

XPS technique was also used to investigate thermally treated electrodes, and results are presented in Figures 3.10, 3.11 and 3.12. The C1s spectrum [81] (Figure 3.10) shows similar behaviour for 110 ºC, 200 ºC and 250 °C, while for 300 °C it shifts towards higher energies. Additionally, fittings for the 284.5 and 289 eV peaks for the sample prepared at 300 °C show a decrease in C=C and C-C bonds and an increase in C-O and C=O bonds, respectively. That would reinforce the idea of the loss of mechanical stability of the sample treated at 300 °C due to oxidation.

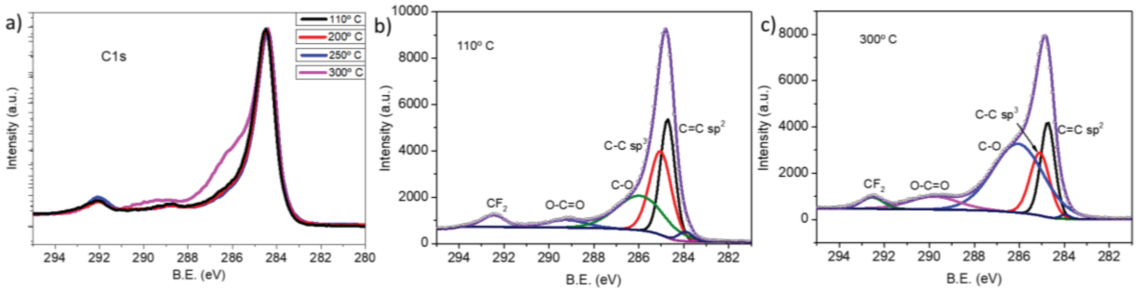

Figure 3.10. C1s XPS spectra. a) Composition of all electrodes treated at different temperatures, b) Peak fitting for 110 °C, c) and 300 °C.

The XPS O1s spectrum, Figure 3.11, following deconvolution made in [82], shows a small peak around 531 eV corresponding to C=O groups and a peak at 532 eV corresponding to C-OH and C=O groups that decreases for higher temperatures and almost disappear for 300 ºC. The main peak at 533 eV corresponds to C-O-C groups and increases with temperature. The broad peak observed between 535 and 540 eV corresponds to COOH groups and adsorbed water or chemisorbed oxygen [15], and it decreases in intensity and shifts towards lower energy binding when the temperature increases. This peak practically disappears at 300 ºC.

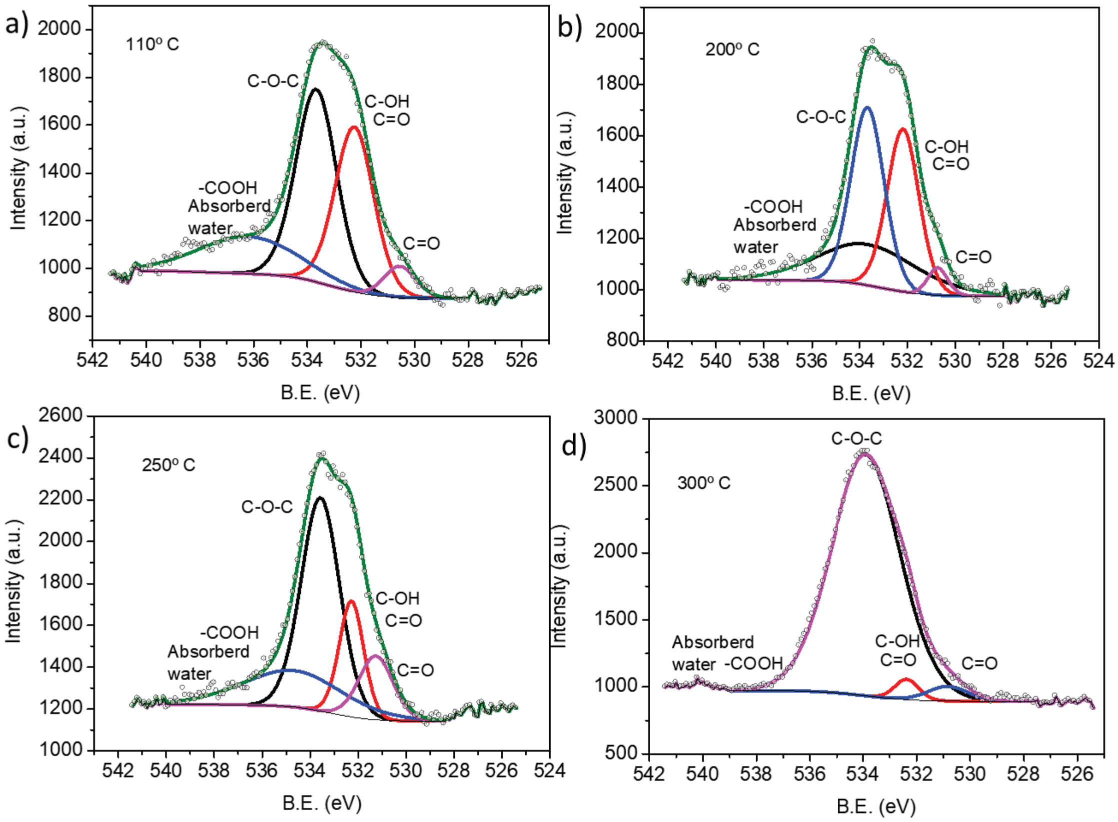

Figure 3.11. O1s XPS spectra of electrodes treated at different temperatures: (a) 110 °C, (b) 200 ºC, c) 250 ºC and d) 300 °C.

The F1s spectrum of XPS, Figure 3.12, shows a broadening towards higher binding energies for 110 ºC, which is related to the intercalation of CF_3 molecules in the CF_2 chain of PTFE [83] and O-F bond [84]. As temperature increases, the widening of the peak diminishes with a reduction of oxygen content and an increase in crystallinity [80]. This is associated with the improved performance of electrodes treated at higher temperatures.

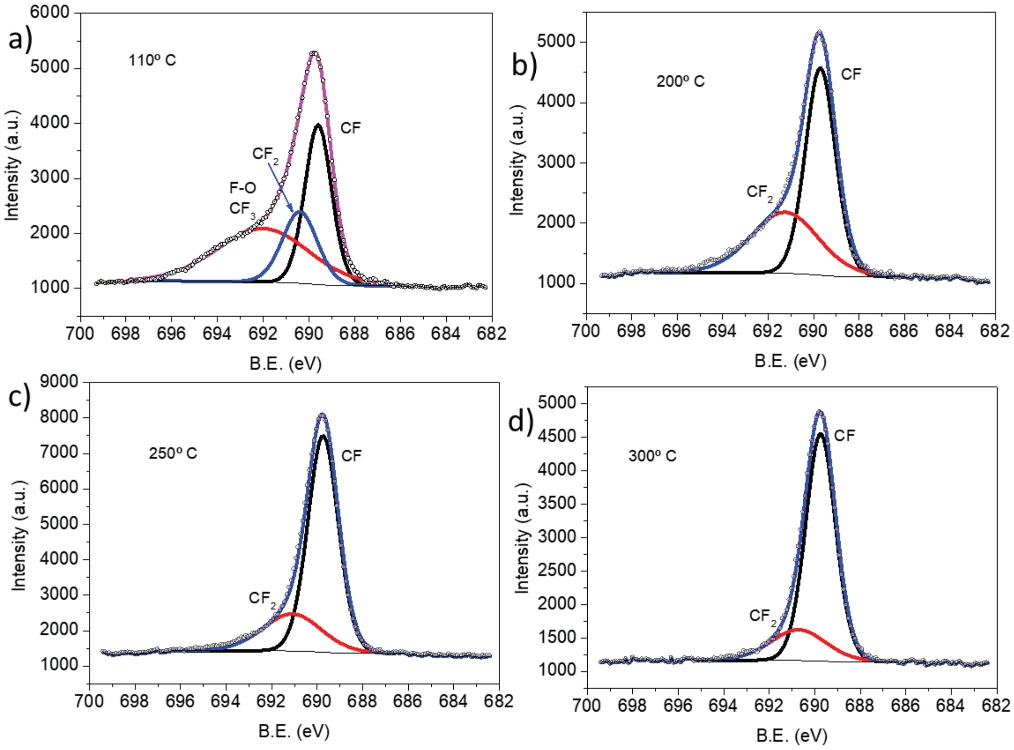

Figure 3.12.. F1s XPS spectra of electrodes treated at different temperatures: (a) 110 °C, (b) 200 ºC, c) 250 ºC and d) 300 °C.

In this section, we discuss the effect of electrode thermal treatment on the electrical and electrochemical performance of the coin cell. As the temperature increases to 240 ºC, the electrical conductivity increases, which can be followed by reducing the CTR value in the impedance plots. The reduction in CTR with temperature is accompanied by increased capacitance at high rates and an increase in the potential window. The best results are found for the electrodes treated at 240 ºC, which show no changes in impedance even when the sample is cycled at 1.6 V, delivering a capacitance of 33.2 F/g at 5 mV/s and 24.2 F/g at 200 mV/s with a capacitance retention of 73%.

As conclusion, is shown in Table 3.5 a comparison with other works that use the same active carbon, YP50 [85], [86]. The combination of high capacitance with a large potential window leads to higher values in terms of stored energy, 200 J/g at 5 mV/s and 146 J/g at 200 mV/s, than those presented in the literature.

Table 3.5. Comparison of different capacitors that use YP50 activated carbon.

Electrolyte	**Voltage (V)**	**Electrode capacitance F/g (only active material)**		**Cycles**	**Energy (J/g)**		**Reference**
		5-20 mV/s	**200 mV/s**		**5-20 mV/s**	**200 mV/s**	
0.5 M H_2SO_4	1.2	96	-	-	69	-	[85]
0.5 M KOH	1.3	87	-	-	74	-	[85]
0.5 M Li_2SO_4	1.8	61	-	-	99	-	[85]
6 M KOH	1	157	134	2,000	79	67	[86]
1 M KOH	1.6	156	114	> 10,000	200	146	This work

3.5 The effect of the membrane on electrochemical behaviour

Until now, all the experiments have been carried out with non-commercial fibreglass nanoporous membranes. To test the effect of the membrane on the electrochemical response of coin cells, we considered two commercial membranes widely used in capacitors and batteries: the Celgard 3501 microporous polypropylene (PP) membrane surfactant coated with a thickness of 25 μm and pore size of 0.064 μm and the Whatman GF/C glass fibre (GF) with a thickness of 260 μm and pore size of 1.2 μm.

Symmetric supercapacitors were assembled using self-standing YP50 electrodes prepared using Teflon as the binder (section 2.2.1 recipe 1), standard 1 M KOH aqueous electrolyte (defined in section 2.2.2), and membranes to study their performance in coin cells (defined in section 2.2.3).

The cells were activated by applying 10 cycles of cyclic voltammetry (CV) with a scanning speed of 5 mV/S in the range of 0.5-1.2 V with steps of 0.1 V. After the activation process, the cells were cycled with galvanostatic charge-discharge at 1 A/g in a voltage window between 1.2 and 1.4 V, followed by high-rate CVs between 5 and 200 mV/s in a voltage window between 1.2 and 1.6 V, interspersing impedance measurements between cycles.

In the galvanostatic charge and discharge test, voltage is represented as a function of time. Results for the two membranes are shown in Figure 3.13. The plots show an almost triangular shape with a small drop at the beginning of each slope [87], the so-called voltage drop due to energy losses. Both membranes exhibit a small voltage drop with values of 30 mV and 27 mV for the GF and the PP membranes, respectively. The GF membrane delivers an almost triangular shape, while the PP membrane shows a small bulge. The capacitance was similar for both membranes, although slightly higher for the GF membrane for higher potentials (Figure 3.13).

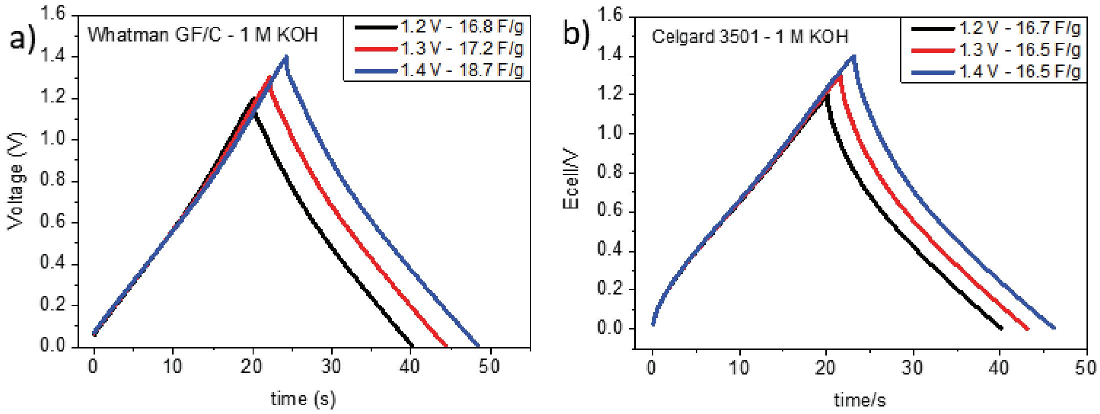

Figure 3.13. Galvanostatic charge-discharge at 1 A/g for membranes a) Whatman GF/C and b) Celgard 3501.

Figure 3.14 shows CV plots of symmetric coin cells, assembled using the two membranes, measured at different scan rates from 5 mV/s to 200 mV/s at 1.2 V. The cell with the GF membrane retains 80.8% of the capacitance, while the cell with the PP membrane retains only 57% of the low rate capacitance.

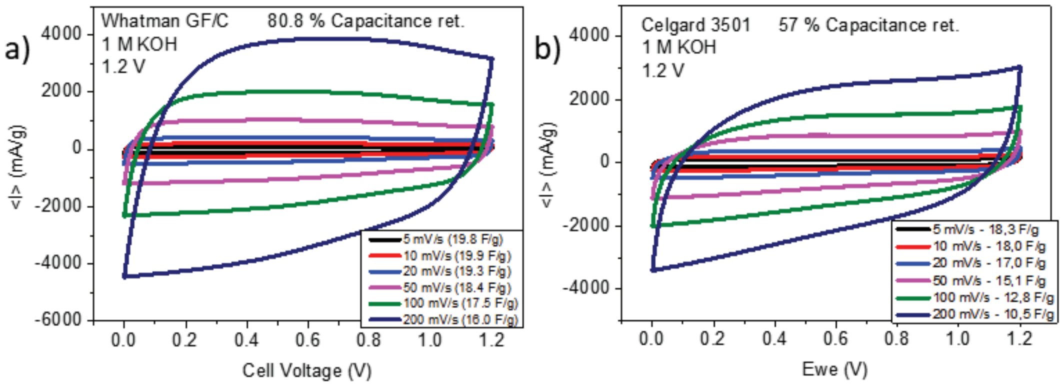

Figure 3.14. Cyclic voltammetry since 1.2 V with a scan rate between 5 and 200 mV/s, a) Whatman GF/C membrane, b) Celgard 3501 membrane.

In the potential scans between 1.3 and 1.6 V, the cell with GF membrane maintains its capacitance at all scanning speeds and its retained capacitance, which is 80.5% (Figure 3.15.a). The device with a PP membrane delivers a capacitance increase of 22% when the potential window increases from 1.2 to 1.6 V. However, when increasing the potential sweep from 5 to 200 mV/s, the capacitance retained is 56%, similar to that obtained in 1.2 V potential window (Figure 3.15.b).

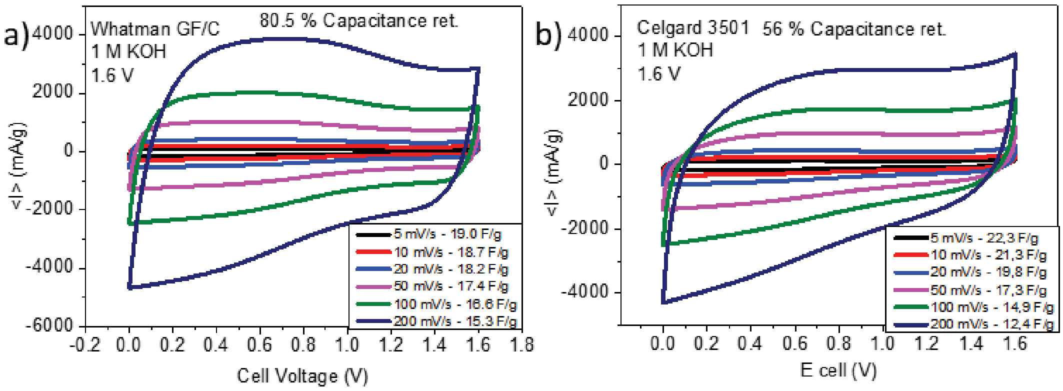

Figure 3.15. Cyclic voltammetry since 1.6 V with a scan rate between 5 and 200 mV/s, a) Whatman GF/C membrane, b) Celgard 3501 membrane.

Impedance plots for the coin cells assembled using Whatman and Celgard membranes are shown in Figure 3.16. The value of ESR for the coin cells is low, less than 1 Ohm. The CTR value is 5 Ohms for the GF membrane and 2 Ohms for the PP membrane. The low CTR of the PP membrane can be attributed to its low electrical impedance, as indicated in the technical specifications [88], and may also be explained by its reduced thickness, which provides a shorter path for ion movement. However, at lower frequencies, the GF membrane undergoes an inflexion of 87º, giving rise to the typical vertical tail of the capacitors. The PP membrane undergoes an inflexion of 69º, its shape is more complex and could be related to a Warburg impedance. Warburg impedance usually appears after CTR as a theoretical 45-degree slope [89] and is related to the diffusion of ions. At even lower frequencies, in the uppermost part of the tail, the PP membrane approaches the vertical behaviour characteristic of capacitive systems, although its final phase angle is 77º, compared to 85º for the GF membrane. The lowest value of the total impedance Z is 174 Ohms for the GF membrane and 180 for the PP membrane, reflecting the fact that the two membranes have similar behaviour at low potential sweep (Figure 3.16).

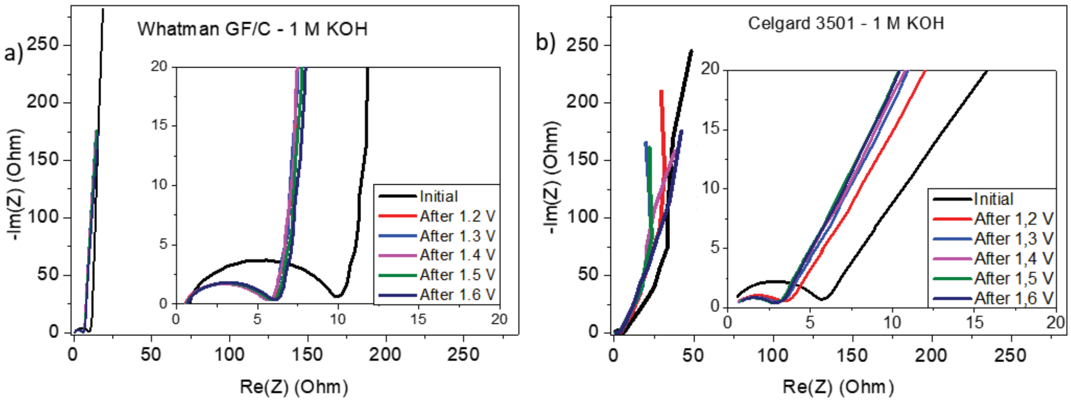

Figure 3.16. Impedance spectroscopy plots of coin cells, a) Whatman GF/C membrane, b) Celgard 3501 membrane.

This section has studied how the membrane influences the supercapacitor performance. The use of PP membranes implies a decrease of rate-capacitance between 20 and 35% compared to the GF membranes. This decrease could be derived from the fact that the PP membrane is less hydrophilic than the GF membrane despite having a surfactant that improves its wettability.

3.6 Preliminary degradation of symmetric supercapacitors

The degradation of capacitors mainly occurs when they are outside their stability window. In supercapacitors, the charge and discharge processes are usually very short, so the capacitor hardly suffers degradation. For this reason, the capacitor can be charged and discharged thousands of times without noticing any signs of degradation, especially if the rate is quite high. Another way to study the degradation of the cell is by ageing experiments through a hold test [90]. Voltage-hold tests with self-discharge studies are less time-consuming than those involving long cycling and afford valuable information on system degradation. In the hold test (or float test), the capacitor is charged up to the desired voltage and remains at this voltage for a certain time. After that, it is disconnected from the current, and the evolution of the potential is studied.

The energy of a capacitor is given by the formula $E = \frac{1}{2} CV^2$. Therefore, it is evident that the easiest way to increase energy is by expanding the potential window of the devices. So, the effect of membrane type on the supercapacitor self-discharge after a hold test was investigated for different voltage windows.

Symmetric supercapacitors were assembled using self-standing YP50 electrodes prepared using Teflon as binder (section 2.2.1 recipe 1) and thermally treated at 300 °C for 1 hour, standard 1 M KOH aqueous electrolyte (defined in section 2.2.2) and the selected membranes: the Celgard 3501 and Whatman GF/C, in coin cells (defined in section 2.2.3).

After activation, capacitors were charged to a potential of 1 V, kept at this voltage for one hour and their evolution was studied over the next hour. The same procedure was used for potentials between 1.1 and 1.6 V with increments of 0.1 V.

Figure 3.17 shows the results of self-discharge tests for the symmetric coin cells assembled using a) a Whatman membrane and b) a Celgard membrane. Both membranes behave similarly until reaching 1.3 V with a potential drop of less than 15%. When the potential is increased, the GF membrane maintains its drop below 15% up to 1.5 V and 19% at 1.6 V (Figure 3.17.a). On the other hand, at 1.4 V, the PP membrane increases its drop to 18%, up to 23% for 1.5 V and up to 33% for 1.6 V (Figure 3.17.b). This early drop in the potential for the PP membrane could be justified by its rapid degradation due to its lower thermal stability as well as lower porosity and ionic conductivity [91].

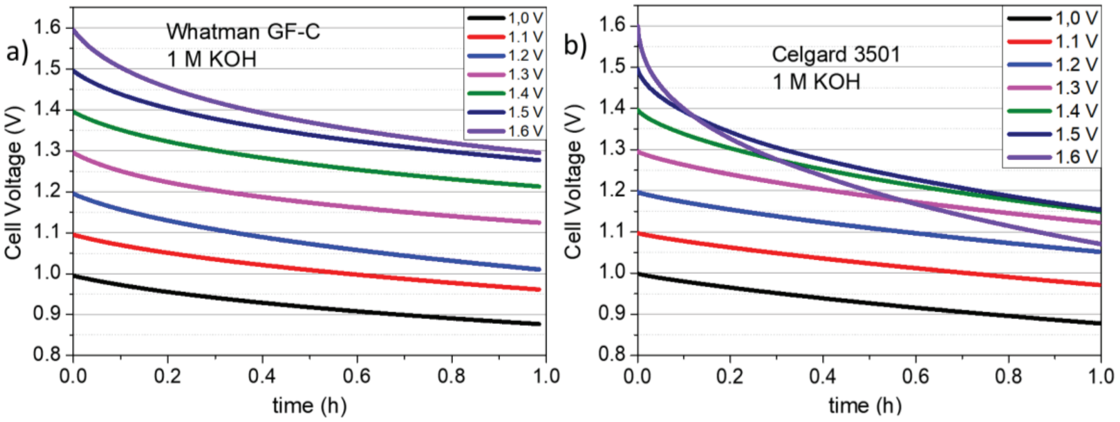

Figure 3.17. Self-discharge after a 1-hour voltage hold for a) Whatman GF/C and b) Celgard 3501 membranes.

For a better visualization of the behaviour of both membranes, the voltage drop after one hour of rest is represented in Figure 3.18. The potential drop of the PP membrane experiences a strong increase from 1.4 V, while this does not happen for the GF membrane until it reaches 1.6 V, which makes the GF membrane more suitable for working at higher potentials.

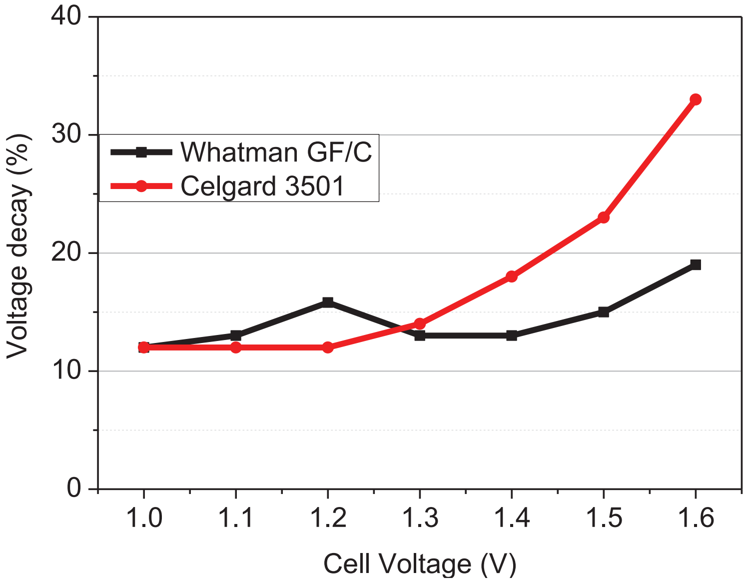

Figure 3.18. Voltage decay after one hour hold test.

In this section, we studied the system self-discharge for different voltages as a function of membrane type. Maintaining the potential for a prolonged time allows for an accelerated degradation in the cell's performance. Self-discharge studies demonstrate that the GF membranes allow the symmetric supercapacitors to work at higher potentials than PP membranes. Operating at higher potentials results in increased energy storage and highlights the critical importance of selecting appropriate materials in electrochemical experiments.

3.7 Conclusions

In this chapter, we have treated the improvement of supercapacitor components using self-standing electrodes. In the first part, we studied the effect of the mass balance between the positive and negative electrodes. We observed improved energy efficiency and impedance response when the positive electrode was larger than the negative one, with a mass ratio m_+/m_- of 0.6. In the second part, we examined the impact of thermal treatment on the electrodes with a temperature range from 110 ºC to 300 ºC, conducting electrochemical characterization through high-rate cyclic voltammetry and impedance, along with material characterization, especially using XPS. As the temperature increased, XPS analysis revealed a reduction in water content and hydroxyl groups in the O1s spectrum, along with the disappearance of oxygen functionalities and a decrease in CF2 groups. Although the C1s spectrum remained unchanged up to 250 ºC, the appearance of oxygen functional groups in the sample treated at 300 ºC, combined with electrochemical results, confirmed that 240 ºC was the optimal treatment temperature. In the third part, we studied the behaviour of two commercial membranes, Whatman GF/C glass fibre (GF) and Celgard 3501 polypropylene (PP) membrane, for the symmetric supercapacitors. We have shown how the GF membrane performs better than the PP membrane in all studied fields by carrying out high-rate cyclic voltammetry, impedance, and long-cycle galvanostatic charge-discharge. In the last part we performed hold test experiments for the GF and the PP membrane. Hold test allow accelerated degradation of the cells as the potential window is increased. The tests allowed us to verify how the GF membrane can be cycled at a higher potential than the PP membrane which leads to an increase in the stored energy.

The optimization of the components of a supercapacitor should be considered holistically, considering all the possible interactions between the parts that make it up. In this chapter we have focused on improving the components of a supercapacitor by keeping the electrolyte constant, and although most of the optimizations adopted could be extrapolated to other devices, they should be studied in each particular case.

4 Water-in-salt electrolytes for high-voltage aqueous supercapacitors

4.1 Introduction

Supercapacitors (SCs) are energy storage devices with high power but moderate energy density. Since the energy in SCs is given by equation 1.6 (E= $\frac{1}{2}CV^2$ [28]), two strategies have been developed in parallel: increasing the capacitance and the electrochemical potential window. As the electrochemical stability window of pure water is 1.23 V, aqueous electrolytes have the problem of water decomposition, the so-called oxygen evolution reaction (OER) and hydrogen evolution reaction (HER), and their stability window does not go beyond 2 V [92].

The easiest way to avoid the drawbacks of aqueous electrolytes is to change to organic electrolytes or ionic liquids, which allows the voltage window to be extended to even up to 3.6 V [93] [94]. However, organic electrolytes have a series of problems associated with them, such as their low ionic conductivity, toxicity, and flammability, which have caused some accidents. They also have a high price and require expensive equipment for dehumidification and removal of atmospheric oxygen. On the other hand, an ionic liquid (IL) is a mixture of salts in a fluid state below the boiling point of water and, therefore, consists exclusively of ions. IL can be used as an electrolyte due to its high potential window. However, its large-scale implementation is limited due to its novelty, the large variety of formulations, the high cost of some and the not well-established impact on the environment, being many of them toxic and harmful.

The interest in replacing organic electrolytes with safer, cheaper, and more reliable ones has led to attempts to increase the electrochemical stability window of aqueous electrolytes. One of the most interesting strategies is to use super-concentrated aqueous electrolytes, the so-called water-in-salt (WIS) electrolytes, where the weight or the volume of salts is greater than the water that dissolves it [95].

The presence of water molecules in aqueous electrolytes can have several impacts on the electrochemical behaviour of the system that must be considered. First, water molecules can coordinate with metal ions, forming complexes affecting the electrode reaction [96]. Water molecules can interact with the ions, affecting their mobility and reactivity [97]. Water molecules can also participate in the electrochemical reactions themselves. Water can sometimes be oxidized or reduced directly, producing oxygen or hydrogen gas [96]. In other cases, water can be involved in forming reactive species that participate in the electrode reaction contributing to the insertion mechanisms [98]. Finally, water molecules can also affect the transport of ions between the electrodes. While the translation of small ions is size dependent, big polyatomic ions such as nitrates, acetates, or sulphates, due to hydrogen bonds with water, have translational and rotational diffusion [97]. This can affect the overall performance of the electrochemical cell, including its capacity, power, and cycling stability [98].

Aqueous electrolytes are generally preferred for low-temperature devices due to their high conductivity, low cost, and the possibility of decreasing the freezing point [99], while organic electrolytes are preferred for high-temperature devices due to their wide electrochemical stability window and high solubility [100]. The choice of electrolyte for a particular electrochemical device depends on the specific application requirements and performance goals.

Regarding WIS, these electrolytes are brought to their limit of solubility and thus are able to prevent water breakdown. This strategy seems to work in batteries [101] or pseudocapacitors [102] which can store a large amount of energy but are limited in their operation when they have to handle power peaks. Electrolytes based on potassium acetate (KAc) have been used in potassium-ion batteries [103]. In this work, we evaluate the influence of the concentration of potassium acetate and lithium acetate aqueous electrolytes on the expansion of the potential window, as well as its response to rapid charge and discharge for supercapacitor use and compare with another promising WIS based on lithium bis(trifluoromethane)sulfonyl imide (LiTFSI) salt.

4.2 Materials and Methods

Self-standing electrodes with YP-50F active material, super P conductive carbon and PTFE as binder were fabricated using recipes described in Chapter 2, section 2.2.1, methods 1 and 2. The films obtained were dried in a vacuum oven for 24 hours at 60 ºC and punched in the form of 8-12 mm discs with an average weight of 4-6 mg/cm^2 for electrochemical testing. Electrodes were placed in CR-2032 coin cell and separated by a GF membrane soaked with the electrolyte.

Regarding electrolyte formulation, different concentrations between 1 and 32 mol/Kg of anhydrous potassium acetate (CH_3COOK, > 99%, Alfa Aesar), lithium acetate ($C_2H_3LiO_2$, 99.95% trace metal basis, Aldrich) and bis(trifluoromethane)sulfonimide lithium salt ($CF_3SO_2NLiSO_2CF_3$, ≥ 99.0%, Aldrich) were prepared in sealed bottles under an argon atmosphere inside a glove box. Ultrapure deionized water was degassed with nitrogen and introduced in the sealed bottles with a syringe. Electrolytes were mixed under magnetic stirring until salts were completely dissolved. Different weight ratio of salt to H_2O were prepared for characterizations and electrochemical testing in this chapter. For instance, in the case of 27 m KAc and 32 m KAc electrolytes, these were prepared with 2 ml of water, each one with a final volume of 4.8 ml and 5.2 ml and a mass of salts of 5.34 g and 6.33 g, respectively (Figure 4.1). The electrolytes did not suffer obvious signs of deterioration, remaining transparent and without signs of precipitation, for samples stored > 1 month.

Figure 4.1. Potassium acetate WIS electrolyte.

4.3 Results and discussion

4.3.1 Electrolyte characterization

Dilute aqueous electrolytes are characterized by having all the solute molecules dissociated into their ions (cations and anions). These ions are completely surrounded by water molecules (solvent) in the so-called solvation sphere, which depends on the charge and size of the ion. When the concentration of the electrolyte increases, the ratio of water molecules per ion is reduced and the solvation spheres may overlap and not completely cover the ions, which could lead to interactions between the different ions (Figure 4.2).

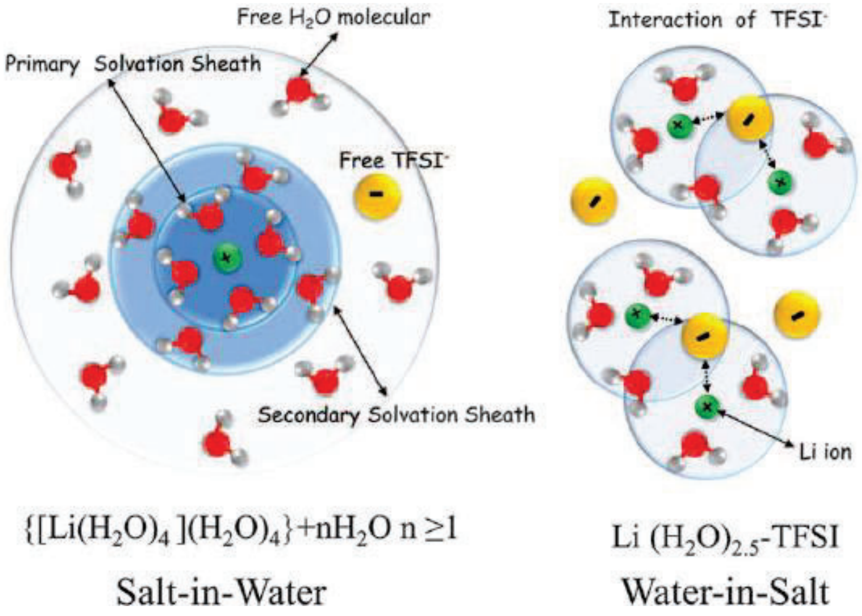

Figure 4.2. Solvation sheath of diluted and WIS electrolytes [95].

The ionic conductivity and the viscosity of selected combinations of electrolytes potassium acetate (KAc) and lithium acetate (LiAc), alone or mixed, were measured for concentrations between 1 and 40 mol/Kg (Table 4.1). Measurements show a gradual decrease in ionic conductivity when electrolyte formulation of KAc changes from dilute to highly concentrated electrolytes. On the other hand, the viscosity suffers the opposite effect, it increases as the electrolyte concentration increases. The electrolyte mixture of KAc and LiAc greatly increases the viscosity while reducing the conductivity.

Table 4.1. Electrolyte conductivity and viscosity.

Electrolyte concentration	**Weight ratio salt to H_2O**	**Molar ratio salt to H_2O**	**Viscosity (cp)**	**Conductivity (mS/cm)**
1 m Kac	0.1:1	1:55.6	1.2	68.1
1 m LiAc	0.07:1	1:55.6	1.3	35.5
21 m Kac	2.08:1	1:2.6	15.2	46.4
21 m LiTFSI	6.02:1	1:2.6	36.2	8.21
25 m Kac	2.47:1	1:2.2	26.5	34.8
27 m Kac	2.67:1	1:2.1	31.1	32.2
30 m Kac	2.97:1	1:1.9	38.6	26.1
32 m KAc	3.14:1	1:1.74	45.5	23
27 m Kac + 6 m Li Ac	3.05:1	1:1.68	105.3	11.9
32 m Kac + 8 m Li Ac	3.69:1	1:1.4	182.7	7.9

The Walden plot represents the inverse of the logarithm of viscosity vs the logarithm of molar conductivity (Figure 4.3.a) and it follows a straight line for the different electrolyte concentrations formulated using KAc and LiAc. The electrolytes with the highest conductivity are 1 m KAc and 1 m LiAc which decreases for the saturated compositions. Additionally, the viscosity of these electrolytes is independent of the shear rate, as shown in Figure 4.3.b for 27 m KAc and other super-concentrated electrolytes, indicating that electrolytes are Newtonian fluids. For the electrolyte 21 m LiTFSI, it has a conductivity of 8.21 mScm^{-1} and viscosity of 36.2 mPa at 25°C [95], deviating slightly from the trend of the other electrolytes due to a higher viscosity and mainly to a lower ionic conductivity, indicating the importance of the nature of the ions and their molecular size [104].

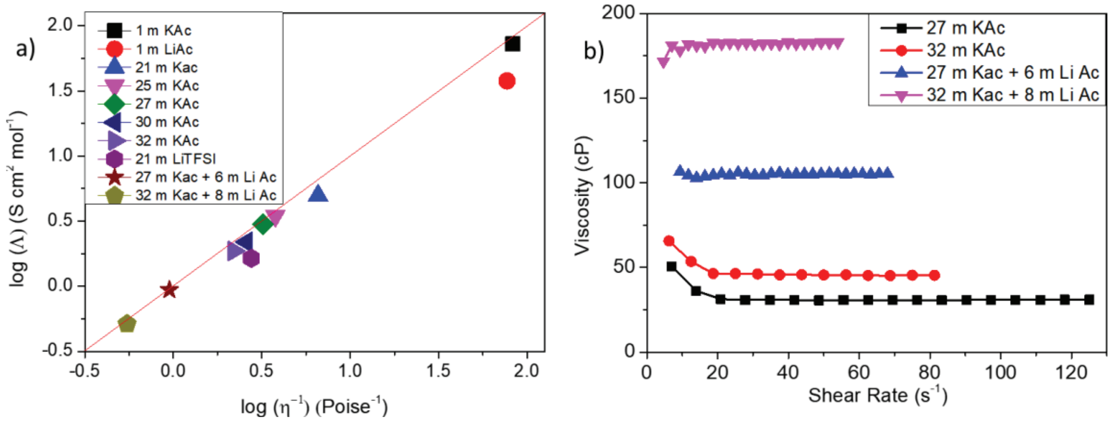

Figure 4.3. a) Walden plot representation of molar conductivity vs viscosity. b) Viscosity vs shear rate of selected electrolytes.

The electrochemical stability window of aqueous electrolytes is determined by the decomposition of the electrolyte in the electrode surface and the oxygen and hydrogen evolution reactions (OER and HER, respectively) [105]. A three-electrode Swagelok T-cell was used to study the electrochemical stability window of super-concentrated 27 m KAc, 27 m KAc + 6 m LiAc and 32 m KAc + 8 m LiAc WIS electrolytes, and compared with 1 m KAc aqueous electrolyte using cyclic voltammetry (CV) with a scan rate of 0.2 mV/s. Glassy carbon was used as working electrode, oversized YP50 as a counter electrode and Ag wire as pseudo-reference electrode. As shown in Figure 4.4, for WIS electrolytes, hydrogen evolution reaction (HER) was shifted to the left and the negative potential was expanded from -1.7 V to -1.9 V, respect to 1 m KAc. Positive potential was checked even until 2.5 V. In a 1 m KAc solution, acetate decomposition and oxygen evolution reaction (OER) began at 1.1 V, with an anodic current peak of 0.09 mA observed at 1.6 V. Although the behaviour is improved in WIS, a small anodic oxidation current persists, with a peak of 0.0043 mA at 1.46 V for 27 m KAc and less than 0.001 mA for the more concentrated electrolytes, which can be attributed to the passivation of the surface of the current collector due to anodic oxidation [101].

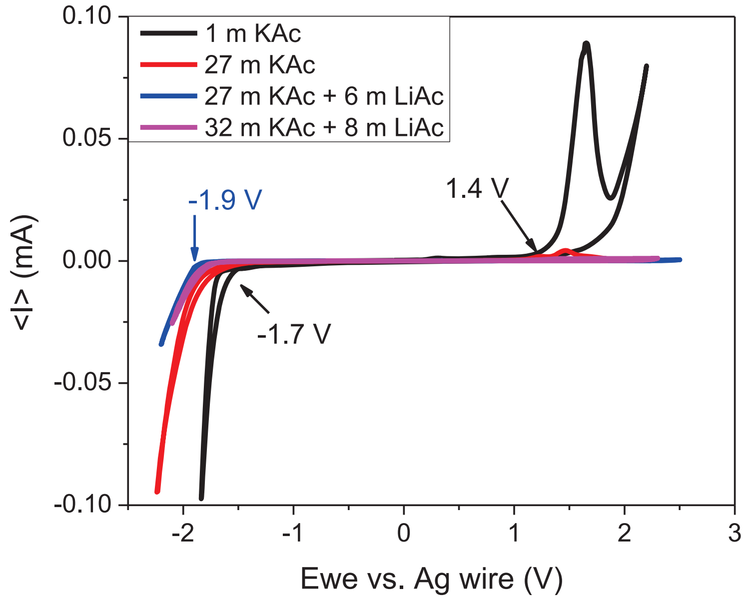

Figure 4.4. Electrochemical stability window of different aqueous electrolytes.

4.3.2 Electrochemical characterization of WIS electrolytes

Coin cells prepared with different potassium acetate (KAc) electrolytes with concentrations from 1 to 32 moles per Kg were tested in two-electrode symmetrical cells. Cyclic voltammetry (CV), galvanostatic charge-discharge, and electrochemical impedance spectroscopy (EIS) experiments were used to evaluate electrolyte performance as a function of salt concentration, operating voltage window, and cycling ageing.

First, the cells were activated by cyclic voltammetry at a low rate of 5 mV/s. Cycling begins with a potential window of 0.5 V and is repeated ten times, and then the process is repeated with potential increments of 0.1 V until the desired potential is reached.

Impedance experiments in potentiostatic mode were performed before and after activation. Figure 4.5 shows Nyquist plots for the cells assembled with KAc electrolytes, from 1 m to 32 m. The plots show typical capacitive behaviour with an almost vertical tail (straight line) at low frequencies, a short 45 degrees line at mid frequencies, and an almost ideal semicircle at high frequencies. Table 4.2 summarizes the resistance results associated with the equivalent series resistance (ESR) and charge transfer resistance (CTR) before and after activation. The values are very low, and they reduce significantly after activating the cells, probably due to better access of the ions to the interior of the pores.

Before activation, it seems that there is a trend that relates the increase in ESR and CTR to the increase in concentration (Figure 4.5.a). However, this trend is lost after activation since all values are reduced without any trend, and no relationship can be observed with the increase in concentration (Figure 4.5.b).

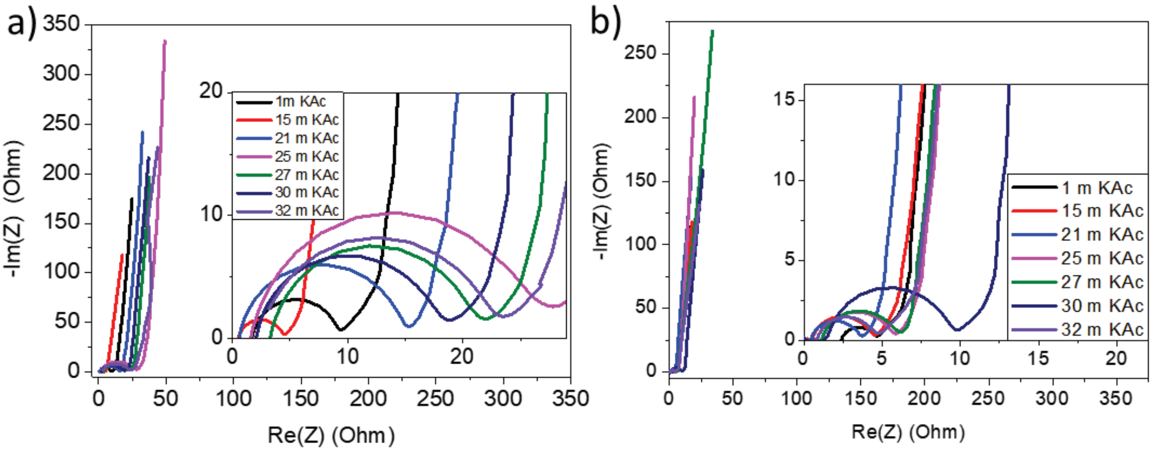

Figure 4.5. Impedance plots of symmetric supercapacitors using super-concentrated electrolytes, a) Before activation, b) After activation.

Table 4.2. ESR and CTR for different concentration of potassium acetate electrolytes.

		Non activated			**Activated**	
Electrolyte		**ESR**	**CTR**		**ESR**	**CTR**
1 m KAc		1.6	7.8		2.4	2.3
15 m KAc		0.5	4		0.5	4
21 m KAc		0.6	14.6		0.5	3.2
25 m KAc		1.6	26.2		1.1	4.8
27 m KAc		3.3	18.5		1.1	5.1
30 m KAc		2.1	16.6		1.3	8.5
32 m KAc		1.6	21.8		0.7	4

The impedance data were fitted according to the modified Randles model where a constant phase element (CPE) replaces the capacitor (Figure 4.6) transforming the RC circuit into a depressed or non-ideal semicircle. The change of the capacitance by the CPE is usually justified by the surface roughness of the electrode [106]. R1 represents the electrolyte resistance. The solution of a particle's one-dimensional diffusion equation is given by the finite-length Warburg element (W1 open). It appears as a 45º line after the R2 element, ending in an open circuit with a vertical tail like capacitor behaviour.

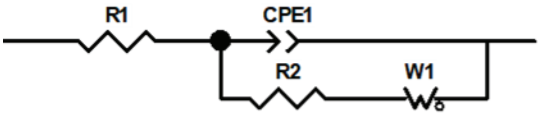

Figure 4.6. Modified Randles circuit for impedance modelling.

Figure 4.7 This shows the impedance data plotted using different impedance formalisms, including Z'' vs Z', Z' vs freq., and theta vs frequency, and the impedance fit of 32 m KAc before and after cell activation. The fit to impedance data is good since fitted data (green trace) and experimental data (blue trace) show good agreement in three different formalisms.

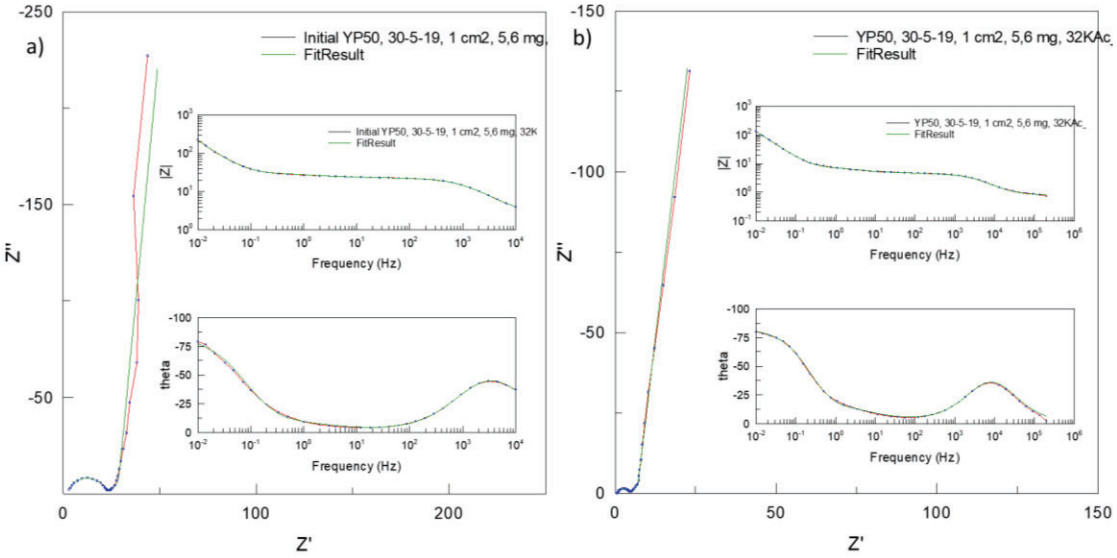

Figure 4.7. Impedance and fit of 32 m KAc a) fresh cell b) after activation. The blue trace corresponds to experimental data, and the green one is fitted.

Table 4.3 shows the data of impedance fit before and after activation of the 32 m KAc cell. We can see a high reduction in the resistances R1, R2 and W1-R (impedance term in Warburg element) for the samples after activation. If the value of CPE1-P = 1, CPE can be substituted by a capacitor C, in our case is 0.87 representing a depressed semicircle, with its value practically unchanged with cycling. CPE1-T multiplied by half the value of the CTR, (R2-R1)/2, gives the value of the time constant τ (at which the maximum height of the semicircle is reached) the same as the RC product would do in a circuit with a resistor in parallel with a capacitor. By calculating the inverse of τ, we find the frequency at which this height is reached. The W1-P parameter is 0.47, representing the near 45º slope after the semicircle. Diffusion of species is given by W1-T = L^2 / D, with L the effective diffusion thickness and D the effective diffusion coefficient of the particle; as the thickness of the cell remains constant, we suppose that the diffusion coefficient is increased with activation, resulting in a smaller value of W1-T.

Table 4.3. Impedance fit parameters of 32 m KAC of the fresh cell and after activation.

	R1	CPE1-T	CPE1-P	R2	W1-R	W1-T	W1-P
Initial	2.404	2.45E-05	0.874	19.83	18.04	1.188	0.47
Activated	0.804	5.33E-05	0.866	3.611	7.178	0.676	0.462

Cyclic voltammetry tests for 1 m KAc and 27 m KAc as a function of operational voltage are shown in Figure 4.8. For each electrolyte, voltage was increased systematically up to 1.9 V for 1m KAc and 27 m KAc. The oxygen evolution reaction (OER) appears clearly at 1.6 V for 1 m

KAc, showing great intensity as the potential increases, while it appears later and with less intensity for 27 m KAc. At the same time, capacitance increases as the potential window increases, pointing to pseudocapacitive contributions from oxygen functional groups [107], easily observed in the distorted shape down of the left side of plots, which departs slightly from the ideal rectangular shape of supercapacitors.

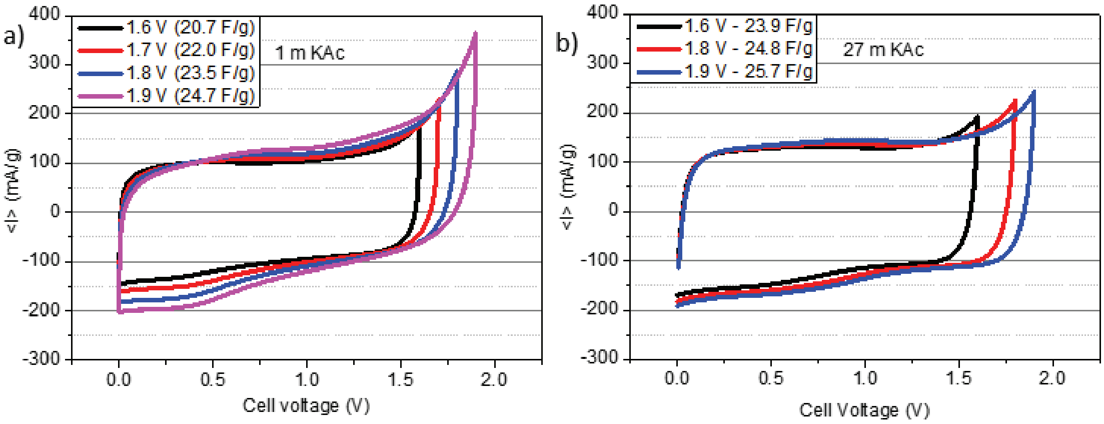

Figure 4.8. CVs at a scan rate of 5 mV/s since 1.9 V for a) 1 m KAc and b) 27 m KAc.

Coulombic efficiencies as a function of the potential window up to 2V were calculated for concentrations from 1 to 32 moles per kilogram of KAc, and results are presented in Figure 4.9. The values were obtained from CVs measured at a scan rate of 5 mV/s. Coulombic efficiencies are higher than 95 % until 1.6 V for 1, 15 and 21 m KAc, until 1.7 V for 25 m KAc, until 1.8 V for 30 and 32 m KAc, and 2 V for 27 m KAc.

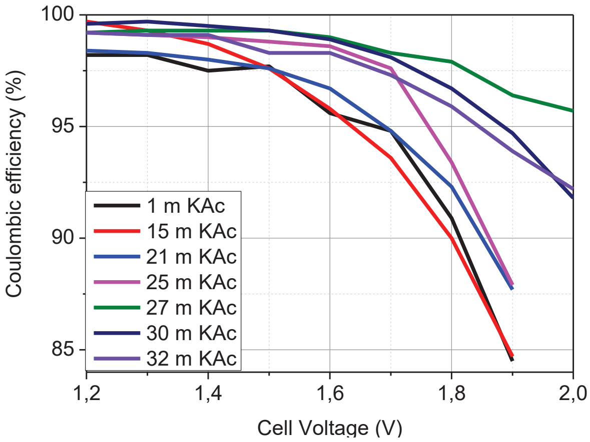

Figure 4.9. Coulombic efficiency of different potassium acetate electrolytes as a function of the potential window.

The operational voltage of 1.8 V was selected for further coin cell tests using 1 and 27 m KAc electrolytes. Cyclic voltammetry at different scan rates from 5 to 100 mV/s are presented in Figure 4.10. Both electrolytes deliver lower capacitance at higher scan rates, from 23.2 to 15.6 F/g for the 1 m KAc and from 26.3 to 19.6 F/g for the 27 KAc, corresponding to a capacitance retention of 67.2% and 74.5% respectively (Figure 4.10).

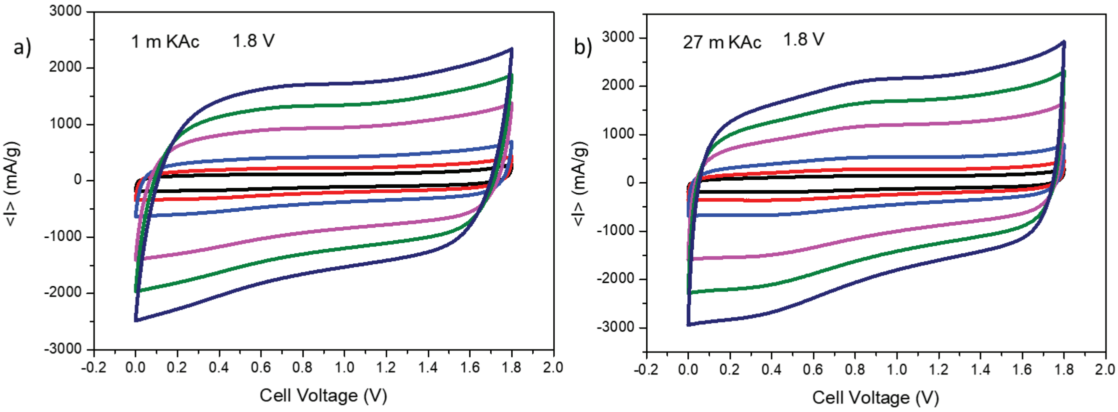

Figure 4.10. CVs at 1.8 V from 5 mV/s to 100 mV/s for a) 1 m KAc and b) 27 m KAc.

High-rate CVs between 5 and 100 mV/s in a voltage window of 1.8 V were also performed for all electrolytes, and results are presented in Figure 4.11. Results show that 27 m KAc obtains the best rate capability with a capacitance retention of 74.5%. A clear trend could not be observed for the less concentrated electrolytes, where the retained capacitance was between 63% and 71%. Still, a significant decrease could be observed for the more concentrated ones of 30 and 32 m with a retained capacitance of around 59%, probably due to the decrease in ionic conductivity and the increase in viscosity for these highly concentrated electrolytes (Table 4.1 and Figure 4.3).

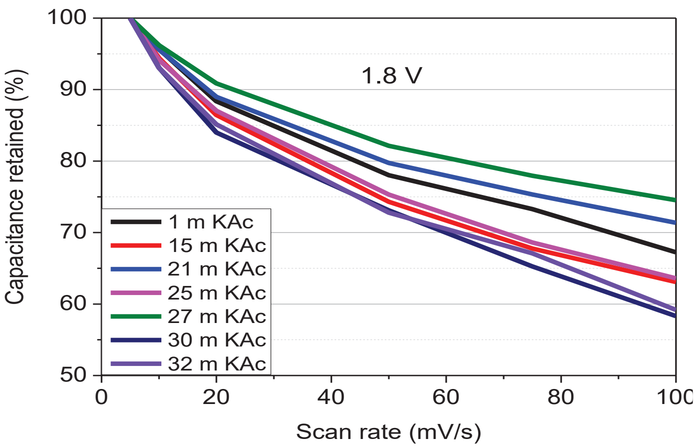

Figure 4.11. Capacitance retained with scan rates from 5 mV/s to 100 mV/s in 1.8 V voltage window.

Long-term experiments were performed with all electrolytes; the results are presented in Figure 4.12. A series of 10,000 CVs with a scan rate of 20 mV/s were launched in several potential windows between 1.7 and 1.8 V, except for 1 m KAc since it failed at 1.7 V after about 5,300 cycles and for 21 m KAc since it had erratic behaviour at 1.8 V and stopped working at 6995 cycles. Long-term cycling results for the evaluated electrolytes show that the retained capacitance after 10,000 cycles at 1.7 V is 90% for 25 m KAc, 85% for 30 m KAc and 79% for 21 m KAc. After 10,000 cycles at 1.8 V, the retained capacitance is around 55% for 25 m KAc and 30 m KAc, 62% for 27 m KAc and 65% and 32 m KAc.

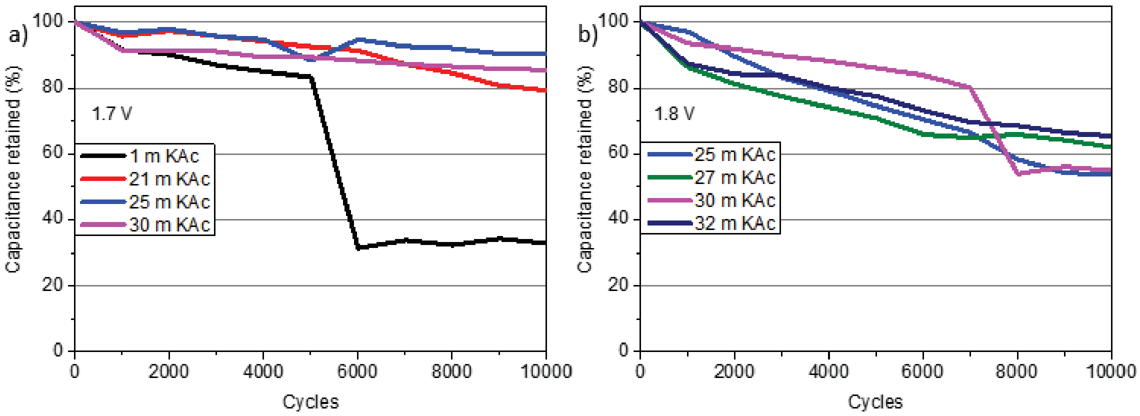

Figure 4.12. Capacitance retained after 10,000 CVs at 20 mV/s with voltages of 1.7 and 1.8 V.

To improve the electrode preparation process, magnetic stirring was replaced by ball milling, following method 2-a as described in Chapter 2, Section 2.2.1. The self-standing electrodes were tested with super-concentrated electrolytes based on potassium acetate. Long-term experiments were carried out with 10,000 galvanostatic charge-discharge cycles with a constant current of 1 A/g with a potential window of 1.8 V. In Figure 4.13.a, the capacitance values for the tested electrolytes are stable throughout the cycling, delivering 9 F/g for 10 m, around 13 F/g for 27 m and 14.7 F/g for 32 m KAC with coulombic efficiencies greater than 97% and energy efficiencies greater than 60% for 10 and 27 m KAc and 70% for 32 m KAc (Figure 4.13.b).

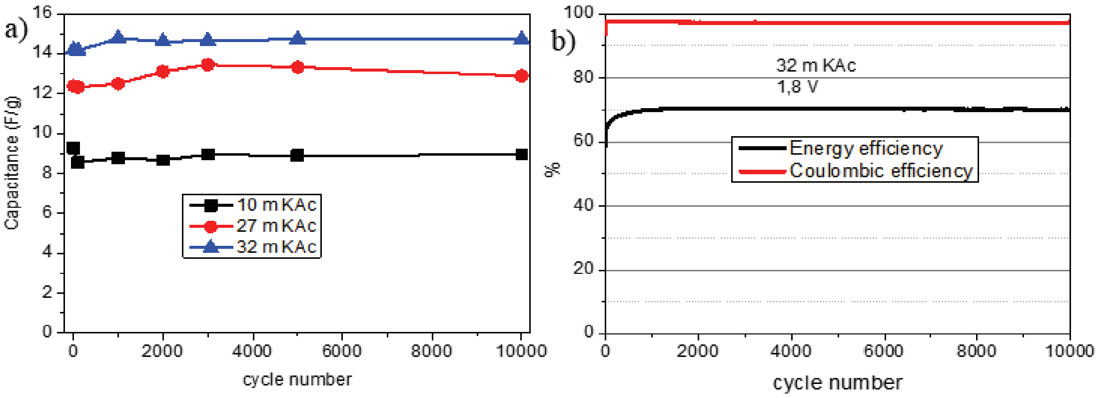

Figure 4.13. 10,000 CVs at 1 A/g in 1,8 V. a) Capacitance for 10 m, 27 m, and 32 m Kac. b) Energy and coulombic efficiencies for 32 m KAc.

High-rate galvanostatic charge-discharge tests were conducted for the 1 m KAc aqueous electrolyte and the 27 m and 32 m KAc WIS electrolytes to assess their power-energy performance, which is illustrated in the Ragone plot (Figure 4.14). The 27 m KAc WIS electrolyte demonstrates the best performance, maintaining high energy even at high rates. These results are comparable to, or even surpass, the performance of commercial capacitors using organic electrolytes, as reflected in technical datasheets [62], [108].

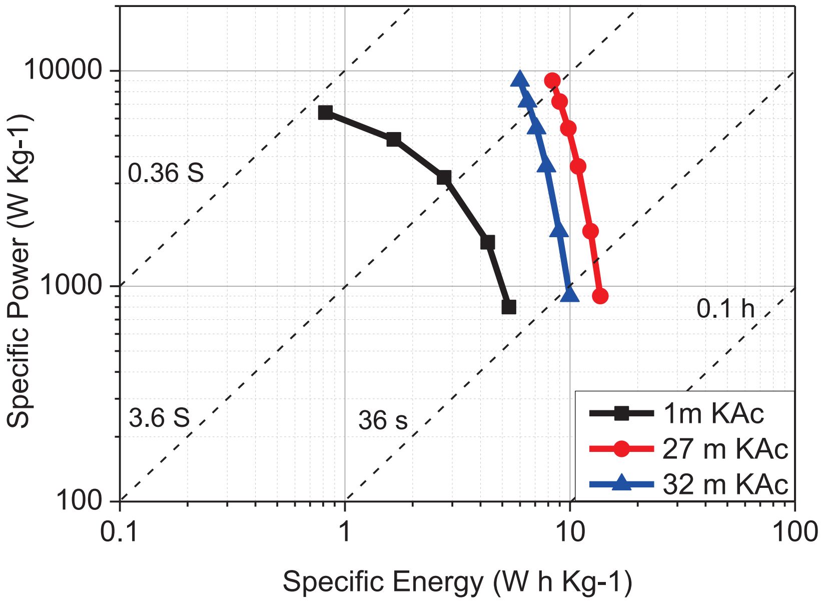

Figure 4.14. Ragone plot of aqueous and WIS electrolytes.

Self-standing electrodes prepared using the ball milling technique demonstrate better capacitance retention during long-term cycling compared to those prepared with magnetic stirring. After 10,000 cycles of galvanostatic charge-discharge at 1 A/g, the capacitance retention remained at 100% for all three selected electrolytes: 10 m, 27 m, and 32 m KAc. High-rate cyclic voltammetry shows 74.5% capacitance retention for 27 m KAc when the scan rate increases from 5 to 100 mV/s, compared to 59% for 32 m KAc, with other concentrations falling between these values. High-rate galvanostatic charge-discharge tests reveal that the 27 m KAc electrolyte delivers the best power-to-energy performance, as shown in the Ragone plot, outperforming even commercial capacitors. This makes 27 m KAc the optimal choice for a super-concentrated electrolyte.

4.3.3 Mixed electrolyte strategy to improve the voltage window

We add a second salt to potassium acetate to reduce the number of water molecules per ion (Table 4.1). Lithium acetate was chosen because lithium is the lightest and the smallest alkaline element of group I. So, two different concentrations of potassium acetate (KAc) with formula CH_3CO_2K and molecular weight 98.15 and lithium acetate (LiAc) with formula $C_2H_3LiO_2$ and molecular weight 65.99 were tested, these being 27 m KAc + 6 m Li Ac and 32 m KAc + 8 m LiAc, the first having better conductivity and viscosity than the second. Alkaline electrolytes were compared to the super-concentrated WIS electrolyte 21 m Lithium bis(trifluoromethane)sulfonyl imide (LiTFSI) with formula $CF_3SO_2NLiSO_2CF_3$ and molecular weight 287.09, and results are presented in this section. We found in the literature that the 40.4 m KAc + 9.8 m LiAc electrolyte can reach an operating window of 2 V in hybrid capacitor [109] and the 31.3 m LiTFSI electrolyte can reach up to 2.4 V in AC capacitor [110].

Three symmetrical self-standing capacitors were made, following method 1 as described in Chapter 2, Section 2.2.1, with activated carbon electrodes separated by a GF membrane soaked with the three electrolytes that we are going to study: 27 m KAc + 6 m LiAc, 32 m KAc + 8 m LiAc and 21 m LiTFSI. After electrochemical activation, high-rate studies were carried out using CVs between 5 mV/s and 100 mV/s in a potential window of 2 V.

In Figure 4.15.a-c, the high-rate cyclic voltammograms (CVs) for the 21 m LiTFSI electrolyte maintain the ideal square shape characteristic of capacitors. However, the CV for 27 m KAc + 6 m LiAc shows a slight deviation from this ideal shape, while the CV for 32 m KAc + 8 m LiAc is notably distorted. This distortion is attributed to the poor ionic conductivity and high viscosity of the electrolyte, as shown in (Table 4.1). At a low scan rate of 5 mV/s, the alkaline electrolytes 27 m KAc + 6 m LiAc and 32 m KAc + 8 m LiAc deliver capacitances of 30.7 F/g and 29.5 F/g, respectively, which are significantly higher than the 18 F/g achieved with 21 m LiTFSI. At a higher scan rate of 100 mV/s, the capacitances drop to 20.8 F/g, 13.5 F/g, and 11.3 F/g for the three electrolytes, with retained capacitances of 68%, 43%, and 63%, respectively (Figure 4.15.d).

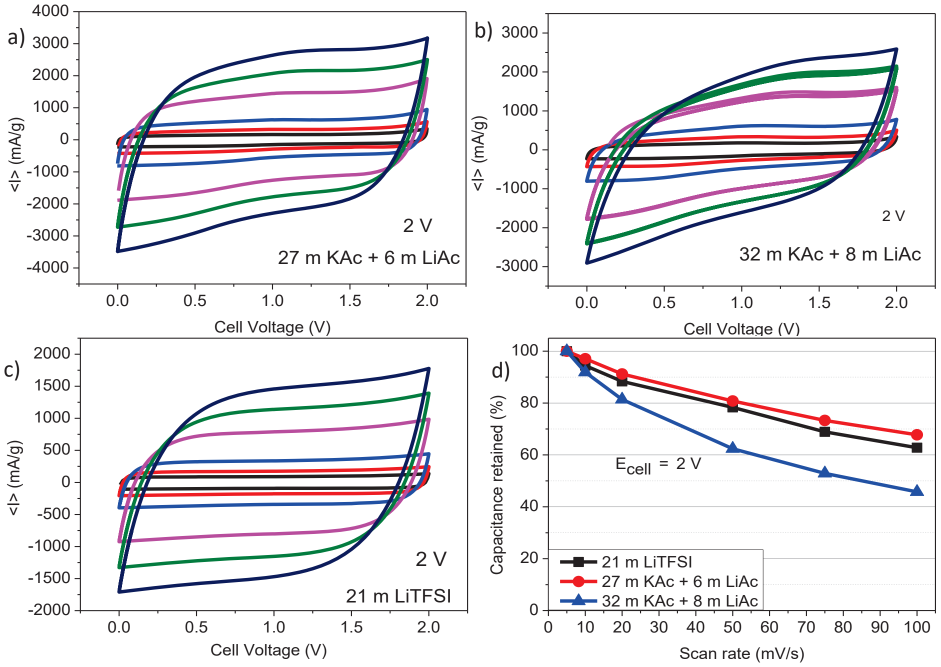

Figure 4.15. CVs between 5-100 mV/s for 27 m KAc + 6 m LiAc a), 32 m KAc + 8 m LiAc b) and 21 m LiTFSI c). d) Retained capacitance with increasing rate.

Due to the good high-rate behaviour of 27 m KAc + 6 m LiAc and 21 m LiTFSI, we conducted long cycling experiments at 20 mV/s in a potential window of 2 V, and the results are presented in Figure 4.16.

The 27 m KAc + 6 m LiAc electrolyte begins with a high initial capacitance of 28.7 F/g, retaining 86% after the first 500 cycles. By 1,000 cycles, the retention drops to 43%, and further declines to 22% at 10,000 cycles (Figure 4.16.a). In contrast, the 21 m LiTFSI electrolyte starts with a moderate initial capacitance of 16 F/g and retains 94% of its capacitance after 10,000 cycles (Figure 4.16.b).

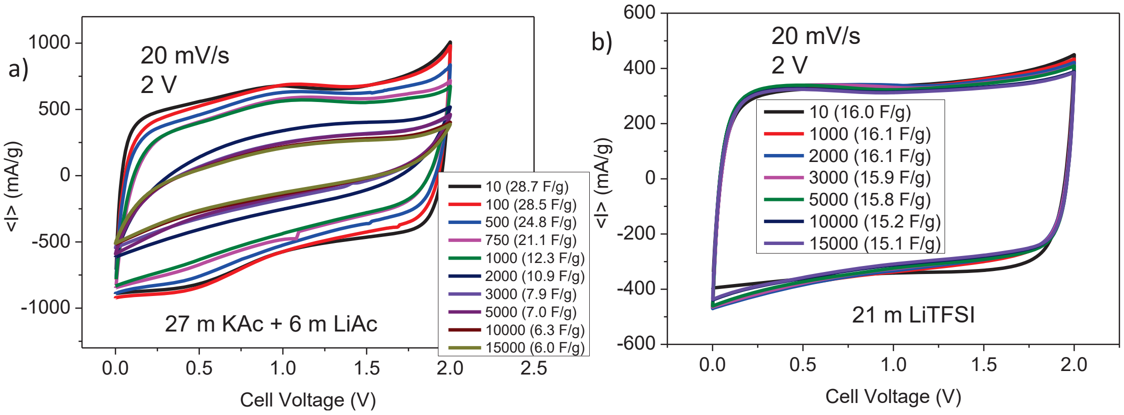

Figure 4.16. 15,000 CVs at 20 mV/s in 2 V voltage window for 27 m Kac + 6 m LiAc a) and 21 m LiTFSI b).

Considering the good results of LiTFSI electrolyte shown in Figure 4.16.b, the potential window was widened, and long-term experiments were carried out with series of 10,000 CVs for 2.1, 2.2 and 2.3 V. The good behaviour of the electrolyte at these potentials is reflected in retained capacitances of 97, 83 and 74 % respectively (Figure 4.17).

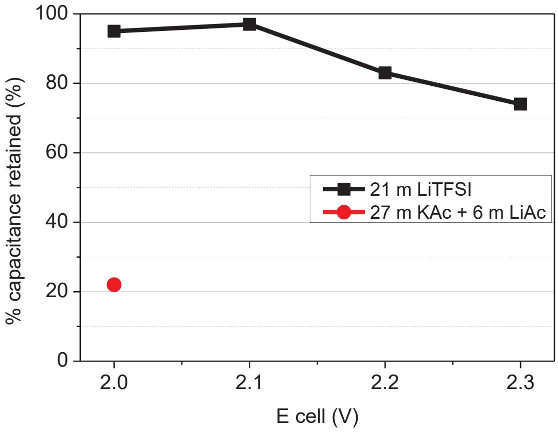

Figure 4.17. Capacitance retained after 10,000 CVs at 20 mV/s.

Finally, we present the estimated cost of the electrolyte to fabricate 1 cell and compare them with the commercial organic electrolyte 1 M $LiPF_6$ EC/DEC, used in research in batteries and supercapacitors [64], [111]. All prices were taken from www.sigmaaldrich.com. First, we calculated the price per gram of each salt, and then we obtained the molarities of the electrolytes used, being 10.7 M for 27 m KAc, 12.7 M for 27 m KAc + 6 m LiAc and 5 M for 21 m LiTFSI, which multiplied by their molar masses gave us the grams of salt per litre. By multiplying the grams of salt by its price, we calculate the cost per litre of each electrolyte. To know the final price, it was considered that 60 µl of electrolyte is needed per cell (Table 4.4). The calculated cost of electrolytes used varies significantly, ranging from €0.0044 for 27 m KAc and €0.0069 for 27 m KAc + 6 m LiAc, to €0.0588 for the organic electrolyte 1 M $LiPF_6$ in EC/DEC, and €0.3307 for 21 m LiTFSI (Table 4.4). The electrolytes based on KAc and LiAc are the cheapest, the organic one has an intermediate price, and the one based on LiTFSI is the most expensive. Although the LiTFSI electrolyte has the best behaviour among the aqueous electrolytes, Figure 4.17, its practical viability is very limited due to its high cost and the possible environmental impact of imide-based electrolytes.

Table 4.4. Estimation of the cost of electrolyte used in the manufacture of 1 cell.

Electrolyte	**Cost (€/cell)**
27 m KAc	0.0044
27 m KAc + 6 m LiAc	0.0069
21 m LiTFSI	0.3307
1 M $LiPF_6$ EC/DEC	0.0588

4.4 Conclusions

In the first part, we studied salt concentration's effect in super-concentrated electrolytes on the potential window of symmetric supercapacitors. The evolution of hydrogen for the electrolyte 1 m KAc occurs at -1.7 V, while for the concentrated electrolytes 27 m KAc, 27 m KAc + 6 m Li Ac and 32 m KAc + 8 m Li Ac appeared at -1.9 V. The oxygen evolution reaction is observed at 1.4 V for 1 m KAc. For the more concentrated electrolytes, there is a small anodic oxidation current, which can be attributed to the passivation of the current collector surface due to anodic oxidation.

In the second part, the compromise between rate capability, long life, cost, and environmental considerations led us to choose the 27 m KAc electrolyte. This electrolyte can retain 74.5% of the capacitance when increasing the rate from 5 to 100 mV/s. It also maintains its initial capacitance of 13 F/g after 10,000 cycles at 1 A/g in a potential window of 1.8 V. Its estimated electrolyte cost is €4.42 to manufacture 1,000 cells.

In the third part, we explored the mixture of KAc and LiAc. The salt mixture, especially 27 m KAC + 6 m LiAc, delivers good capacitance and rate capability results at 2 V. We also used a super-concentrated electrolyte based on LiTFSI salt, seeing how the potential window is increased to 2.3 V. However, its use is limited due to its high cost and possible adverse environmental effects.

Overall, we have studied the application in supercapacitors of a new type of highly concentrated aqueous solutions, the so-called water-in-salt electrolyte, which offer a wide electrochemical stability window. This increase in the potential window entails an increase in the stored energy, as it is proportional to the square of the potential. This increase in stored energy helps bridge the gap between supercapacitors using aqueous and organic electrolytes. Aqueous electrolytes are significantly cheaper, easier to prepare and store, and offer environmental benefits, making them a more sustainable alternative.

5 Degradation of water-in-salt symmetric supercapacitors

5.1 Introduction

The inevitable degradation of energy storage devices is a phenomenon that presents challenges to the long-term effectiveness of these systems. The objective of this chapter is the comprehensive study of the degradation of symmetric supercapacitors based on activated carbon electrodes using aqueous electrolytes. The choice of the electrolytes was motivated by their different potential windows as investigated in Chapters 3 and 4, one being the standard aqueous electrolyte 1 M KOH, whose potential window is 1.6 V, and the super-concentrated 27 m KAc, whose potential window can reach 1.8 V.

The main mechanisms of degradation originate from the decomposition of the electrolyte, which leads to the formation of gases, precipitates, or degradation materials that can block the electrode pores or form a passivation layer on their surface. Oxidation of the positive carbon electrode with irreversible CO_2 production and corrosion of the positive stainless steel current collector, resulting in the formation of a passivation oxide layer [112], are the main cause of performance deterioration in symmetrical carbon capacitors with an increase in resistance [113], [114]. The irreversible reactions inside the cell lead to the release of gases that cause an increase in pressure with the formation of bubbles in the electrodes and current collectors that increase the ionic resistance, making the transport and diffusion of the ions difficult. The concentration of gases can also cause a loss of contact between the electrodes and the current collector, causing an increase in electronic resistance [115]. Additionally, the electrodes may undergo structural changes due to adding functional groups, reducing their capacitance or stability. Operating conditions such as temperature, humidity, and voltage also significantly impact performance. Furthermore, mechanical stress on the electrodes caused by a prolonged number of cycles can diminish their operability [116].

All these degradation mechanisms are thoroughly studied and analysed using the Failure Mode and Effects Analysis (FMEA) method [117]. FMEA is a tool used to identify potential failures in a product or process, classifying them by their effects, severity, and frequency. It also proposes actions to eliminate or mitigate these failures. The FMEA process begins by analysing degradation mechanisms, classifying their impact on degradation, degradation modes, and their effects on the system. This method is applied to various energy storage systems, including supercapacitors [118] and Li-ion batteries [119].

In this chapter, we have investigated the degradation mechanisms of the super-concentrated electrolyte 27 KAc through the FMEA method and compared the results to those of the standard aqueous electrolyte 1 m KAc. To our knowledge, no studies have addressed the degradation mechanisms of super-concentrated aqueous electrolytes. The studies have considered electrochemical cycling (subsection 5.3.1) of the symmetric supercapacitors at a high voltage of 2 V to accelerate ageing, and the electrodes and components dismantled afterwards for the post-mortem analysis (subsection 5.3.2), aiming to elucidate the possible causes of failure. The FMEA analysis has also involved component reassembly, and results are presented in subsection 5.3.3.

5.2 Materials and methods

Electrodes were prepared with YP50 activated carbon as active material, as explained in section 2.2.1, following the method 2-a. Electrodes were arranged in stainless steel coin cell (SS-304) or Swagelok cell with glassy carbon current collectors, see section 2.2.3, and separated by a nanoporous fibreglass membrane soaked with the electrolytes. Two different aqueous electrolytes were considered: 1) super-concentrated (water-in-salt) 27 m potassium acetate (KAc) basic electrolyte, with a pH of 9, and 2) 1 M KOH highly basic electrolyte, with a pH of 14.

5.3 Results

5.3.1 Cycling ageing

Supercapacitors store energy through the surface accumulation of charges, which barely produce changes in the volume of the electrode, causing very little damage to its components that makes the expected cycle life of supercapacitors greater than 10^6 cycles of charge and discharge [12], as long as they remain within their potential stability window and are not subjected to temperature stress [118]. To accelerate the degradation process, we have performed an electrochemical characterization of aqueous supercapacitors within a potential of 2 V, which is greater than the stability potential window of the used electrolytes.

Cells were prepared with the selected electrolytes and activated as described in Section 4.3.2. After activation, the cells were cycled from 1.3 to 2 V with a series of 10 CVs at a sweep rate of 50 mV/s, followed by long-term charge and discharge cycles at a current density of 1 A/g, between which impedance spectroscopies were interspersed. From them, efficiency, increase in impedance, long-term stability, performance decay and lifespan were studied.

CVs measured during the activation up to 2 V for 1 m KOH and 27 m KAc are presented in Figure 5.1 a) and b), respectively. In a voltage window of 2 V, a pronounced current peak corresponding to the oxygen evolution reaction is observed in the positive electrode, with increases of 184% and 94% compared to a voltage window of 1.3 V for 1 M KOH and 27 m KAc, respectively. Meanwhile, the peak corresponding to the hydrogen evolution reaction, observed in the negative electrode, increases by 53% and 85% for 1 M KOH and 27 m KAc, respectively. Both peaks indicate irreversible reactions [120], as expected due to the high potential applied.

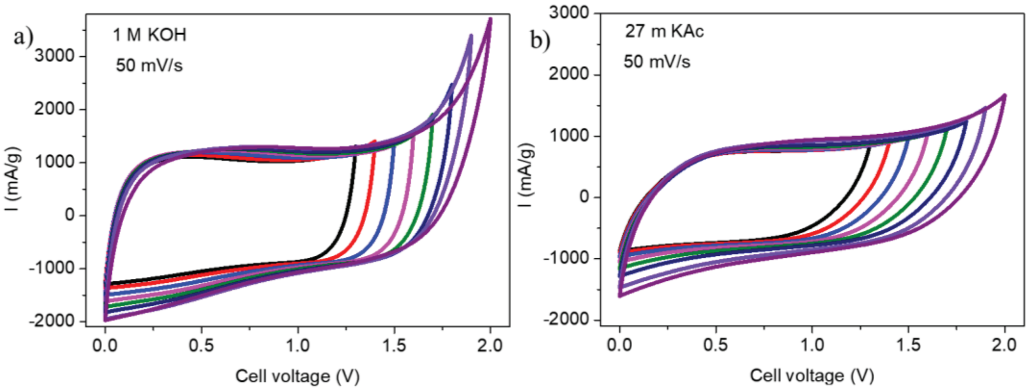

Figure 5.1. CVs measured in the voltage window 2V at 50 mV/s for AC symmetric capacitor in 1 M KOH a) and 27 m KAc b) electrolytes

Long-term galvanostatic charge-discharge at 1 A/g since 2 V were performed after CVs; results for the first cycle are presented in Figure 5.2. The almost triangular shape of the SC with 27 m KAc, Figure 5.2 b), starts to bend at 1.7 V. In contrast, the curve of 1 M KOH, Figure 5.2 a) shows a flattening at 1.7 V; this plateau-like behaviour is similar to the one observed in batteries and associated with a faradaic process. It lasted almost 8 minutes and was assigned to an irreversible oxidative process. The decomposition reactions in the electrodes are usually assigned to the oxidation of functional groups that cause the evolution of CO and CO_2, the decomposition of water in the electrolyte, with the production of O_2 and H_2 in the positive and negative electrodes respectively, and the corrosion of carbon on the positive electrode with CO and CO_2 generation [121][122]. The conductivity of the electrolyte can decrease due to a low dissociation of the salts into their ions [116] and parasitic reactions of the electrolyte lead to the formation of precipitates on the surface and inside the pores of the electrodes, which limit the access of the electrolyte ions to the active zones with the consequent reduction in performance [123].

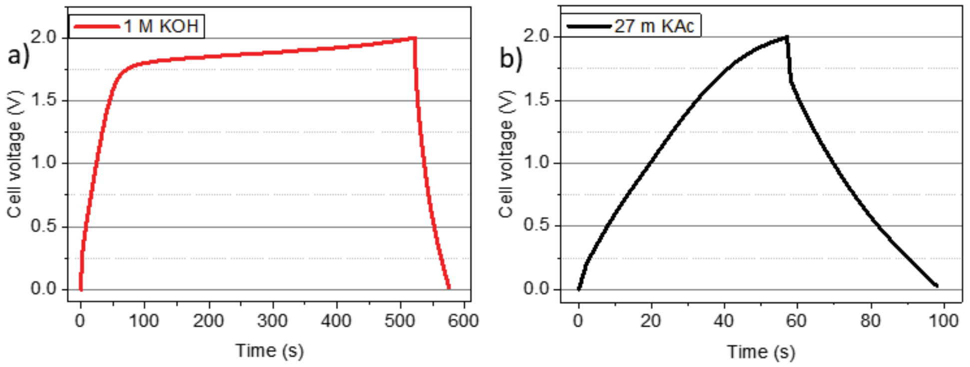

Figure 5.2. First charge-discharge cycle in the voltage window 2V for supercapacitors with a) 27 m KAc and b) 1 M KOH electrolytes.

The degradation mechanisms of aqueous capacitors occur at specific temperatures and certain cell voltages [116]. For 1 M KOH, almost all the current supplied between 1.7 and 2.0 V during the first cycle was used in an irreversible reaction, experiencing a rapid degradation process, Figure 5.2 a). The Coulombic efficiency of the first cycle was only 10% for 1 m K OH and 74% for 27 m KAc, gradually increasing during the first 100 cycles to 92 and 94%, respectively, reaching values close to 100% in the following cycles (Figure 5.5.a). Thus, it is not surprising that the 1 M KOH cell suffered a rapid degradation after the first 100 charge-discharge cycles, as can be seen in the high voltage drop, or IR drop, and the shorter discharge time (Figure 5.3.a) that entails lower capacitance (Figure 5.5.b). It should be noted that the 27 m KAc cell (Figure 5.3.b) also has an important IR drop, although less than that of 1 M KOH, and the discharge times are reduced with cycling, symptoms that the applied potential was also excessive, as we expected for a 2 V voltage window.

During the charging and discharging process, a large amount of irreversible heat is generated, causing the capacitor to heat up and deteriorate its performance [124]. The generation of irreversible heat is caused by the Joule effect, increasing energy losses through the porous structure [125].

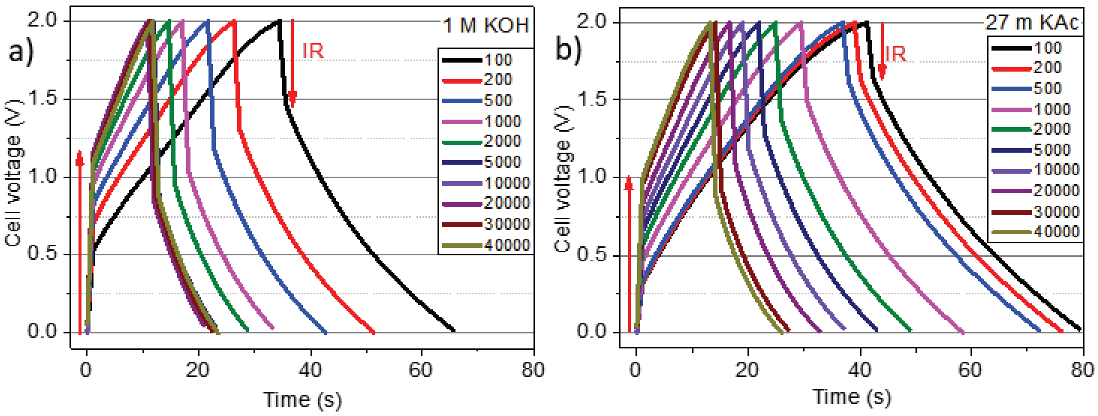

Figure 5.3. Long term galvanostatic charge-discharge cycles of SCs for 1 M KOH a) and 27 m KAc b) electrolytes.

The increase in the IR drop (in volts) for the two electrolytes as a function of cycles is shown in the Table 5.1. Data show a rapid increase in IR drop from the first galvanostatic charge-discharge cycles at 2 V for the two samples, Figure 5.3. This increase is more pronounced for samples with 1 m KOH electrolyte at the beginning of cycling. After 30,000 cycles, the IR drop equals both samples ~1.1 V. As the resistance in the IR drop is related to the heat generation rate [126], the large IR drop that appears in our devices on cycling made us think that the heat generated in the electrodes is one reason for the rapid drop in capacitance (Figure 5.5.b).

Table 5.1. IR drop (V) after 2 V galvanostatic cycling.

Cycle number	**10**	**100**	**200**	**300**	**400**	**500**	**1,000**	**2,000**	**5,000**	**10,000**	**20,000**	**30,000**	**40,000**
27 m KAc	0.35	0.35	0.36	0.37	0.37	0.38	0.51	0.62	0.72	0.81	0.93	1.08	1.13
1 M KOH	0.29	0.53	0.70	0.74	0.79	0.82	0.96	1.04	1.15	1.17	1.15	1.13	1.12

The degradation process of the cells was followed through impedances interspersed between the charge-discharge cycles. The Nyquist plots measured for the two electrolytes as a function of cycling ageing are shown in Figure 5.4, and measured CTR values are presented in Table 5.2. From initial galvanostatic cycles, black traces in Figure 5.4, the CTR shows a notable increase as a function of cycling in the case of 1 M KOH, Table 5.2. That is not the case for 27 m KAc, which shows a less pronounced increase in CTR as a function of cycling.

This higher value of the CTR for 1 m KOH is correlated to the IR drop seen in charge-discharge experiments (Figure 5.3). The changes in the impedance follow the physicochemical deterioration of the cell observed in galvanostatic charge-discharge. Cells cycled after 40,000 galvanostatic cycles exhibit a significant rise in CTR, as indicated by the increased voltage drop at the beginning of the discharge curve. The tail of the impedance also moved away from verticality, as a sign of the loss of pure capacitive behaviour.

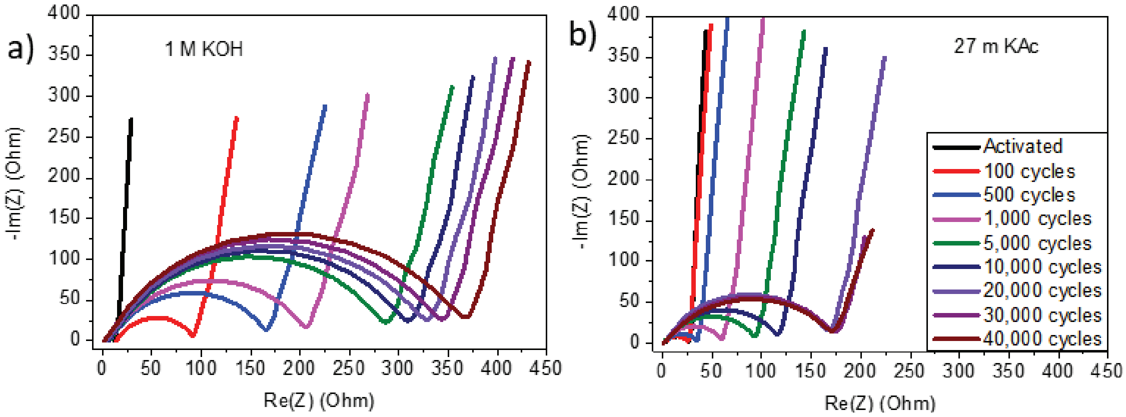

Figure 5.4. Capacitor impedance evolution with cycling of a) 1 M KOH and b) 27 m KAc electrolytes.

Table 5.2. CTR (in ohms) after CVs activation since 2 V and long-term galvanostatic charge-discharge.

CTR (Ω)	Initial	1.2 V	1.8 V	2.0 V	100	200	300	400	500	1,000	2,000	5,000	10,000	20,000	30,000	40,000
27 m KAc	141	98	49	25	24	26	27	30	33	58	74	92	115	167	174	171
1 M KOH	67	21	8	13	77	116	131	146	159	199	233	281	304	324	341	368

Energy efficiency, defined as the relationship between the energy supplied and the energy recovered, was monitored throughout the charging and discharging process (inset of Figure 5.5.a). Energy efficiency shows severe degradation during the first few hundred cycles, reaching efficiencies of 23% and 36% after 10,000 cycles for 1 M KOH and 27 m KAc, respectively (inset of Figure 5.5.a). After 10,000 cycles, the discharge capacitance was 5.5 F/g, with a 73% decay for 1 M KOH, and 9.4 F/g, with a 54% decay for 27 m KAc (Figure 5.5.b).

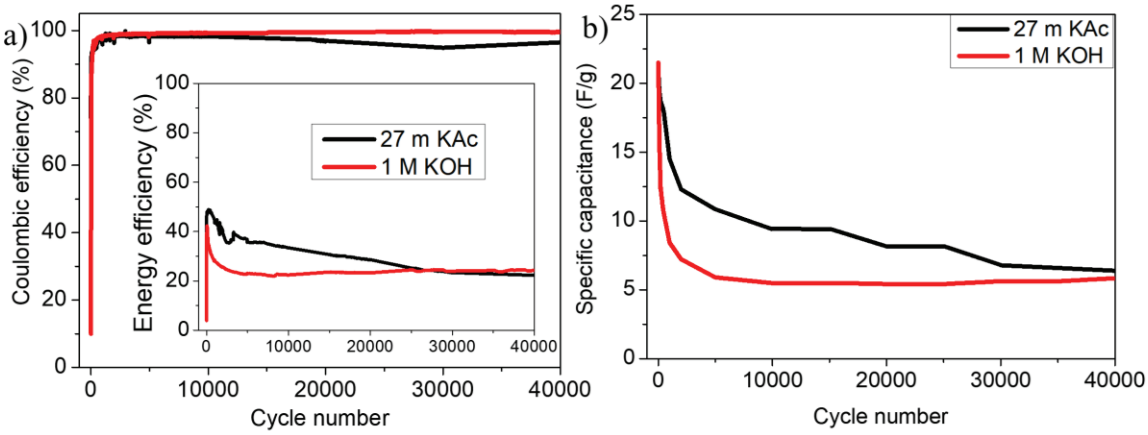

Figure 5.5. a) Coulombic efficiency energy efficiency (inset) and b) specific capacitance of 1 M KOH and 27 m KAc electrolytes measured over 40,000 cycles in a 2 V voltage window.

Among the two samples, the 1 M KOH electrolyte exhibits faster degradation. This is evidenced by a significant increase in current in the CVs at elevated potentials, related to the evolution of oxygen, a greater IR drop in the galvanostatic cycles and a higher CTR in the impedances when compared with super-concentrated 27 m KAc electrolyte. Both samples deliver a similar capacitance of ~ 6 F/g, corresponding to 30 % of the initial one, and an IR drop of 1.1 V with CTR values of 171 Ω for 27 m KAc and 368 Ω for 1 M KOH after 40,000 cycles. At this point, cells were disassembled, and components were investigated through post-mortem analysis.

5.3.2 Post-mortem analysis

Once the cells were cycled, the structural and physicochemical characterization of the electrodes was carried out. The cells were opened, and their components were separated preserving the positive and negative electrodes of the cells used with the electrolytes 1 M KOH (Figure 5.6.a) and 27 m KAc (Figure 5.6.b). The membrane of the cell containing 27 m KAc changed from white to brownish colour, possibly due to the degradation of the electrolyte, which sometimes took on a slight brownish colour in the bottle (Figure 5.6.c), although the electrolytes stored in inert conditions did not show any degradation.

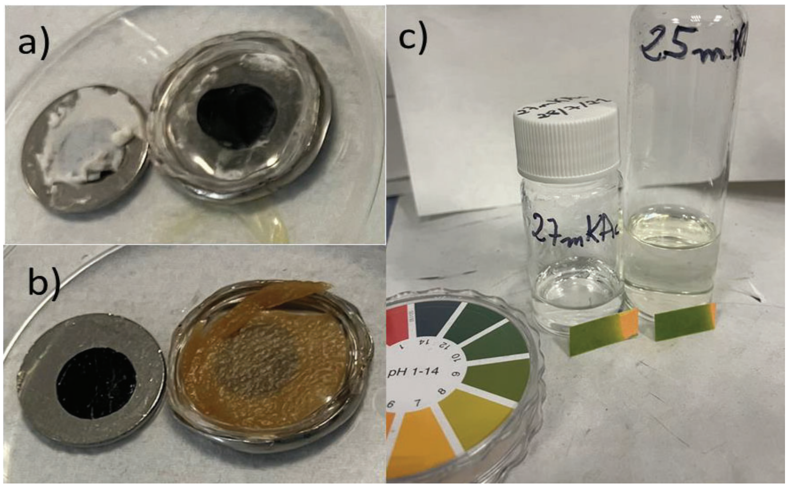

Figure 5.6. Open cells: 1 M KOH electrolyte a) and 27 m KAc electrolyte b). c) Changes in the colour and pH in potassium acetate electrolytes.

In post-mortem investigations, SEM is as an invaluable tool for unravelling the intricate details of material degradation and performance-related phenomena. The examination of morphological alterations, such as pore structure evolution, particle aggregation, and potential electrolyte-induced effects centred in the analysis of both positive and negative electrodes individually, with comparisons with their pristine counterparts, was used to decipher the interplay between activated carbon and the electrolytes in the overall performance of supercapacitor devices. SEM pictures of post-mortem electrodes are shown in Figure 5.7. All analysed samples display thick fibres from the fibreglass membrane.

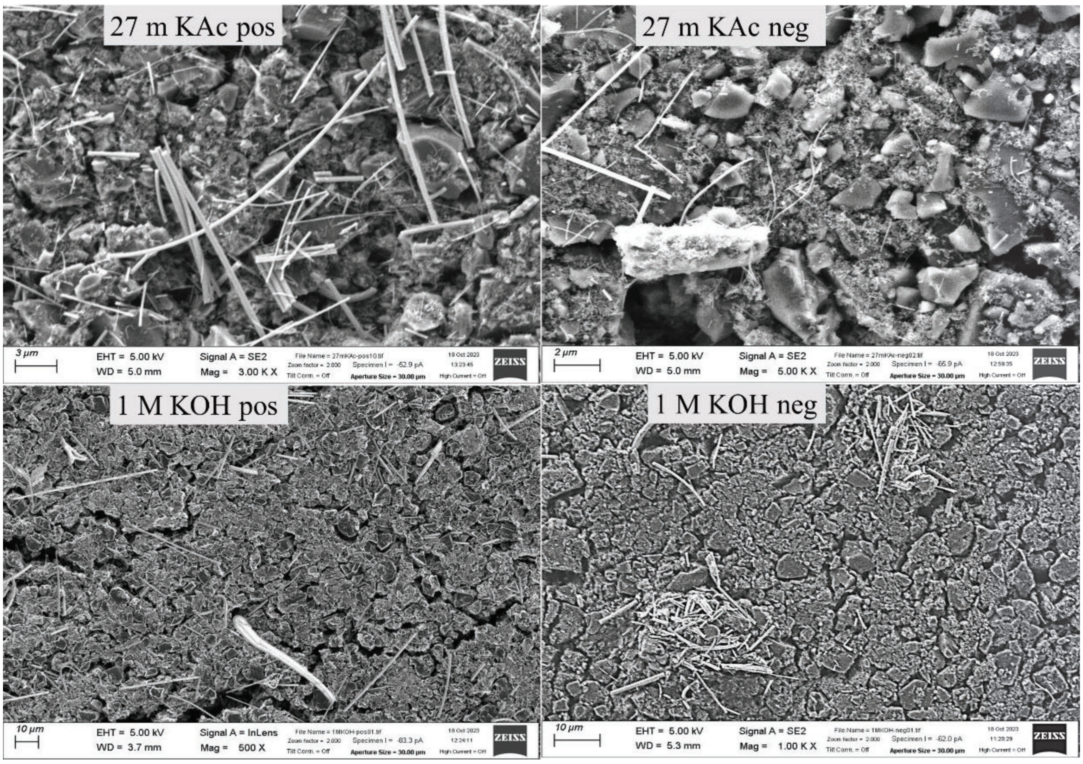

Figure 5.7. Low-magnification SEM images of post-mortem electrodes after 40,000 cycles at 2V.

Figure 5.8 and Figure 5.9 show pictures of cycled electrodes at higher magnification. For all samples analysed, particle agglomeration is not observed. No changes in the particle morphology were observed when compared to the uncycled electrodes (Chapter 2, Figure 2.14.d) , with some unblocked pores clearly visible (Figure 5.8). The images also show some precipitate on the surface of the AC particles, particularly on the negative electrode from the 1 M KOH cell. Although these precipitates could be mostly removed after a thorough washing with water, their failure in dissolving during the first wash indicates low solubility. The positive electrodes exhibit a clean appearance for both electrolytes, with visible traces of the PTFE binder (Figure 5.9).

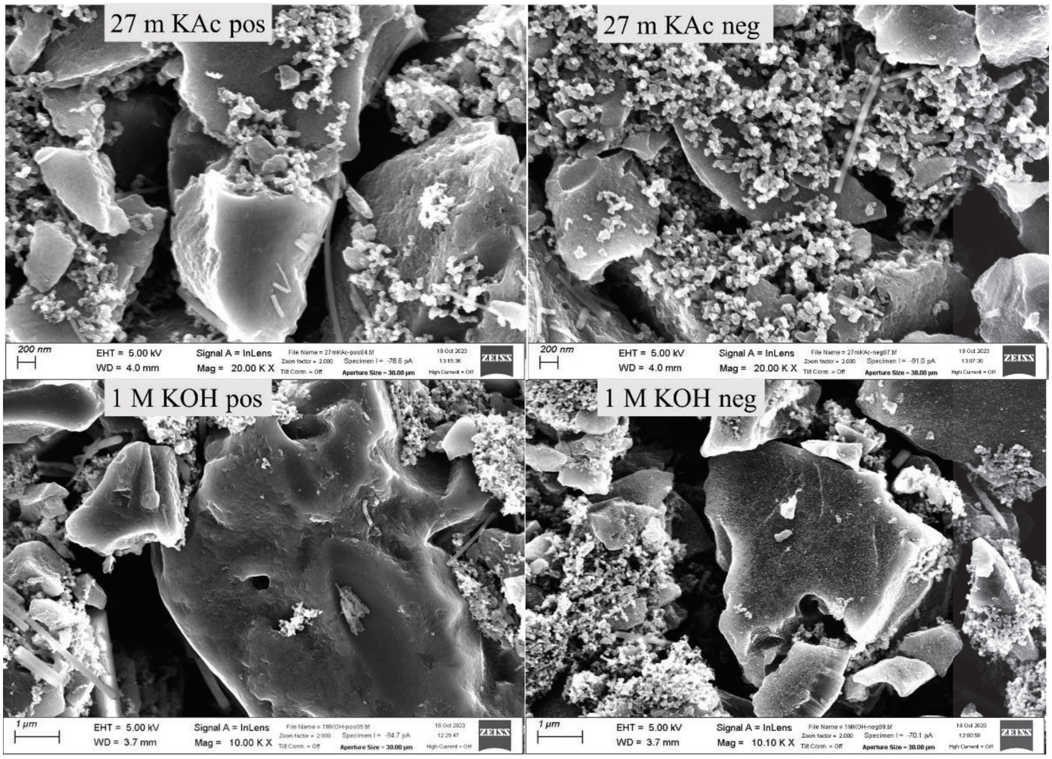

Figure 5.8. Medium-magnification SEM image of post-mortem electrodes after 40,000 cycles at 2V.

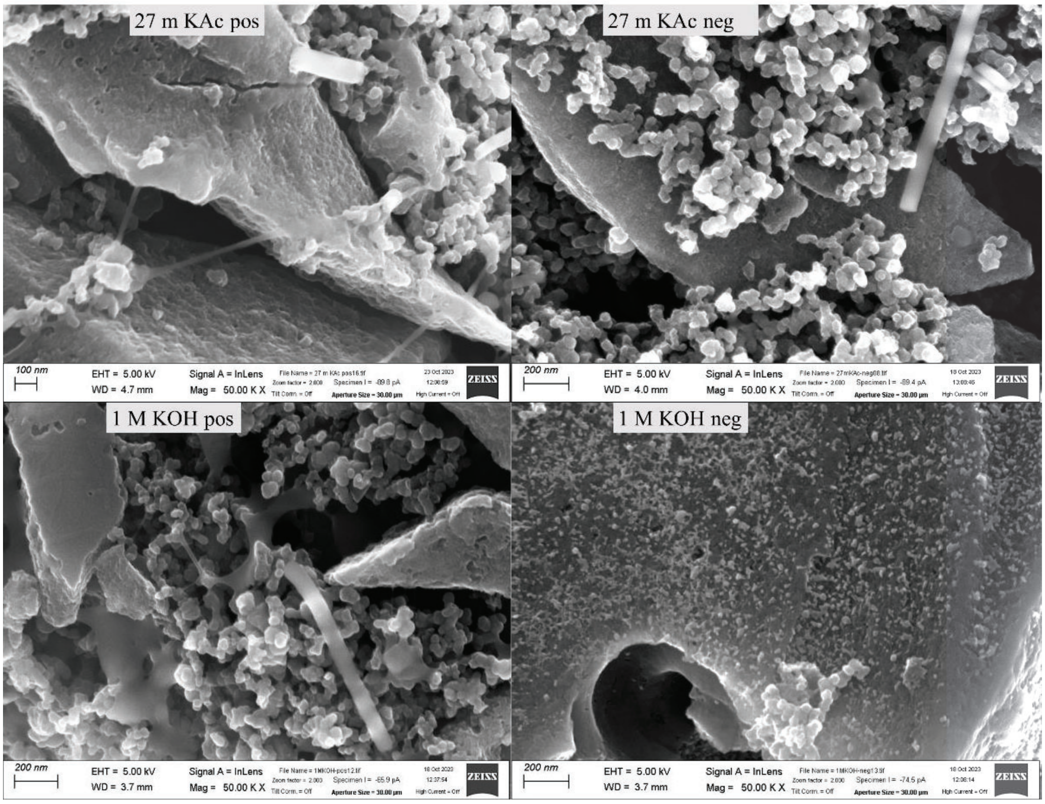

Figure 5.9. High-magnification SEM image of post-mortem electrodes after 40,000 cycles at 2V.

The chemical composition of the elements in the electrodes was analysed using the energy dispersive spectroscopy (EDS) technique, and the results are presented in Figure 5.10. The main objective was to find differences between the electrodes as well as to search for the origin of the deposits on the 1 M KOH negative electrode. EDS analysis reveals an atomic Si content of 3% and 0.8% for the 1 M KOH negative and positive electrodes, respectively, and 0.12% and 0.15% for the 27 M KAc negative and positive electrodes, respectively. Based on EDS results, the fact that the precipitate did not dissolve during the first wash, and the similar Si content across all electrodes after a thorough second wash, we suspect that the fibreglass membranes partially dissolve in the presence of the highly basic 1 M KOH electrolyte [127], leading to the formation of silica precipitates [128].

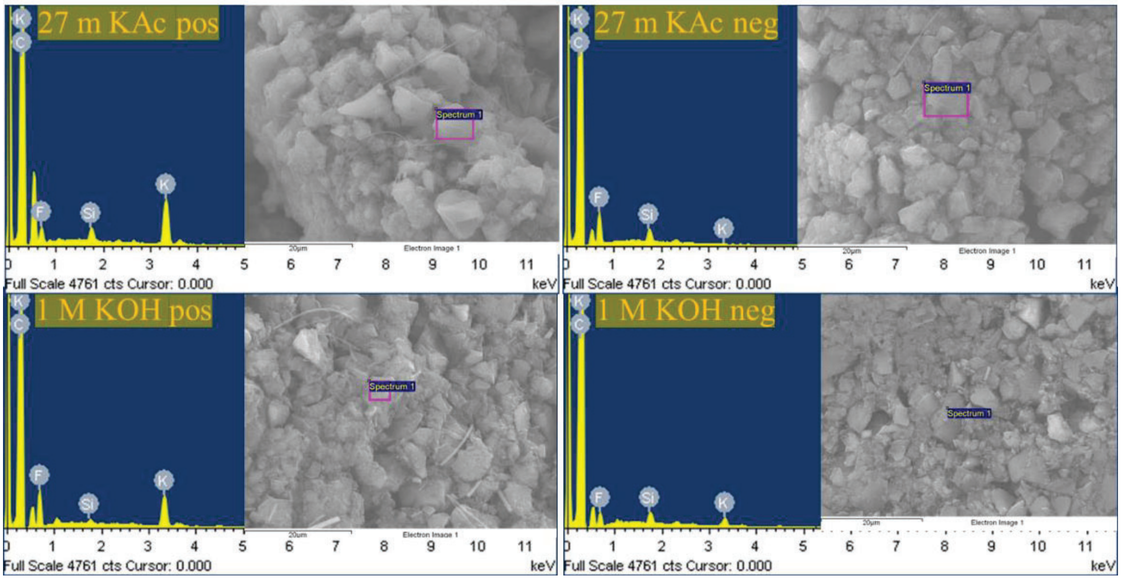

Figure 5.10. Energy dispersive spectroscopy of post-mortem electrodes after 40,000 cycles at 2V.

Fourier Transform Infrared (FTIR) spectrum was obtained for fresh and post-mortem electrodes cycled in 27 m KAc and 1 M KOH. Results are shown in Figure 5.11. Post-mortem electrodes show a very similar pattern, with marked differences to the fresh electrode pattern. The bands at 1100 and 800 cm^{-1} are associated with the asymmetric and symmetric Si-O-Si stretching vibration bonding [129]. The reaction with potassium acetate and potassium hydroxide electrolytes is related to the presence of oxygen functional groups clearly shown in a band at 1370-1450 cm^{-1} corresponding to bending vibrations of C-H aliphatic groups [130], a marked absorption peak, related to potassium electrolytes [131], corresponding to carbonyl groups, C=O stretching vibration at 1725 cm^{-1} [132], a band at 2850-2950 cm^{-1} corresponding to C-H stretch of alkane groups (single-bonded carbon atoms) [133], and the appearance in the positive electrodes of a broad band between 3000 and 3500 cm^{-1} attributed to the presence of hydrophilic O-H groups that promotes wettability [134].

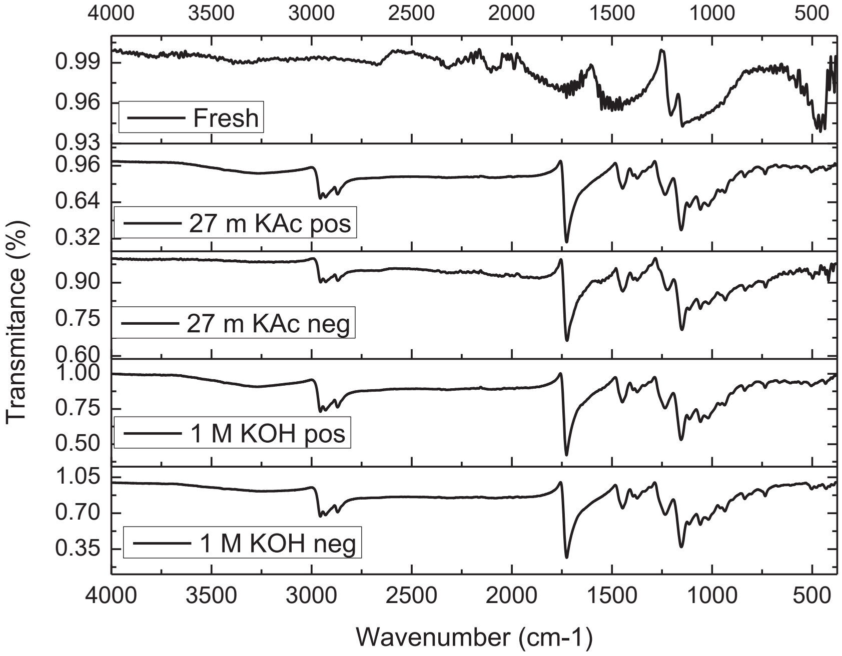

Figure 5.11. FTIR for fresh and post-mortem electrodes in 27 m KAc and 1 M KOH electrolytes after 40,000 cycles at 2V.

X-Ray Diffraction (XRD) was used to observe the structure of the supercapacitor electrodes. The XRD patterns of fresh and cycled electrodes are presented in Figure 5.12. XRD patterns do not show significant changes in the position of the peaks or their intensity, revealing no notable changes at a structural level.

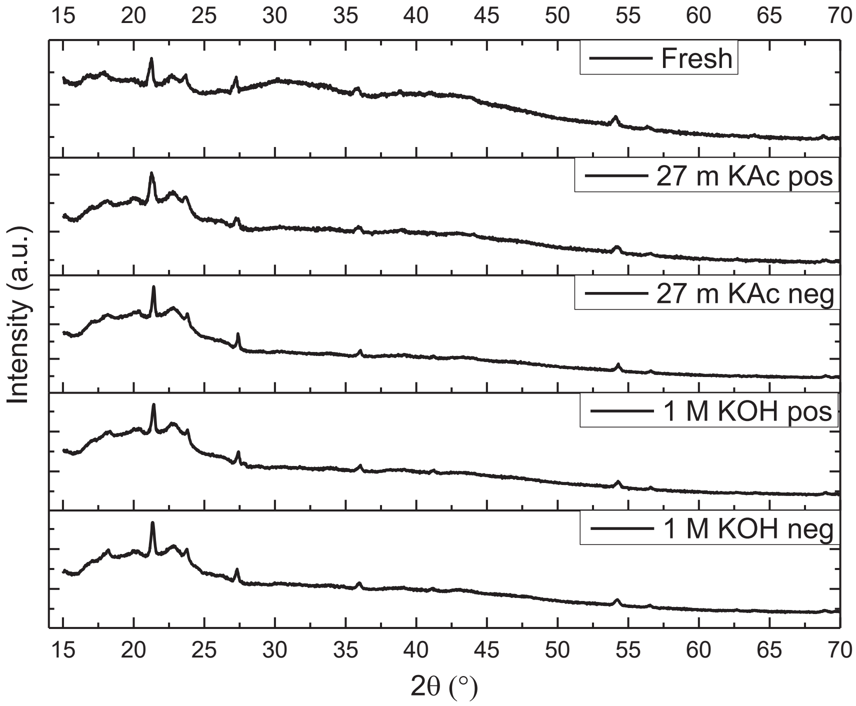

Figure 5.12. XRD diffraction patters of the fresh electrode and cycled ones after 40,000 cycles at 2V

Figure 5.13, 5.14, and 5.15 show XPS spectra of fresh (pristine) and cycled samples after 40,000 cycles at 2V. As the penetration depth is about 10 nm, XPS is presented as the ideal technique to identify the elemental composition and chemical bonds of functional groups in post-mortem analysis. Four samples belonging to the negative and positive electrodes of the 1 M KOH and 27 m KAc electrolytes were analysed and compared to fresh electrodes.

The C1s spectrum, Figure 5.13, shows the appearance of a peak around 295-296 eV, which is attributed to the formation of CF_3 groups [135]. This formation is related to an increase in hydrophilicity [136]. Peak broadening is observed around 286-290 eV, corresponding to an increase in the C-O and O-C=O groups in all samples except for the negative electrode of 1 M KOH. In the latter, the disappearance of the 290 eV peak corresponding to the π-π* transition is observed, which would cause a decrease in the conductivity of the electrodes [137] and was related to the increase in impedance. A reduction in the functional groups that contain oxygen is also observed in the negative electrode of 1 M KOH, with the peak around 288.5 eV remaining very marked, which is related to O-C=O bonds as well as carbonates, which would explain the deposits observed in the SEM images. In addition, a peak around 282.9 eV was assigned to metal carbide and related to the formation of potassium carbide or silicon carbide [138] and to a displacement in the C=C peak.

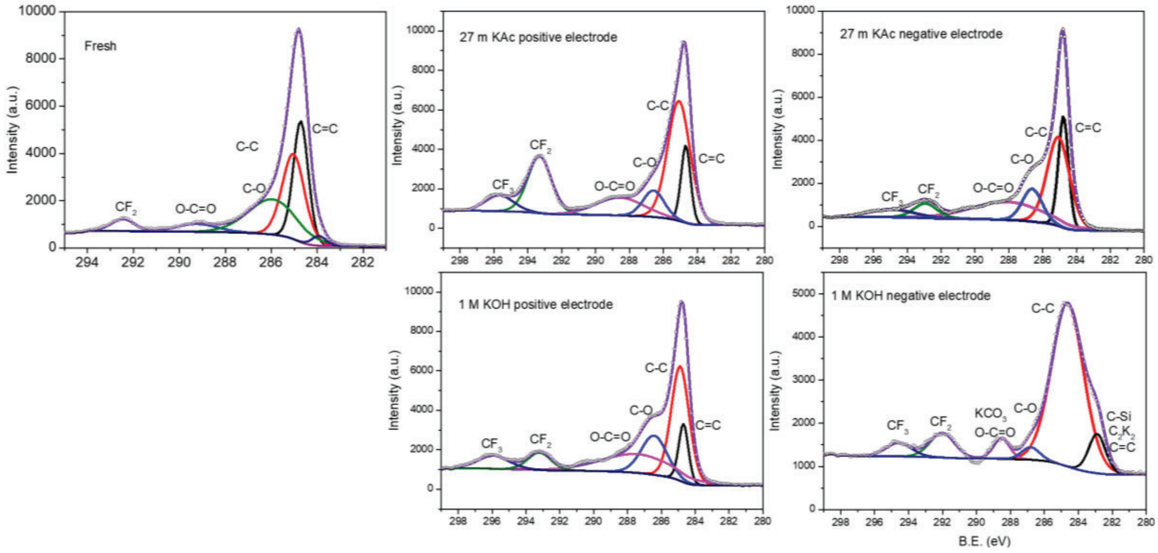

Figure 5.13. XPS C1s spectra of pristine carbon electrodes and after 40,000 cycles at 2V.

For the XPS study of the O1s spectrum, Figure 5.14, deconvolution into five peaks was used [82]. The samples cycled in 27 m KAc better preserved the spectrum's shape than the 1 m KOH after cycling at 2V. For 27 m KAc positive samples, the absorbed water and the -COOH groups are practically eliminated. The OH groups are reduced for the negative samples cycled in 27 m KAc. Samples cycled in 1 M KOH show a pronounced hump in the low energy part, increasing the separation between the C=O and C-OH groups by 0.8 V for the negative electrode and by 1.5 eV for the positive electrode, a strong decrease in C-O-C groups, and a decrease in water adsorption. In addition, both the cycled positive and negative electrodes in 1 M KOH exhibit better preservation of -COOH groups compared to those in 27 M KAc, which is associated to better hydrophilicity.

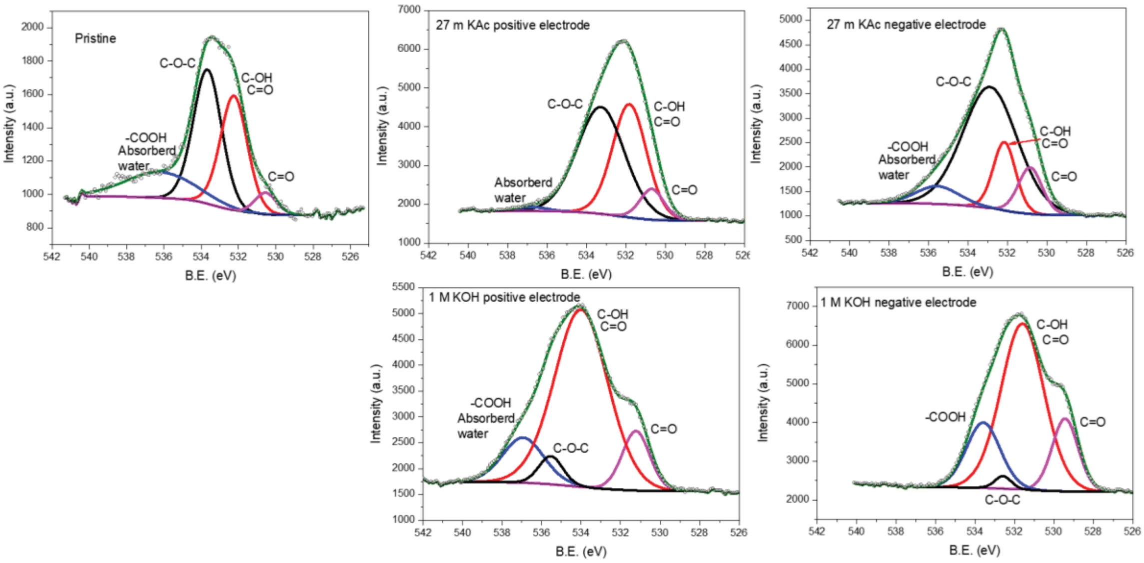

Figure 5.14. XPS O1s spectra of pristine carbon electrodes and after 40,000 cycles at 2V.

For the XPS study of the F1s spectrum, Figure 5.15, deconvolution into three peaks was used for the non-cycled sample, relating from lowest to highest energy with CF, CF_2 and CF_3/F-O bonds [84], [139] and probably related to absorbed water, as in the O1s spectrum, Figure 5.14. The positive electrode cycled in 27 m KAc only needs two peaks corresponding to the CF and CF_2 of the PTFE, probably due to the elimination of practically all the adsorbed water and the -COOH groups. For the negative electrode, a third peak is needed as for the fresh sample. The positive electrode cycled in 1 M KOH shows a significant increase in the CF_3/F-O peak, which correlates with the broadening of the O1s peak. The negative electrode also exhibits an increase in these features, although to a lesser extent than the positive electrode. This difference suggests that the positive electrode undergoes more pronounced surface modifications in the 1 M KOH environment, possibly enhancing its hydrophilicity through the formation of functional groups.

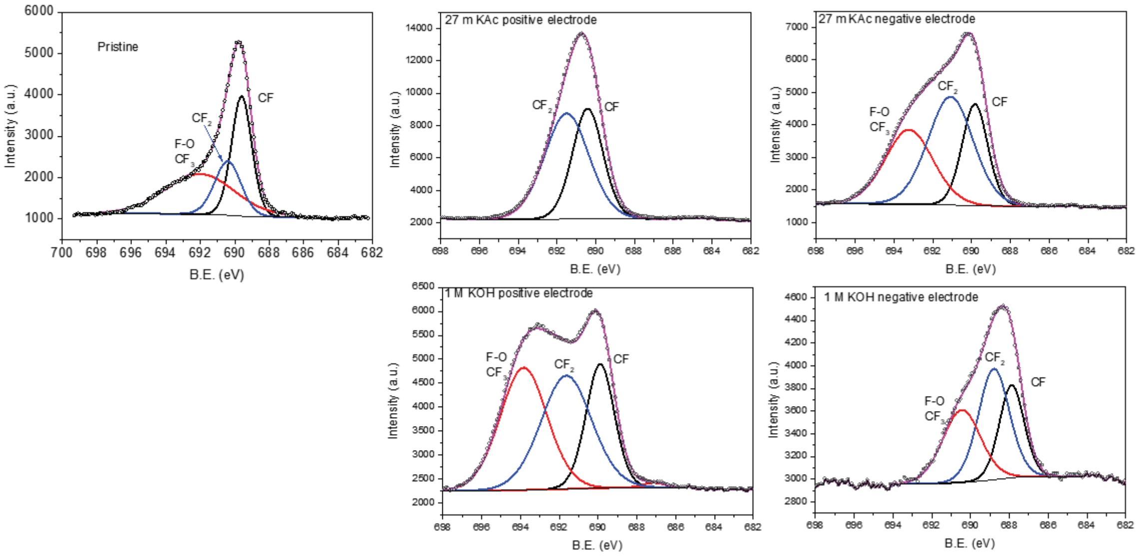

Figure 5.15. XPS F1s spectra of pristine carbon electrodes and after 40,000 cycles at 2V.

In this section, we have carried out degradation studies and post-mortem analysis of symmetrical activated carbon capacitors with the super-concentrated electrolyte 27 m potassium acetate, and we have compared the results with the aqueous electrolyte 1 M KOH. For this, we have carried out a complete electrochemical characterization, accelerating the degradation with a stress potential of 2V. Once the cell was degraded, we conducted physicochemical and structural characterization of the degraded components using SEM, EDS, FTIR, XRD and XPS. The SEM images reveal the presence of precipitates on the negative electrode of the 1 M KOH cell. These precipitates are likely related to silica deposits, which result from the dissolution and subsequent precipitation of a small amount of the fibreglass membrane. The FTIR spectra show a similar pattern for all electrodes with the creation of numerous functional groups (bands appearing at 1725 cm^{-1} and the band between 2850-2950 cm^{-1} corresponding to C=O and C-H bonds, respectively), which could be related to the decrease in capacity and increase in resistance. The XRD analysis does not reveal changes at the structural level. The XPS analysis shows the appearance in all samples of a new peak at 295-296 eV related to the degradation of the PTFE binder of composition CF_2 by the formation of CF_3. Oxygen functional groups also appear for all samples. In addition, the loss of the 290 eV peak in the 1 M KOH negative electrode appears to be related to a loss of conductivity and the appearance of the precipitates observed with the SEM. The broadening of the O1s spectrum is observed in both positive and negative for the 1 m KOH cell. The F1s spectrum broadens the two negative electrodes for the 27 m KAc cell. The positive electrode of 1 M KOH shows a large broadening after prolonged cycling at 2V, which was related to the formation of CF3 due to binder degradation.

5.3.3 Cell reassembly

We used Swagelok cells equipped with glassy carbon current collectors to complement our degradation studies since they can be easily opened and closed, allowing better access to the components and their reuse. Glassy carbon is a material with high hardness, low chemical reactivity and high electrical conductivity, which prevents the appearance of parasitic reactions that mask the electrochemical processes [140]. Two cells were prepared with a symmetrical arrangement of activated carbon electrodes, separated by a fibreglass membrane and soaked in a 27 m KAc electrolyte, to which we assumed a potential window of 1.8 V. A voltage stress was applied to accelerate degradation, where the cells were cycled within a 2 V potential window (as described in previous sections) for 10,000 cycles using galvanostatic charge and discharge at a rate of 1 A/g. After 10,000 cycles, one cell, referred to as "rest 24 h" or "rest", was allowed to rest for 24 hours. Meanwhile, the other cell, referred to as “change”, was disassembled, its electrodes were washed and dried, and then reassembled into a new Swagelok cell with a fresh membrane and electrolyte. Both the “change” cell and the “rest” cell were subsequently cycled for an additional 10,000 cycles. After this second set of cycles, both cells were dismantled for post-mortem studies to investigate any changes in the electrodes, membrane, and electrolyte due to prolonged cycling.

Figure 5.16 shows the electrochemical results of Swagelok cells containing the 27 m KAc electrolyte and cycled in the potential window of 2 V. During the first 1,000 cycles, the cells experienced an average capacitance reduction of 18.5% (Figure 5.16.a). The reduction in capacitance continued at a slower rate, with an average drop of 35.4% after 10,000 cycles.

After the process of "change" or "rest," the cells underwent another 10,000 galvanostatic cycles at 1 A/g within a voltage window of 2 V. The capacitance of the cells partially recovered, increasing by 20.6% and 17.1%, respectively. However, over the next 1,000 cycles, the capacitance experienced an abrupt decline of 15.3% and 17.1%, respectively. During the subsequent cycles, the capacitance continued to decrease for both cells, reaching cycle 20,000 with a similar overall decline of 40.7% and 44%, respectively (Figure 5.16.a). It should be noted that the capacitance loss patterns were very similar for both cells.

The nearly triangular shape of the galvanostatic charge-discharge cycles shows the capacitive behaviour of the activated carbon electrodes (Figure 5.16.b). A reduction in charge and discharge times can be observed between cycle 1 and cycle 10,000, followed by a recovery at cycle 10,001, after either changing the membrane and electrolyte or resting for 24 hours. This is then followed by a subsequent reduction in times, continuing until reaching cycle 20,000.

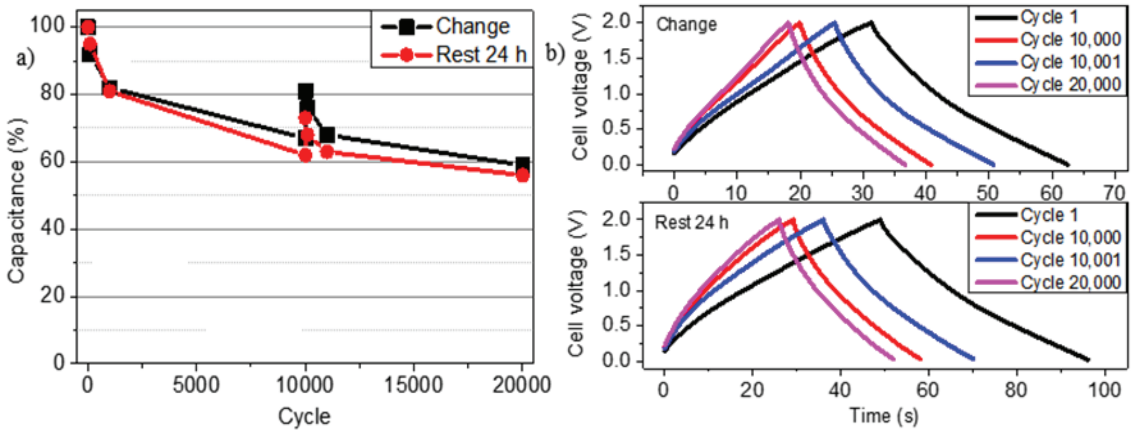

Figure 5.16. Galvanostatic charge-discharge. a) Cell capacitance evolution during 20,000 cycles. b) Shape of different cycles.

The IR drop values were extracted from Galvanostatic charge-discharge plots and are presented in Table 5.3. The IR drop study shows that values remain extremely low and constant for both cells. The "change" cell has a constant IR drop of 12 mV during the first 10,000 cycles, which increases to 15 mV after changing the electrolyte and then decreases to 13 mV after 20,000 cycles. The "Rest 24h" cell has an initial IR drop of 13, increases to 15 during the first 1,000 cycles and reaches 13 mV at cycle 10,000. After 20,000 cycles, it decreases to 11mV. It should be noted that in the "change" cell, the IR drop increases when the electrolyte is changed, while it decreases in the "Rest 24h" cell. This was justified because the electrolyte needed some cycles in the "change" cell to fill the electrode's pores again, increasing the resistance. In contrast, the "Rest 24h" cell was already activated. The low value of the IR drop was assigned to a better electric contact between the activated carbon electrodes and the glassy carbon current collectors.

Table 5.3. IR drop (mV) of "charge" and "Rest 24h" cells as a function of cycles.

Cycle number	1	1,000	10,000	10,001	11,000	20,000
Change	12	12	12	15	14	13
Rest	13	15	13	11	13	11

The study of the impedances, Figure 5.17, shows similar behaviour for both cells with low ESR and CTR, even after 20,000 cycles. This is in good correlation with the low value of the IR drop of the galvanostatic experiments shown above. On the other hand, the Nyquist plots show significant differences in low-frequency data, which were investigated through the Warburg coefficient.

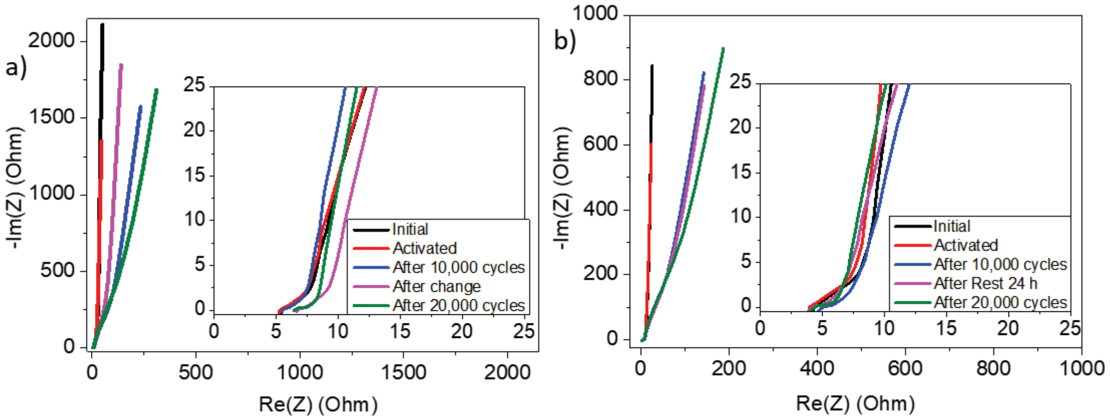

Figure 5.17. Impedance evolution during 20,000 cycles. a) “Change” cell. b) “Rest” cell.

The Warburg coefficient (σ) is proportional to the inverse of the square root of ions diffusion. It can be calculated from the slope of the representation of the real part of the impedance at low frequency with respect to the inverse of the square root of the angular frequency. Results are presented in Figure 5.18. The initial slope and after activation averaged 6.3, indicating a low value of σ, which implies high ion diffusion. After 10,000 cycles, the "change" cell reached a slope value of 58.5, which decreased to 29.7 after the electrolyte and membrane were replaced, and the electrodes were washed. The slope then increased to 87.3 after 20,000 cycles. For the "rest" cell, the slope after 10,000 cycles was 37.7, with no significant changes following the rest period, but it increased to 52.8 after 20,000 cycles.

The improvement in the diffusivity of the “change” cell after 10,000 cycles, by changing the electrolyte and the membrane and washing the electrodes, was attributed to a better flow of ions through the membrane and improved ion access to the pores by eliminating accumulated deposits. The improvement in diffusion could not be maintained in the following cycles, with σ reaching its higher value after 20,000 cycles for both cells.

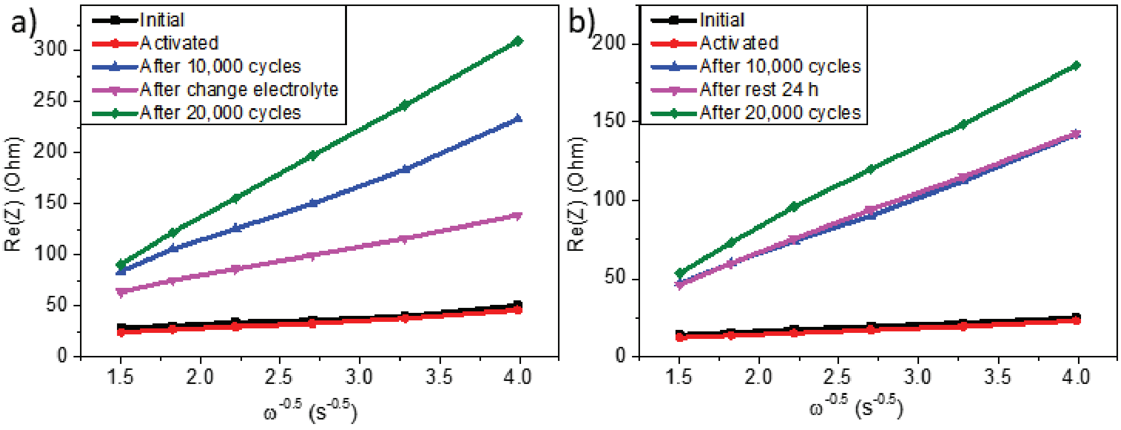

Figure 5.18. Plot of the real part of the impedance vs. ω-0.5. a) “Change” cell. b) “Rest” cell.

The values of the Warburg coefficient are represented in the Table 5.4.

Table 5.4. Warburg coefficient for different cycling states for “change” and “rest” cells.

	Initial	Activated	10,000 cycles	After	20,000 cycles
Change	8.3	8.4	58.5	29.7	87.3
Rest	4.3	4.2	37.7	38.6	52.8

5.4 Discussion

We have carried out a failure mode and effects analysis (FMEA) of the symmetrical activated carbon supercapacitors in super-concentrated 27 m KAc subjected to degradation by stress voltage (Table 5.5). Failure Mode and Effect Analysis (FMEA) is a systematic approach used to identify and evaluate the potential failure modes of a product or process and their effects on performance. Failure modes are classified according to their effect, severity, and frequency. They are used to take actions to eliminate or mitigate failures, prioritizing those with the greatest impact. Basically, the steps to follow are: 1) Identify potential failure modes. 2) Determine the effects of each failure mode. 3) Analyse the causes. 4) Evaluate the severity, occurrence, and early detection. 5) Prioritize the failure modes. 6) Develop mitigation strategies.

Corrosion is a failure mode of current collectors. It depends on their manufacturing material and their reactivity with the electrolyte. The decomposition of the electrolyte in the positive electrode leads to the formation of oxygen that would oxidize the current collector. This would generate a loss of electrical conductivity between the electrode and the current collector with increased resistance and reduced capacitance. Although no visible oxide formation was observed in the visual inspection of stainless-steel current collectors, it is well known the formation of a passivation film of chromium oxide on the surface, that increases with the voltage applied, protecting from corrosion but increasing resistivity. The IR drop observed after 10,000 cycles was 0.012 V for the Glassy Carbon Current Collectors (GCCC) compared to 0.81 V for the Stainless-Steel Current Collectors (SSCC), indicating better electrical contact for the GCCC. Additionally, the GCCC cell demonstrated greater capacitance retention, maintaining 67% compared to 46% for the SSCC after the first 10,000 cycles. We assign a high failure level to this failure mode.

Pore blocking is a failure mode that affects carbon electrodes. It occurs due to the reaction of carbon with oxygen produced by the decomposition of the electrolyte, a process determined by the electrolyte's stability window. The generation of gases such as H_2, O_2, and CO_2 leads to pore blockage, which hinders electrode-electrolyte contact, resulting in increased resistance and decreased capacitance. FTIR and XPS experiments indicate an increase in these functional groups, which are involved in the reduction of device performance, which is why we have assigned to this failure mode a high failure level.

The loss of electrode cohesion is a failure related to the deterioration of the binder. We have used PTFE, whose formula is CF_2, due to its great chemical stability, flexibility, low friction, high electrical resistance, and the fact that it is insoluble in any solvent. Analysing the cycled electrodes with XPS, we observed an increase in CF3 bonds in both electrodes, which could be related to a loss of cohesion in the binder. Visual observation did not reveal signs of disintegration of the electrode. SEM observation showed no agglutination or areas where the active material and the conductor were not in contact. Therefore, we assign a medium-low severity to this failure mode.

The oxidation of water is a failure associated with aqueous electrolytes in which water decomposes into oxygen, protons, and electrons, the latter two being used in the production of hydrogen, completing the water splitting. This reaction limits the stability window of the electrolyte due to the precipitation of salts and/or the evolution of gases that cause an increase in the resistance of the cell and a reduction in the capacitance due to pore blocking. The electrolyte was the super-concentrated potassium acetate 27 m, to which a voltage stress of 2 V was applied for 10,000 cycles. Changing the electrolyte or letting the cell rest does not make a big difference after 20,000 cycles in capacitance retention, with values of 59 % and 54 %, respectively. As the stability of the electrolyte is the main factor incident in the pore blocking, we assign a high failure level to this failure mode.

The short circuit of the capacitor can be considered the worst failure since the device stops working completely. This failure is usually due to a break in the membrane with the formation of holes or cracks. This would put the positive and negative electrodes in direct contact, causing the rapid passage of electrons and a strong electric discharge between plates. In the supercapacitors, we have used fibreglass membranes which have good mechanical properties, and this phenomenon was not observed, so we have assigned a low failure level to this failure mode.

Table 5.5. Failure Mode and Effects Analysis of activated carbon electrodes in 27 m K acetate.

Failure	Component	Failure analysis		Failure effect		Techniques	Detection method	Cell re-assembly	Failure level
		Failure mode	Failure cause	Local effect	System effect				
Current collector (CC) corrosion	Stainless steel (SS) Glassy carbon (GC)	Corrosion	Electrolyte composition Long cycling Excessive voltage	Loss of conductivity between electrode and current collector	Resistance (R) increase Capacitance (C) decay High-rate C reduction	Charge - discharge (Ch-dch) Impedance spectroscopy (EIS) Cyclic voltammetry (CV)	Corrosion not observed R increase C decay	No. SS CC Yes. GC CC	High
Pore blocking	Activated carbon electrodes (ACE)	ACE Oxidation	Limited electrolyte stability window	Pore blocking: CO/CO_2 surface group formation in ACE Pore formation: AC oxidation and CO_2 evolution	R increase C reduction High-rate C reduction Shorter cycle life	Ch-dch EIS CV	Coin cell swelling not detected. FTIR, XPS increase of functional groups	ACE washed New membrane & electrolyte	High
Structural degradation	ACE + Super P conductive + PTFE binder	Particle cohesion loss	Long cycling Excessive voltage	Contact loss between active and conductive particles (PTFE binder degradation CF_2-->CF_3)	R increase C reduction High-rate C reduction Shorter cycle life	Ch-dch EIS CV	XPS: binder degraded SEM: no change	ACE washed New membrane & electrolyte	Medium-low
Liquid electrolyte decomposition	Super saturated electrolyte 27 m K acetate	Oxidation of water	Limited electrolyte stability window	Precipitation of salt & pore blocking. Gas evolution from water splitting. Electrode oxidation	R increase C reduction High-rate C reduction Shorter cycle life	Ch-dch EIS CV	SEM/EDS salt not detected on degraded ACE	Fresh electrolyte	High
Membrane deterioration	Glass fibre membrane	Short circuit	Dendrites & precipitates	Pin holes and craks	No voltage	Ch-dch EIS CV	Total failure not observed	New membrane	Low

5.5 Conclusions

By analysing the results obtained in this section, we believe that applying excessive voltage to an aqueous electrolyte leads to water splitting and gas generation. This process hinders contact between the electrode and the electrolyte by blocking the pores, resulting in a sharp drop in capacitance during the first 1,000 cycles, observable at the beginning of the experiments, after changing the electrolyte and membrane or when the cell is allowed to rest. We believe that the main degradation mechanism of the electrodes occurs due to the loss of carbon active material, which reacts with O_2 generated during water splitting, resulting in the formation of CO_2. This CO_2 would contribute to blocking pores along with the O_2 and H_2 coming from the division of water until reaching the equilibrium concentration at approximately 1,000 cycles. Another degradation mechanism would be motivated by the degradation of the electrolyte, which would increase its concentration with reduction of the ionic conductivity and possible precipitation of salts on the electrode. Finally, the oxidation of the current collectors can reduce conductivity, increase resistance, and decrease capacitance, thereby shortening the lifespan of the capacitor.

6 Hybrid supercapacitors in water-in-salt and organic electrolytes

6.1 Introduction

Supercapacitors are characterized by their fast charging and discharging, high power, excellent cyclability and low maintenance. On the other hand, batteries are characterized by their high specific energy [141]. Trying to take advantage of the positive qualities of both devices, numerous attempts have been made to integrate the best of each system into the so-called hybrid capacitors, that is, those that are formed by a capacitive electrode like those used in capacitors, usually made with carbonaceous materials, and another electrode like those used in batteries, usually made with a metal oxide. Hybrid capacitors are designed as versatile accumulators that can work at different charging regimes. In fast charges the capacitive electrode would be able to be fully charged in a few seconds, while in slow charges both electrodes could be fully charged.

This chapter is dedicated to the study and manufacturing of hybrid capacitors. The capacitive material used is YP50 activated carbon while for the faradaic one we have used the typical battery materials lithium titanium oxide (LTO) and lithium iron phosphate (LFP) as negative and positive electrodes respectively [71], [142].

6.2 Lithium titanium oxide hybrid capacitor

Lithium Titanium Oxide (LTO) is a material widely used in batteries, been explored the hybridization with capacitive materials [143]. In this chapter we tried to make a hybrid AC/LTO capacitor with the organic electrolyte $LiPF_6$. For the negative electrode was used commercial LTO on copper foil. For the positive electrode, YP50, super P and PVDF were mixed in 85:10:5 proportions dissolved with NMP, mixed using the ball milling technique and spreading the paste on an aluminium sheet.

The cells were cycled by cyclic voltammetry (CV) with different potential window and scanning rate. The hybrid capacitor was able to give, in a potential window from 1 to 3 V, 30.2 F/g at a low rate of 0.6 mV/s (Figure 6.1.a), maintaining 16.7 F/g at 5 mV/s and 7.7 F/g at 20 mV/s (Figure 6.1b). For comparison, a symmetrical capacitor AC/AC on aluminium foil was made and was capable of giving 13.2 F/g at 5 mV/s and 10 F/g at 20 mV/s (Figure 6.1.c).

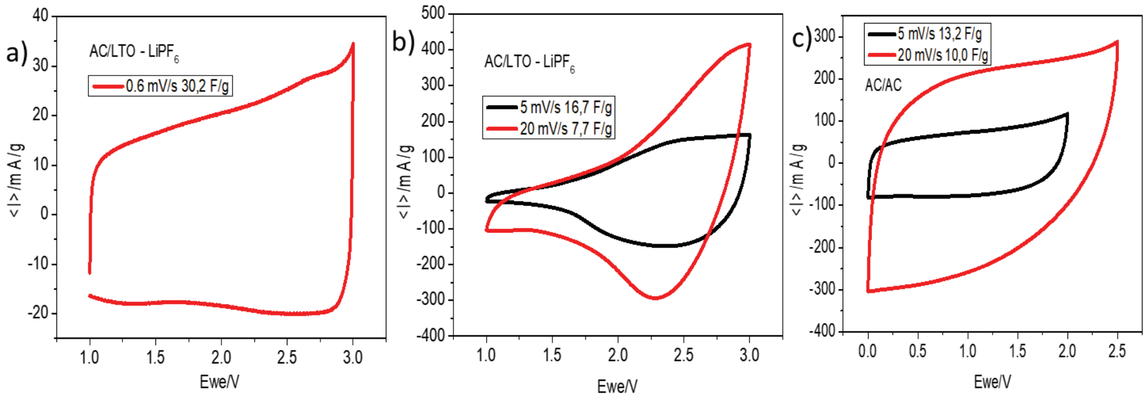

Figure 6.1. Cyclic voltammetry of AC/LTO hybrid capacitor a) and b) and of AC/AC symmetric capacitor c).

To complete the study of LTO hybrid capacitors, hybrid electrodes [144] were fabricated by mixing equal parts of LTO and YP50 activated carbon (AC) using PVDF as binder and NMP as solvent. Identical hybrid electrodes were separated by a fibre glass membrane soaked with $LiPF_6$ organic electrolyte in coin cell type device and sealed under Ar atmosphere in a glove box. The hybrid electrode capacitor was cycled at 5 mV/s in a potential window of 1.2 V, where it was capable of giving 7.2 F/g (Figure 6.2.a). This capacitance is practically half that of the AC capacitor (Figure 6.1.c). Therefore, practically all the capacitance was attributed to the contribution of the activated carbon and that the part coming from the LTO was practically null. To verify the influence of the electrolyte, the hybrid electrodes were tested with the organic electrolyte 1.2 M LiFSI in EC/EMC/DMC. Cyclic voltammetry was performed at 0.1 mV/s in a potential window of 1.5 V (Figure 6.2.b), finding a capacitance of 5.3 F/g, similar to $LiPF_6$. The low capacitance of mixed electrodes was attributed to the fact that LTO is only used in batteries as negative electrode material and has limited use in positive electrodes [145].

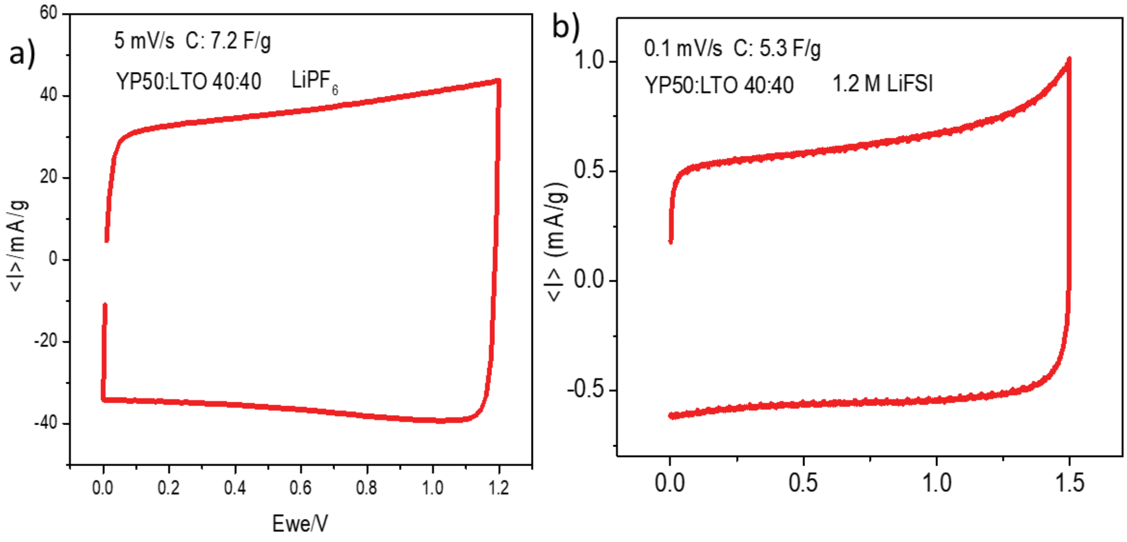

Figure 6.2. Cyclic voltammetry of AC/LTO mixed electrodes in LiPF6 at a scan rate of 5 mV/s a) and LiFSI at 0,1 mV/s b).

6.3 Lithium iron phosphate hybrid capacitor

Lithium Iron Phosphate (LFP) is a material widely used as a cathode in lithium batteries due to its high safety, durability, and power. LFP also has a more constant discharge voltage, and its materials are cheaper and less toxic than other lithium batteries [146]. These advantages compensate for its lower energy density, making LFP a material with a very high potential in future applications. With the aim of using its high power and durability, hybrid capacitors were manufactured with LFP, battery type material, in the positive electrode and activated carbon YP50, capacitive type material, in the negative electrode.

For the manufacture of the positive electrode, LFP was used as active material, super P as electronic conductor and PTFE as binder in proportions 80:15:5. A sufficient amount of ethanol was added and mixed with the ball milling technique for 10' at 20 Hz. The paste obtained was spread on an aluminium sheet with the Dr. Blade technique and left to dry in the vacuum oven at 110 ºC for 24 hours. The negative electrode was made with ball milling technique with YP50, super P and PTFE in proportions 85:10:5 and enough ethanol, rolling and pressing the paste until having a self-supporting electrode. Electrodes were placed in a coin cell and separated by a Whatman GF/A membrane soaked with 1 M $LiPF_6$ organic Electrolyte.

The cells were cycled by cyclic voltammetry (CV) in a potential window of 2.9 V and different scanning rates from 0.1 to 50 mV/s and their impedance (EIS) was studied. The hybrid capacitor delivers 20.9 F/g at the low rate of 0.1 mV/s (Figure 6.3.a), maintaining 9.1 F/g at 5 mV/s, 8.7 F/g at 20 mV/s and 6 F/g at 50 mV/s. We can compare with the symmetrical AC/AC capacitor who gave 13.2 F/g at 5 mV/s and 10 F/g at 20 mV/s (Figure 6.1.c). In Figure 6.3.b we can observe the change in impedance due to the formation of a passivation layer called solid electrolyte interface (SEI). The SEI is deposited as the electrolyte and the electrode react during cycling. This layer prevents the electrolyte oxidation at high potentials although it increases the resistance and therefore reduces the rate of cycling [147].

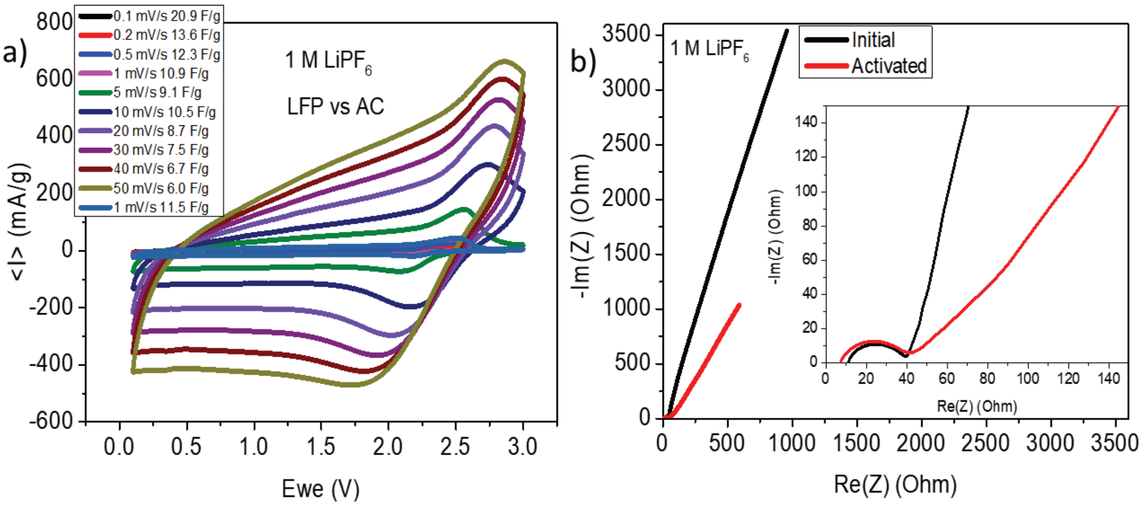

Figure 6.3. Cyclic voltammetry a) and impedance b) of LFP/AC hybrid capacitor in 1 M LiPF6 organic electrolyte.

The hybrid capacitor was also tested with 32 m KAc + 6 m LiAc super-concentrated aqueous water-in-salt electrolyte (WIS) with cyclic voltammetry (CV) and scanning rates from 0.1 to 50 mV/s in a potential window of 1.8 V, and impedance spectroscopy (EIS). Cyclic voltammetry surprised by giving excellent capacitances of 52.4 F/g at 0.1 mV/s, 40.6 F/g at 1 mV/s, 22.6 at 5 mV/s and 13.3 at 10 mV/s (Figure 6.4).

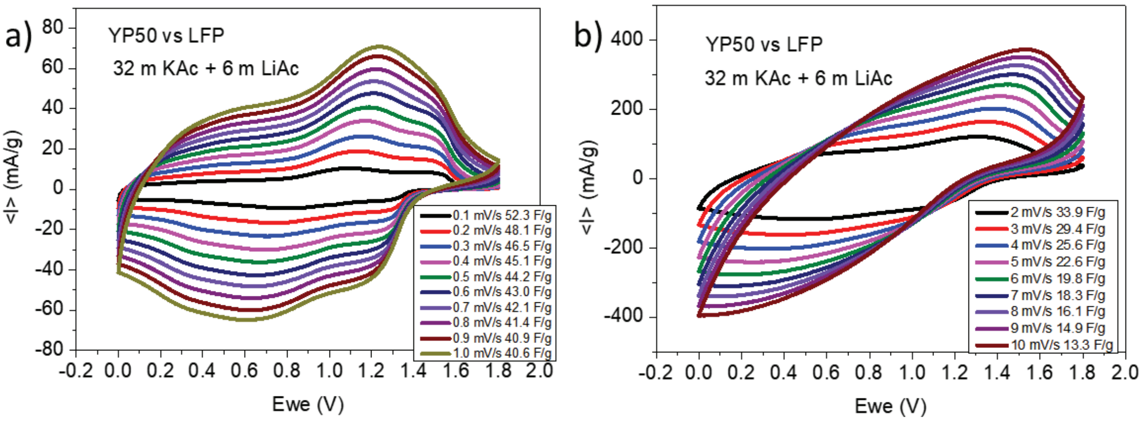

Figure 6.4. Cyclic voltammetry at low-rate a) and medium rate b) of LFP/AC hybrid capacitor in WIS electrolyte.

The impedance of the hybrid capacitor in WIS electrolyte showed similar electrolyte resistance (R_s) than organic electrolyte but higher CTR and a less vertical tail, both in the initial impedance and after cycling (Figure 6.5.a). The inclination of the tail, approximately 45° was related to a typical Warburg impedance of batteries, the same can be said of the wide semicircle (CTR). These considerations are supported by the higher capacitance shown by the aqueous electrolyte at low and medium rate, although at high rates it has slightly worse behaviour than organic electrolyte (Figure 6.5.b).

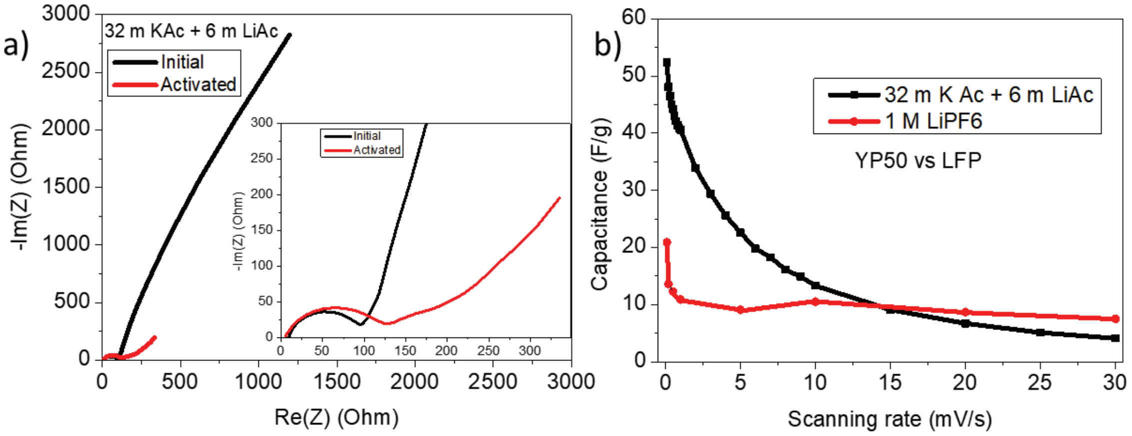

Figure 6.5. LFP/AC hybrid capacitor. a) Impedance with WIS electrolyte. b) Capacitance comparative of organic and WIS electrolytes.

As comparison, a half-cell with LFP battery type electrode vs Li metal in 1 M $LiPF_6$ organic electrolyte was studied with cyclic voltammetry and impedance. Cyclic voltammetry of battery-type materials shows a marked peak where redox reaction takes place (Figure 6.6.a), with a very different shape than that observed for the hybrid capacitors. Also the impedance showed different behaviour when compared to hybrid capacitors (Figure 6.6.b). The initial cycle showed a larger semicircle, related to a higher charge transfer resistance (CTR) and an almost vertical tail similar to hybrid capacitors. Once cycled, the CTR continues to grow until it doubles, when it barely grew in hybrid capacitors, and the tail grows and opens towards higher resistances, when in hybrids capacitors it was considerably reduced.

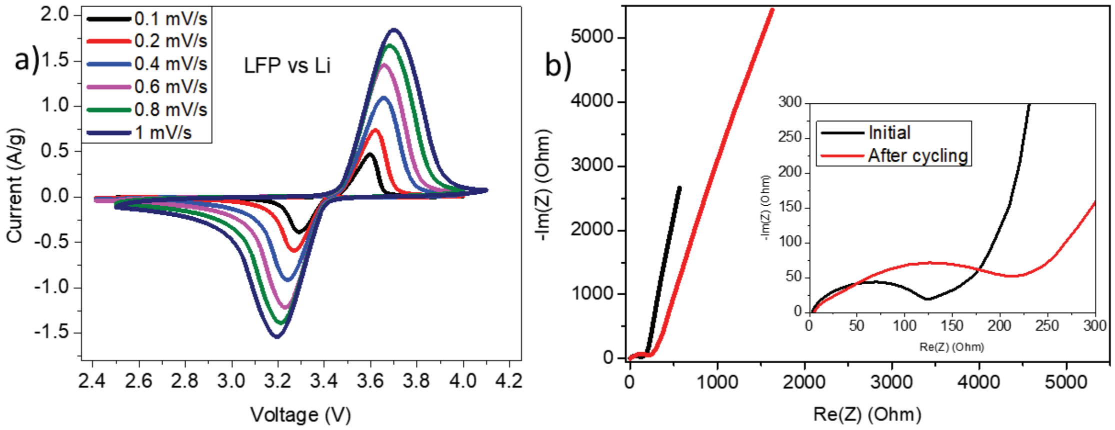

Figure 6.6. Half-cell LFP vs Li metal. a) Cyclic voltammetry. b) Impedance.

The study of the CVs allowed us to study the dependence of the current on the sweep rate. The processes that take place in the electrode can be divided into surface mechanisms where $\mathrm{d}i/dv$ is constant, i.e., capacitive processes, and diffusion-controlled mechanisms where $\mathrm{d}i/dv^{1/2}$ is constant [148], being able to establish a power-law relationship between the current i and the scan rate v through the formula:

$$i = av^b \qquad \text{(Eq. 6.1)}$$

Where b takes a value between 0.5 (diffusion limited process) and 1 (capacitive process) in a log(i) vs log(v) plot [149]. The values of b are compared for hybrid capacitor with different electrolytes showing higher values, higher capacitive behaviour, for aqueous electrolytes, 0.83 for 32 m KAc+6 m LiAc and 0.72 for 32 m KAc, been of 0.68 for 1 M $LiPF_6$ organic electrolyte. As comparison, the half-cell with LFP battery type electrode vs Li metal in 1 M $LiPF_6$ organic electrolyte shows a b value of 0.55, near to the theoretical value of 0.5 related to diffusion-controlled materials (Table 6.1).

Table 6.1. Comparison of b value for hybrid capacitor and half-cell battery electrode with different electrolytes.

Electrode	Electrolyte	b
YP50 vs LFP	32 m KAc + 6 m LiAc	0.83
YP50 vs LFP	32 m KAc	0.72
YP50 vs LFP	1 M $LiPF_6$	0.68
LFP vs Li metal	1 M $LiPF_6$	0.55

Taking into account that the current response can be classified as diffusion-controlled (faradaic battery-type) or surface-controlled (capacitive), the following general relationship can be applied for a given potential [30]:

$$i(V) = k_1 v^{1/2} + k_2 v \qquad \text{(Eq. 6.2)}$$

By dividing this equation by $v^{1/2}$ and through the graphical representation of $i(V)v^{-1/2}$ vs $v^{1/2}$, can be obtained the constants k1 and k2 and diffusion-controlled and capacitive current contributions can be plotted (Figure 6.7), where can be seen the different contributions to the current and how it agrees with the found value of parameter b.

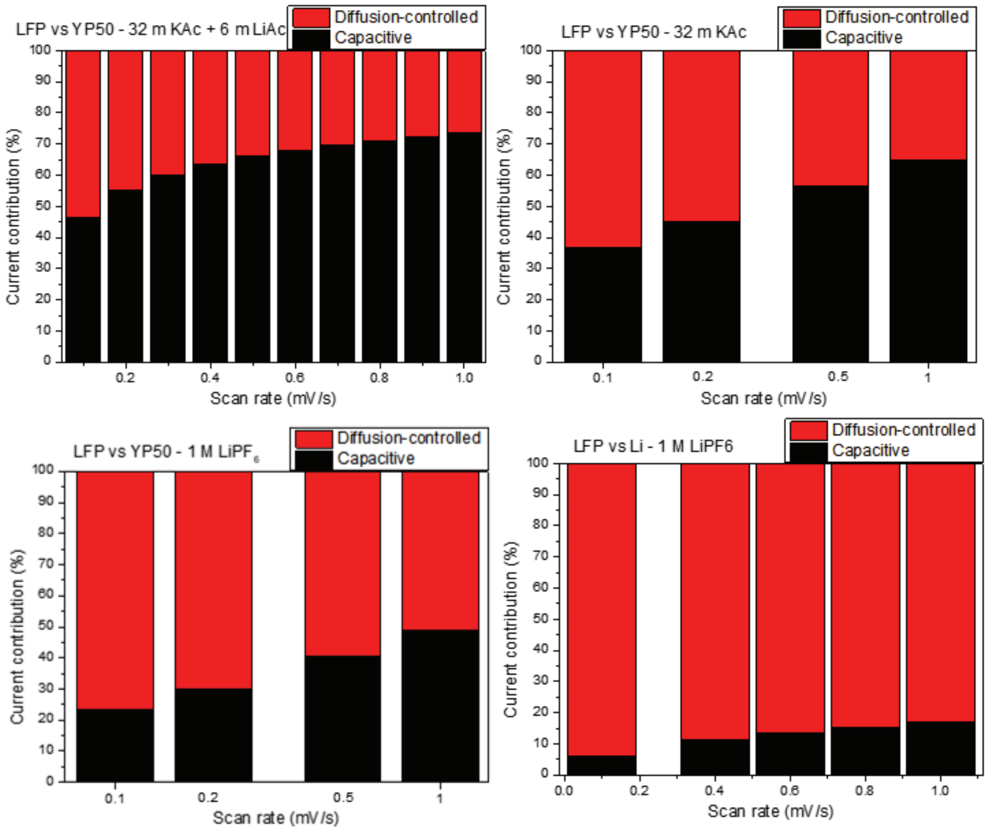

Figure 6.7. Current contribution from capacitive and diffusive mechanism for hybrid supercapacitors and half/cell battery.

6.4 Conclusions

In this chapter we have shown the viability of hybrid capacitors in aqueous and organic electrolytes, which, being halfway between batteries and supercapacitors in terms of stored energy and charge/discharge time, can occupy the empty space between these energy storage devices.

In the first part, we studied lithium titanium oxide (LTO) and YP50 activated carbon hybrid capacitor in organic electrolyte, finding good capacitance at low rate (30.2 F/g at 0.6 mV/s) and moderate capacitance at medium rate (16.7 F/g at 5 mV/s and 7.7 F/g at 20 mV/s).

In the second part, we studied lithium iron phosphate (LFP) and YP50 activated carbon hybrid capacitor in organic and super-concentrated water-in-salt electrolytes as well as LFP vs. Li metal. For organic electrolytes we find moderate capacitance at low and medium rates (20.9 F/g at 0.1 mV/s and 10.5 F/g at 10 mV/s) while for 32 m KAc + 6 m LiAc super-concentrated aqueous water-in-salt (WIS) electrolyte we find very high capacitance at low rate and moderate capacitance at medium rate (52.3 F/g at 0.1 mV/s and 13.3 F/g at 10 mV/s). The relationship between capacitive and faradaic processes has also been studied, showing the importance of the choice of electrolyte in order to enhance one process or another.

7 Conclusions and future work

7.1 Conclusions

One of the main objectives of this thesis is to elevate the energy and power of symmetrical carbon supercapacitors in aqueous electrolytes while broadening their potential window and thus be able to fill the gap between supercapacitors and batteries (chapters 3, 4 and 6). Various strategies have been explored, encompassing electrode mass equilibrium, thermal optimization, utilization of super-concentrated electrolytes, membrane selection, and integrating capacitive and faradaic materials within a unified device. In pursuit of these goals, efforts were made to diminish impedance and enhance energy efficiency, acknowledging the intrinsic interdependence of these factors.

The other main objective of this thesis is the degradation studies of the materials that make up the activated carbon supercapacitors (chapter 5). To this end, the forced electrochemical degradation of the capacitors in different aqueous electrolytes has been studied with special emphasis on the super-concentrated water-in-salt electrolyte 27 m potassium acetate (KAc). After electrochemical degradation, post-mortem physicochemical studies were carried out, and selected components were reassembled in a new cell.

The main conclusions of the first part of the thesis are related to the improvement of the performance of activated carbon and hybrid supercapacitors in aqueous electrolytes:

- The mass balance (chapter 3) between the positive and negative electrodes in 1 M KOH electrolyte has been adjusted by preparing electrodes with different mass loading and conducting long-term experiments with impedance studies in the potential window 1.2-1.6 V. It was found that the energy efficiency was the highest for a mass ratio (m_+/m_-) of 0.6, with efficiencies in long-term experiments of 82% at 1.2 V and 78% at 1.6 V. The high energy efficiency could be related to the impedance response since the device with a mass ratio of 0.6 had the lowest series resistance (Rs) and charge transfer resistance (CTR) of all the devices with a small increase when the voltage was increased from 1.2 to 1.6 V.

- Thermal treatment of the electrodes (chapter 3) was used in activated carbon capacitors with 1 M KOH electrolyte to reduce the impedance and increase the high-rate capacitance, which implies improving the power and increasing the potential window. Specifically, when the potential window was increased from 1.2 to 1.6 V, the electrodes treated at 240 ºC could deliver a high capacitance of 33.2 F/g with a retention of 70% when the rate was changed from 5 to 200 mV/s. This good performance at high rate was mainly related to the low impedance shown by the electrodes treated at 240 ºC.

- The influence of the membrane (chapter 3) was studied with the use of two commercial ones: glass fibre (GF) and polypropylene (PP). In high-rate and galvanostatic experiments, the performance of the GF membrane was much superior to that of PP. The GF membrane showed a capacitance retention of more than 80% when the rate was increased from 5 to 200 mV/s, even at a potential of 1.6 V, preserving the almost triangular shape of the galvanostatic charge-discharge plots. In contrast, the PP membrane showed a capacitance retention of less than 60% and a significant voltage drop at the beginning of the charge and discharge cycles. This behaviour was reflected in the impedance studies. The impedance plot of coin cells fabricated using GF membrane demonstrated the typical behaviour of capacitors with a small semi-depressed circle at high frequencies followed by an almost vertical tail of 87º at low frequencies. For PP-based coin cells, the low-frequency data was more complex, displaying the Warburg impedance characteristic of a diffusion process and a vertical tail at low frequencies. By maintaining the potential in hold test experiments, it was also seen that devices with a GF membrane suffer less degradation and lower self-discharge, which implies that they can be cycled at a higher potential for longer time. This study emphasizes the need to evaluate all the elements that make up the cell and not only electrodes and electrolytes.

- Super-concentrated aqueous 27 m KAc water-in-salt (WIS) electrolyte (chapter 4) was used to increase the energy of capacitors through increasing the potential window. WIS electrolytes are characterized by their high concentration which considerably reduces the number of free water molecules, reducing its interaction and the decomposition of water at high voltages. A small increase in the potential will lead to a large increase in energy, as is reflected in the formula for the energy of a capacitor $E = \frac{1}{2} CV^2$, since the potential is squared. With the use of the 27 m KAc WIS electrolyte, we have shown that an aqueous capacitor can work at 1.8 V with a capacity retention of 74.5% by increasing the rate from 5 to 100 mV/s, as well as a retention of practically 100% of its capacitance after 10,000 cycles at 1 A/g when electrodes were prepared with the ball milling technique.

- The increase in concentration with a mixed electrolyte containing 27 m KAc + 6 m LiAc and the use of the fluorinated electrolyte 21 m LiTFSI (chapter 4) demonstrated capacitance retention of 68% and 63%, respectively, when the rate was increased from 5 to 100 mV/s in a potential window of 2 V. Also, the retained capacitance after 10,000 cycles was 22% and

94%, respectively. Finally, we concluded in discarding the 27 m KAc + 6 m LiAc electrolyte for not increasing the operational potential window of the device and the 21 m LiTFSI electrolyte for economic and environmental considerations.

- In Chapter 6, we have explored the viability of preparing hybrid capacitors in which one electrode is capacitive and the other is battery type. First, YP50 activated carbon was combined as a capacitive electrode with lithium titanium oxide (LTO) as a battery-type electrode using the organic electrolyte $LiPF_6$. A good capacitance of 30.2 F/g was obtained at 0.6 mV/s, 16.7 F/g at 5 mV/s and 7.7 F/g at 20 mV/s. Subsequently, the same strategy was applied to lithium iron phosphate (LFP), delivering 20.9 F/g at 0.1 mV/s and 10.5 F/g at 10 mV/s. s. Then, the super-concentrated aqueous electrolyte (WIS) 32 m KAc + 6 m LiAc was implemented into the hybrid device, resulting in a very high capacitance of 52.3 F/g at 0.1 m V/s and 13.3 F/g at 10 mV/s. Using the dependence between the current and the scanning speed $i=av^b$, it was possible to separate the capacitive processes from the faradaic ones for a given cell. In capacitive processes, b tends to 1 (double-layer type) and, in faradaic processes, b tends to 0.5 (battery type). A control cell was prepared with LFP electrode (battery type) versus Li metal (half-cell configuration) in 1 M $LiPF_6$ organic electrolyte, obtaining a b value of 0.55, very close to the theoretical one. Afterwards, 3 full cells were prepared with 3 different electrolytes: organic 1 M $LiPF_6$ and super-concentrated aqueous 32 m KAc and 32 m KAc + 6 m LiAc. The electrodes used were YP50 activated carbon as the negative electrode and LFP as the positive electrode. The b values were 0.68, 0.72 and 0.83 respectively, verifying that the capacitive or faradaic character of devices not only depends on the electrodes, but is also related to the electrolytes used, showing the importance of its choice in order to enhance one process or another.

The main conclusions of the second part of the thesis are related to the degradation studies of activated carbon supercapacitors in aqueous electrolytes (chapter 5):

- The forced degradation through a stress voltage of symmetric capacitors, made with activated carbon electrodes and fibre glass membrane, shows that the degradation of their components depends on the applied potential, the electrolyte, and the materials forming the electrodes and current collectors.
- Water splitting in aqueous electrolytes is an irreversible faradaic reaction with the formation of O_2 and H_2. Due to the reduction of the number of water molecules, the concentration of salts increases, which can lead to the formation of salt precipitates that reduce the capacitance by blocking the pores. The stability window of the electrolyte mainly

determines water splitting, and it has been proven that the super-concentrated electrolyte 27 m KAc can expand the potential window up to 1.8 V.

- The main degradation of activated carbon electrodes in aqueous electrolytes comes from the oxidation of the positive electrode by the oxygen generated in the decomposition of water, leading to consumption of the electrode with formation of CO_2.
- The formation and accumulation of O_2, H_2 and CO_2 at the electrodes reduce the capacitance by obstructing the access of the electrolyte to the interior of the pores, reducing the electrical contact between the electrode and the current collector, and increasing the resistance of the cell.
- Observation with XPS showed that binder degradation can be reduced with the super-concentrated electrolyte 27 m KAc, thereby improving the integrity of the electrodes.
- Composition of current collectors can reduce chemical reactivity, increase electrical conductivity, or achieve a greater overpotential for the dissociation of water. We compared stainless steel and glassy carbon current collectors, finding that glassy carbon had better performance due to its high conductivity and low impedance.

7.2 Future work

Regarding the increase in capacitance at high rates of porous activated carbon electrodes, we have verified how the mass balance, thermal treatments, the choice of membrane or the type of current collector can reduce the resistance and increase the capacitance and the potential window. The next steps to be carried out would be the reduction of the impedance of the electrodes by introducing some type of doping, such as graphene, and its integration with all other processes used, customizing them depending on the materials and electrolyte used.

Regarding the increase in the potential window with super-concentrated electrolytes, its viability has been demonstrated for electrolytes based on potassium acetate. Following the line of super-concentrated electrolytes, we propose the study of mixed aqueous/organic electrolytes to explore the expansion of the potential window without compromising safety. Another possible line of work would be the study of solid electrolytes, which would open a new path of research in the field of capacitors.

The wide range of battery-type materials opens a great field for future research regarding the use of capacitive and faradaic materials in the same device. It is worth exploring and tailoring pseudocapacitive materials for devices depending on their power or energy needs.

References

[1] U. De Antioquia and G. P. Ramos, “30-La electricidad antes de Faraday. Parte 1 The electricity before Faraday,” Diciembre, 2003. Accessed: Sep. 04, 2024. [Online]. Available: https://www.redalyc.org/articulo.oa?id=43003013

[2] S. J. Schechner and D. P. Wheatland, “The Art of Making Leyden Jars and Batteries According to Benjamin Franklin.” [Online]. Available: http://www.anb.org/articles/01/01-00089.html.

[3] F. Decker, “Volta and the ‘pile,’” Copied by permission from the “Electrochemistry Encyclopedia” (http://knowledge.electrochem.org/encycl/) on “05/09/2024.” The original material is subject to periodical changes and updates.

[4] C. S. Chi *et al.*, “Transition of hydrated oxide layer for aluminum electrolytic capacitors,” *Materials Science and Engineering: A*, vol. 448–451, pp. 314–317, Mar. 2007, doi: 10.1016/j.msea.2006.02.317.

[5] A. Wang, S. Kadam, H. Li, S. Shi, and Y. Qi, “Review on modeling of the anode solid electrolyte interphase (SEI) for lithium-ion batteries,” Dec. 01, 2018, *Nature Publishing Group*. doi: 10.1038/s41524-018-0064-0.

[6] K. Funke, “Solid State Ionics: From Michael Faraday to green energy - The European dimension,” Aug. 2013. doi: 10.1088/1468-6996/14/4/043502.

[7] A. Burke, “Ultracapacitors: why, how, and where is the technology,” 2000. [Online]. Available: www.elsevier.comrlocaterjpowsour

[8] Z. Zhang, “Comparative Study of Supercapacitor, Battery and Supercapattery,” 2023.

[9] Q. Wei *et al.*, “High-Energy and High-Power Pseudocapacitor–Battery Hybrid Sodium-Ion Capacitor with Na+ Intercalation Pseudocapacitance Anode,” *Nanomicro Lett*, vol. 13, no. 1, Jan. 2021, doi: 10.1007/s40820-020-00567-2.

[10] H. J. Becker, “Low voltage electrolytic capacitor,” Jul. 23, 1957.

[11] K. B. Li *et al.*, “Studies on the equivalent serial resistance of carbon supercapacitor,” *Electrochim Acta*, vol. 174, pp. 596–600, Jun. 2015, doi: 10.1016/j.electacta.2015.06.008.

[12] P. Simon and Y. Gogotsi, “Perspectives for electrochemical capacitors and related devices,” Nov. 01, 2020, *Nature Research*. doi: 10.1038/s41563-020-0747-z.

[13] S. Zallouz, S. Pronkin, J.-M. Le Meins, C. Pham-Huu, and C. Matei Ghimbeu, “New development in carbon-based electrodes and electrolytes for enhancement of supercapacitor performance and safety. Renewable Energy Production and Distribution Volume 2 in Advances in Re-newable Energy Technologies, Elsevier, pp,” p. 10, 2023, doi: 10.1016/B978-0-443-18439-0.00011-2ï.

[14] A. Mendhe and H. S. Panda, “A review on electrolytes for supercapacitor device,” Dec. 01, 2023, *Discover*. doi: 10.1007/s43939-023-00065-3.

[15] P. Simon and Y. Gogotsi, “Materials for electrochemical capacitors,” Nov. 16, 2008. doi: 10.1038/nmat2297.

[16] H. Helmholtz, “Ueber einige Gesetze der Vertheilung elektrischer Ströme in körperlichen Leitern, mit Anwendung auf die thierisch-elektrischen Versuche,” *Ann Phys*, vol. 165, no. 6, pp. 211–233, 1853.

[17] H. Helmholtz, “Ueber einige Gesetze der Vertheilung elektrischer Ströme in körperlichen Leitern, mit Anwendung auf die thierisch-elektrischen Versuche (Schluss.),” *Ann Phys*, vol. 165, no. 7, pp. 353–377, 1853, doi: 10.1002/andp.18531650702.

[18] H. Helmholtz, “Studien über electrische Grenzschichten,” *Ann Phys*, vol. 243, no. 7, pp. 337–382, 1879, doi: 10.1002/andp.18792430702.

[19] M. Gouy, “Sur la constitution de la charge électrique à la surface d’un électrolyte,” *J. Phys. Theor. Appl*, vol. 9, no. 1, 1910, doi: 10.1051/jphystap:019100090045700ï.

[20] H. Schmidt-Böcking, K. Reich, A. Templeton, W. Trageser, and V. Vill, “S25,” in *Otto Sterns Veröffentlichungen – Band 2*, Berlin, Heidelberg: Springer Berlin Heidelberg, 2016, pp. 197–206. doi: 10.1007/978-3-662-46962-0_20.

[21] D. C. Grahame, “THE ELECTRICAL DOUBLE LAYER AND THE THEORY OF ELECTROCAPILLARITY,” 1947. [Online]. Available: https://pubs.acs.org/sharingguidelines

[22] J. O. Bockris, M. A. V Devanathan, and K. Muller, "On the structure of charged interfaces," *Proc R Soc Lond A Math Phys Sci*, vol. 274, no. 1356, pp. 55–79, Jun. 1963, [Online]. Available: https://royalsocietypublishing.org/

[23] M. Thommes *et al.*, "Physisorption of gases, with special reference to the evaluation of surface area and pore size distribution (IUPAC Technical Report)," *Pure and Applied Chemistry*, vol. 87, no. 9–10, pp. 1051–1069, Oct. 2015, doi: 10.1515/pac-2014-1117.

[24] J. Chmiola, G. Yushin, Y. Gogotsi, C. Portet, P. Simon, and P. L. Taberna, "Anomalous Increase in Carbon Capacitance at Pore Sizes Less Than 1 Nanometer," *Science (1979)*, vol. 313, no. 5794, pp. 1760–1763, Sep. 2006, doi: 10.1126/science.1132195.

[25] J. Huang, B. G. Sumpter, and V. Meunier, "A universal model for nanoporous carbon supercapacitors applicable to diverse pore regimes, carbon materials, and electrolytes," *Chemistry - A European Journal*, vol. 14, no. 22, pp. 6614–6626, Jul. 2008, doi: 10.1002/chem.200800639.

[26] V. L. Martins *et al.*, "An overview on the development of electrochemical capacitors and batteries – part I," *An Acad Bras Cienc*, vol. 92, no. 2, pp. 1–28, 2020, doi: 10.1590/0001-3765202020200796.

[27] T. Brousse, D. Bélanger, and J. W. Long, "To Be or Not To Be Pseudocapacitive?," *J Electrochem Soc*, vol. 162, no. 5, pp. A5185–A5189, 2015, doi: 10.1149/2.0201505jes.

[28] B. E. Conway, "Conway_1991_J._Electrochem._Soc._138_1539," *J. Electrochem. Soc.*, vol. 138, no. 1539, 1991.

[29] B. E. Conway, *Electrochemical Supercapacitors: Scientific Fundamentals and Technological Applications*. kluwer-Academic, 1999.

[30] V. Augustyn, P. Simon, and B. Dunn, "Pseudocapacitive oxide materials for high-rate electrochemical energy storage," *Energy Environ Sci*, vol. 7, no. 5, p. 1597, 2014, doi: 10.1039/c3ee44164d.

[31] J. Wang *et al.*, "Pseudocapacitive materials for electrochemical capacitors: From rational synthesis to capacitance optimization," Jan. 01, 2017, *Oxford University Press*. doi: 10.1093/nsr/nww072.

[32] N. R. Chodankar *et al.*, “True Meaning of Pseudocapacitors and Their Performance Metrics: Asymmetric versus Hybrid Supercapacitors,” Sep. 01, 2020, *Wiley-VCH Verlag*. doi: 10.1002/smll.202002806.

[33] R. Borah, F. R. Hughson, J. Johnston, and T. Nann, “On battery materials and methods,” Jun. 01, 2020, *Elsevier Ltd*. doi: 10.1016/j.mtadv.2019.100046.

[34] Z. Liu, X. Li, H. Zhang, K. Huang, and Y. Yu, “Are solid-state batteries absolutely more environmentally friendly compared to traditional batteries-analyzing from the footprint family viewpoint,” *J Clean Prod*, vol. 447, p. 141452, Apr. 2024, doi: 10.1016/j.jclepro.2024.141452.

[35] P. L. Stigliano *et al.*, “A physico-chemical investigation of highly concentrated potassium acetate solutions towards applications in electrochemistry,” *Physical Chemistry Chemical Physics*, vol. 23, no. 2, pp. 1139–1145, Jan. 2021, doi: 10.1039/d0cp04151c.

[36] M. Thommes *et al.*, “Physisorption of gases, with special reference to the evaluation of surface area and pore size distribution (IUPAC Technical Report),” *Pure and Applied Chemistry*, vol. 87, no. 9–10, pp. 1051–1069, Oct. 2015, doi: 10.1515/pac-2014-1117.

[37] S. Achari, A. S. Rajalakshmi, S. Jayasree, & Raichel, and M. Lopez, “Adsorption of p-nitrophenol from aqueous solutions by Zr 4+ activated carbon: Adsorption isotherm studies,” 2018.

[38] A. N. Popova, “Crystallographic analysis of graphite by X-Ray diffraction,” *Coke and Chemistry*, vol. 60, no. 9, pp. 361–365, Sep. 2017, doi: 10.3103/S1068364X17090058.

[39] T. Degen, M. Sadki, E. Bron, U. König, and G. Nénert, “The high score suite,” in *Powder Diffraction*, Cambridge University Press, Dec. 2014, pp. S13–S18. doi: 10.1017/S0885715614000840.

[40] L. Abbas, L. Bih, K. Yamni, A. Elyahyaouy, A. El Attaoui, and Z. Ramzi, “Graphite Carbone Structure,” *Crystal Structure Theory and Applications*, vol. 12, no. 01, pp. 1–10, 2024, doi: 10.4236/csta.2024.121001.

[41] B. S. Girgis, Y. M. Temerk, M. M. Gadelrab, and I. D. Abdullah, “X-ray Diffraction Patterns of Activated Carbons Prepared under Various Conditions,” 2007.

[42] B. S. Girgis, Y. M. Temerk, M. M. Gadelrab, and I. D. Abdullah, “X-ray Diffraction Patterns of Activated Carbons Prepared under Various Conditions,” 2007.

[43] S. M. Lee, S. H. Lee, and J. S. Roh, “Analysis of activation process of carbon black based on structural parameters obtained by XRD analysis,” *Crystals (Basel)*, vol. 11, no. 2, pp. 1–11, Feb. 2021, doi: 10.3390/cryst11020153.

[44] F. Song, Q. Wang, and T. Wang, “The effects of crystallinity on the mechanical properties and the limiting PV (pressure×velocity) value of PTFE,” *Tribol Int*, vol. 93, pp. 1–10, Jan. 2016, doi: 10.1016/j.triboint.2015.09.017.

[45] G. Ramer and B. Lendl, “Attenuated Total Reflection Fourier Transform Infrared Spectroscopy,” in *Encyclopedia of Analytical Chemistry*, Wiley, 2013. doi: 10.1002/9780470027318.a9287.

[46] Morsch et al., “ORGANIC CHEMISTRY LibreTexts.” [Online]. Available: https://LibreTexts.org

[47] E. Fuente, J. A. Menéndez, M. A. Díez, D. Suárez, and M. A. Montes-Morán, “Infrared spectroscopy of carbon materials: A quantum chemical study of model compounds,” *Journal of Physical Chemistry B*, vol. 107, no. 26, pp. 6350–6359, Jul. 2003, doi: 10.1021/jp027482g.

[48] J. Piwowarczyk, R. Jedrzejewski, D. Moszyński, K. Kwiatkowski, A. Niemczyk, and J. Baranowska, “XPS and FTIR studies of polytetrafluoroethylene thin films obtained by physical methods,” *Polymers (Basel)*, vol. 11, no. 10, Oct. 2019, doi: 10.3390/polym11101629.

[49] F. A. Stevie and C. L. Donley, “Introduction to x-ray photoelectron spectroscopy,” *Journal of Vacuum Science & Technology A: Vacuum, Surfaces, and Films*, vol. 38, no. 6, Dec. 2020, doi: 10.1116/6.0000412.

[50] D. J. Morgan, “Comments on the XPS Analysis of Carbon Materials,” *Journal of Carbon Research*, vol. 7, no. 3, p. 51, Jul. 2021, doi: 10.3390/c7030051.

[51] H. Kahlert, “Reference electrodes,” in *Electroanalytical Methods: Guide to Experiments and Applications*, Springer Berlin Heidelberg, 2010, pp. 291–308. doi: 10.1007/978-3-642-02915-8_15.

[52] N. Elgrishi, K. J. Rountree, B. D. McCarthy, E. S. Rountree, T. T. Eisenhart, and J. L. Dempsey, “A Practical Beginner’s Guide to Cyclic Voltammetry,” *J Chem Educ*, vol. 95, no. 2, pp. 197–206, Feb. 2018, doi: 10.1021/acs.jchemed.7b00361.

[53] M. D. Stoller and R. S. Ruoff, “Best practice methods for determining an electrode material’s performance for ultracapacitors,” 2010. doi: 10.1039/c0ee00074d.

[54] J. Zhao and A. F. Burke, “Review on supercapacitors: Technologies and performance evaluation,” Aug. 01, 2021, *Elsevier B.V.* doi: 10.1016/j.jechem.2020.11.013.

[55] M. Van Haeverbeke, M. Stock, and B. De Baets, “Equivalent Electrical Circuits and Their Use Across Electrochemical Impedance Spectroscopy Application Domains,” *IEEE Access*, vol. 10, pp. 51363–51379, 2022, doi: 10.1109/ACCESS.2022.3174067.

[56] R. Drummond, S. Zhao, D. A. Howey, and S. R. Duncan, “Circuit synthesis of electrochemical supercapacitor models,” *J Energy Storage*, vol. 10, pp. 48–55, Apr. 2017, doi: 10.1016/j.est.2016.11.003.

[57] “Carbon materials,” https://nanografi.com/blog/carbon-nanofibers-for-superior-conductivity-in-supercapacitors/?srsltid=AfmBOopOZPhLxBtS3xBGr93UqvMQJKoI0aR56xQg2_KUbsPbZyPbG5Jc.

[58] CEST, “From biomass to supercapacitor,” YouTube. Accessed: Sep. 10, 2024. [Online]. Available: https://youtu.be/b3C0kheckCM?si=fMHcyMXHd3cGyZkQ

[59] J. M. Miller, J.-N.-J. Miller, and R. Smith, “ULTRACAPACITOR ASSISTED ELECTRIC DRIVES FOR TRANSPORTATION.” [Online]. Available: www.maxwell.com

[60] S. Ahankari, D. Lasrado, and R. Subramaniam, “Advances in materials and fabrication of separators in supercapacitors,” Feb. 07, 2022, *Royal Society of Chemistry*. doi: 10.1039/d1ma00599e.

[61] “Film Capacitors General technical information,” 2018.

[62] “3003279.2_Final-DS_New-2.7V-3000F-Cell_20210406”.

[63] “KEMET Supercapacitors FC series.” [Online]. Available: www.kemet.com

[64] R. Chen *et al.*, "A Comparative Review of Electrolytes for Organic-Material-Based Energy-Storage Devices Employing Solid Electrodes and Redox Fluids," May 08, 2020, *Wiley-VCH Verlag*. doi: 10.1002/cssc.201903382.

[65] D. C. U. Sirimanne, N. Kularatna, and N. Arawwawala, "Electrical Performance of Current Commercial Supercapacitors and Their Future Applications," *Electronics (Switzerland)*, vol. 12, no. 11, Jun. 2023, doi: 10.3390/electronics12112465.

[66] Z. Lin, D. Li, and Y. Zou, "Energy efficiency of lithium-ion batteries: Influential factors and long-term degradation," *J Energy Storage*, vol. 74, Dec. 2023, doi: 10.1016/j.est.2023.109386.

[67] N. Somakettarin, A. Pichetjamroen, N. Teerakawanich, P. Chindamanee, C. Chupong, and C. Suppitaksakul, "An evaluation of battery energy efficiency with multi-step sampling rate recording for DC data loggers," *Energy Reports*, vol. 9, pp. 866–872, Mar. 2023, doi: 10.1016/j.egyr.2022.11.103.

[68] H. Keshan, J. Thornburg, and T. Selim Ustun, "Comparison of Lead-Acid and Lithium Ion Batteries for Stationary Storage in Off-Grid Energy Systems," 2016.

[69] B. Andres, A. C. Engström, N. Blomquist, S. Forsberg, C. Dahlström, and H. Olin, "Electrode mass balancing as an inexpensive and simple method to increase the capacitance of electric double-layer capacitors," *PLoS One*, vol. 11, no. 9, Sep. 2016, doi: 10.1371/journal.pone.0163146.

[70] S. Vaquero, J. Palma, M. Anderson, and R. Marcilla, "Mass-Balancing of Electrodes as a Strategy to Widen the Operating Voltage Window of Carbon/Carbon Supercapacitors in Neutral Aqueous Electrolytes," 2013. [Online]. Available: www.electrochemsci.org

[71] S. Dsoke, B. Fuchs, E. Gucciardi, and M. Wohlfahrt-Mehrens, "The importance of the electrode mass ratio in a Li-ion capacitor based on activated carbon and Li4Ti5O12," *J Power Sources*, vol. 282, pp. 385–393, May 2015, doi: 10.1016/j.jpowsour.2015.02.079.

[72] R. Lu, A. Yang, Y. Xue, L. Xu, and C. Zhu, "Analysis of the key factors affecting the energy efficiency of batteries in electric vehicle," *World Electric Vehicle Journal*, vol. 4, pp. 9–13, Nov. 2010.

[73] J. J. Quintana, A. Ramos, M. Diaz, and I. Nuez, “Energy efficiency analysis as a function of the working voltages in supercapacitors,” *Energy*, vol. 230, Sep. 2021, doi: 10.1016/j.energy.2021.120689.

[74] R. Farma *et al.*, “Physical and Electrochemical Properties of Supercapacitor Electrodes Derived from Carbon Nanotube and Biomass Carbon,” 2013. [Online]. Available: www.electrochemsci.org

[75] W. G. Nunes, B. G. A. Freitas, R. M. Beraldo, R. M. Filho, L. M. Da Silva, and H. Zanin, “A rational experimental approach to identify correctly the working voltage window of aqueous-based supercapacitors,” *Sci Rep*, vol. 10, no. 1, Dec. 2020, doi: 10.1038/s41598-020-75851-7.

[76] N. Ehteshami, L. Ibing, L. Stolz, M. Winter, and E. Paillard, “Ethylene carbonate-free electrolytes for Li-ion battery: Study of the solid electrolyte interphases formed on graphite anodes,” *J Power Sources*, vol. 451, Mar. 2020, doi: 10.1016/j.jpowsour.2020.227804.

[77] F. Barzegar, D. Y. Momodu, O. O. Fashedemi, A. Bello, J. K. Dangbegnon, and N. Manyala, “Investigation of different aqueous electrolytes on the electrochemical performance of activated carbon-based supercapacitors,” *RSC Adv*, vol. 5, no. 130, pp. 107482–107487, Dec. 2015, doi: 10.1039/c5ra21962k.

[78] X. Díez-Betriu *et al.*, “Raman spectroscopy for the study of reduction mechanisms and optimization of conductivity in graphene oxide thin films,” *J Mater Chem C Mater*, vol. 1, no. 41, pp. 6905–6912, Nov. 2013, doi: 10.1039/c3tc31124d.

[79] H. Gul, A. ul H. A. Shah, and S. Bilal, “Achieving ultrahigh cycling stability and extended potential window for supercapacitors through asymmetric combination of conductive polymer nanocomposite and activated carbon,” *Polymers (Basel)*, vol. 11, no. 10, Oct. 2019, doi: 10.3390/polym11101678.

[80] F. Andreatta *et al.*, “Degradation of PTFE non-stick coatings for application in the food service industry,” *Eng Fail Anal*, vol. 115, Sep. 2020, doi: 10.1016/j.engfailanal.2020.104652.

[81] M. C. Biesinger, “Accessing the robustness of adventitious carbon for charge referencing (correction) purposes in XPS analysis: Insights from a multi-user facility data review,” *Appl Surf Sci*, vol. 597, Sep. 2022, doi: 10.1016/j.apsusc.2022.153681.

[82] J. H. Zhou *et al.*, “Characterization of surface oxygen complexes on carbon nanofibers by TPD, XPS and FT-IR,” *Carbon N Y*, vol. 45, no. 4, pp. 785–796, Apr. 2007, doi: 10.1016/j.carbon.2006.11.019.

[83] K. Fujitani *et al.*, “In situ synchrotron X-ray scission of polytetrafluoroethylene chains and elucidation of dry etching,” *Heliyon*, vol. 9, no. 5, May 2023, doi: 10.1016/j.heliyon.2023.e15794.

[84] O. Wijaya *et al.*, “A gamma fluorinated ether as an additive for enhanced oxygen activity in Li-O2 batteries,” *J Mater Chem A Mater*, vol. 3, no. 37, pp. 19061–19067, May 2015, doi: 10.1039/c5ta03439f.

[85] H. Wu, M. Genovese, K. Ton, and K. Lian, “A Comparative Study of Activated Carbons from Liquid to Solid Polymer Electrolytes for Electrochemical Capacitors,” *J Electrochem Soc*, vol. 166, no. 6, pp. A821–A828, 2019, doi: 10.1149/2.0141906jes.

[86] Z. Zhu *et al.*, “Effects of various binders on supercapacitor performances,” *Int J Electrochem Sci*, vol. 11, no. 10, pp. 8270–8279, 2016, doi: 10.20964/2016.10.04.

[87] Y. Gao *et al.*, “Electrochemical performance of Ti3C2 supercapacitors in KOH electrolyte,” *Journal of Advanced Ceramics*, vol. 4, no. 2, pp. 130–134, Jun. 2015, doi: 10.1007/s40145-015-0143-3.

[88] A. Electrolyte, “Celgard® 3501 Monolayer Microporous Membrane Primary Applications Technical Data.” [Online]. Available: www.celgard.com/literature

[89] E. Warburg, “Ueber das Verhalten sogenannter unpolarisirbarer Elektroden gegen Wechselstrom,” *Ann Phys*, vol. 303, no. 3, pp. 493–499, 1899.

[90] D. Weingarth, A. Foelske-Schmitz, and R. Kötz, “Cycle versus voltage hold - Which is the better stability test for electrochemical double layer capacitors?,” *J Power Sources*, vol. 225, pp. 84–88, Mar. 2013, doi: 10.1016/j.jpowsour.2012.10.019.

[91] S. Zhang *et al.*, “Nanocomposite polymer membrane derived from nano TiO2-PMMA and glass fiber nonwoven: High thermal endurance and cycle stability in lithium ion battery applications,” *J Mater Chem A Mater*, vol. 3, no. 34, pp. 17697–17703, Jul. 2015, doi: 10.1039/c5ta02781k.

[92] H. Zhang, X. Liu, H. Li, I. Hasa, and S. Passerini, “Challenges and Strategies for High-Energy Aqueous Electrolyte Rechargeable Batteries,” Jan. 11, 2021, *Wiley-VCH Verlag*. doi: 10.1002/anie.202004433.

[93] Y. Lu, Z. Gao, Q. Yang, C. Xiong, and G. H. Hu, “3.6 V high-voltage symmetrical supercapacitor based on reduced graphene oxide/polythiophene aerogels with uniform dispersion,” *J Energy Storage*, vol. 72, Nov. 2023, doi: 10.1016/j.est.2023.108224.

[94] Z. Xiong *et al.*, “A High-Performance Dual-Ion Battery-Supercapacitor Hybrid Device Based on LiCl in Ion Liquid Dual-Salt Electrolyte,” *Adv Energy Mater*, vol. 12, no. 7, Feb. 2022, doi: 10.1002/aenm.202103226.

[95] L. Suo *et al.*, “‘Water-in-salt’ electrolyte enables high-voltage aqueous lithium-ion chemistries,” *Science (1979)*, vol. 350, no. 6263, pp. 938–943, 2015, doi: 10.1126/science.aab1595.

[96] B. Huang *et al.*, “Cation- and pH-Dependent Hydrogen Evolution and Oxidation Reaction Kinetics,” *JACS Au*, vol. 1, no. 10, pp. 1674–1687, Oct. 2021, doi: 10.1021/jacsau.1c00281.

[97] P. Banerjee and B. Bagchi, “Ions’ motion in water,” May 21, 2019, *American Institute of Physics Inc.* doi: 10.1063/1.5090765.

[98] P. Lemaire *et al.*, “Probing the Electrode–Electrolyte Interface of a Model K-Ion Battery Electrode The Origin of Rate Capability Discrepancy between Aqueous and Non-Aqueous Electrolytes,” *ACS Appl Mater Interfaces*, vol. 14, pp. 20835–20847, 2022, doi: 10.1021/acsami.1c24111.

[99] T. Sun, S. Zheng, H. Du, and Z. Tao, “Synergistic Effect of Cation and Anion for Low-Temperature Aqueous Zinc-Ion Battery,” *Nanomicro Lett*, vol. 13, no. 1, Dec. 2021, doi: 10.1007/s40820-021-00733-0.

[100] K. Amine, Q. Wang, D. R. Vissers, Z. Zhang, N. A. A. Rossi, and R. West, “Novel silane compounds as electrolyte solvents for Li-ion batteries,” *Electrochem commun*, vol. 8, no. 3, pp. 429–433, Mar. 2006, doi: 10.1016/j.elecom.2005.12.017.

[101] M. R. Lukatskaya *et al.*, “Concentrated mixed cation acetate ‘water-in-salt’ solutions as green and low-cost high voltage electrolytes for aqueous batteries,” *Energy Environ Sci*, vol. 11, no. 10, pp. 2876–2883, Oct. 2018, doi: 10.1039/c8ee00833g.

[102] H. Avireddy *et al.*, “Stable high-voltage aqueous pseudocapacitive energy storage device with slow self-discharge,” *Nano Energy*, vol. 64, 2019, doi: 10.1016/j.nanoen.2019.103961.

[103] D. P. Leonard, Z. Wei, G. Chen, F. Du, and X. Ji, “Water-in-Salt Electrolyte for Potassium-Ion Batteries,” *ACS Energy Lett*, vol. 3, no. 2, pp. 373–374, 2018, doi: 10.1021/acsenergylett.8b00009.

[104] M. Amiri and D. Bélanger, “Physicochemical and Electrochemical Properties of Water-in-Salt Electrolytes,” Jun. 21, 2021, *John Wiley and Sons Inc*. doi: 10.1002/cssc.202100550.

[105] M. Zhou, Z. Bo, and K. Ostrikov, “Challenges and prospects of high-voltage aqueous electrolytes for energy storage applications,” *Physical Chemistry Chemical Physics*, vol. 24, no. 35, pp. 20674–20688, Aug. 2022, doi: 10.1039/d2cp02795j.

[106] A. C. Lazanas and M. I. Prodromidis, “Electrochemical Impedance Spectroscopy─A Tutorial,” Jun. 21, 2023, *American Chemical Society*. doi: 10.1021/acsmeasuresciau.2c00070.

[107] Y. He *et al.*, “Capacitive mechanism of oxygen functional groups on carbon surface in supercapacitors,” *Electrochim Acta*, vol. 282, pp. 618–625, Aug. 2018, doi: 10.1016/j.electacta.2018.06.103.

[108] “SCC Series High Capacitance Cylindrical SuperCapacitors QUALITY INSPECTIONS.” [Online]. Available: www.kyocera-avx.com/disclaimer/

[109] W. Deng *et al.*, “Li/K mixed superconcentrated aqueous electrolyte enables high-performance hybrid aqueous supercapacitors,” *Energy Storage Mater*, vol. 20, pp. 373–379, Jul. 2019, doi: 10.1016/j.ensm.2018.10.023.

[110] P. Lannelongue *et al.*, “‘Water-in-Salt’ for Supercapacitors: A Compromise between Voltage, Power Density, Energy Density and Stability,” *J Electrochem Soc*, vol. 165, no. 3, pp. A657–A663, 2018, doi: 10.1149/2.0951803jes.

[111] Q. Zhang, J. Rong, D. Ma, and B. Wei, “The governing self-discharge processes in activated carbon fabric-based supercapacitors with different organic electrolytes,” *Energy Environ Sci*, vol. 4, no. 6, pp. 2152–2159, Jun. 2011, doi: 10.1039/c0ee00773k.

[112] P. Zhu, D. Gastol, J. Marshall, R. Sommerville, V. Goodship, and E. Kendrick, “A review of current collectors for lithium-ion batteries,” Feb. 15, 2021, *Elsevier B.V.* doi: 10.1016/j.jpowsour.2020.229321.

[113] P. Ratajczak, K. Jurewicz, P. Skowron, Q. Abbas, and F. Béguin, “Effect of accelerated ageing on the performance of high voltage carbon/carbon electrochemical capacitors in salt aqueous electrolyte,” *Electrochim Acta*, vol. 130, pp. 344–350, Jun. 2014, doi: 10.1016/j.electacta.2014.02.140.

[114] Q. Abbas *et al.*, “Strategies to Improve the Performance of Carbon/Carbon Capacitors in Salt Aqueous Electrolytes,” *J Electrochem Soc*, vol. 162, no. 5, pp. A5148–A5157, 2015, doi: 10.1149/2.0241505jes.

[115] M. He, K. Fic, E. Frackowiak, P. Novák, and E. J. Berg, “Ageing phenomena in high-voltage aqueous supercapacitors investigated by in situ gas analysis,” *Energy Environ Sci*, vol. 9, no. 2, pp. 623–633, Feb. 2016, doi: 10.1039/c5ee02875b.

[116] E. Pameté *et al.*, “The Many Deaths of Supercapacitors: Degradation, Aging, and Performance Fading,” Aug. 04, 2023, *John Wiley and Sons Inc*. doi: 10.1002/aenm.202301008.

[117] A. Pourramazan, S. Saffari, and A. Barghandan, “Capacitor Bank Used in Distribution Power Systems,” *International Journal of Innovative Research in Electrical, Electronics, Instrumentation and Control Engineering ISO*, vol. 3297, no. 2, pp. 2321–5526, 2007, doi: 10.17148/IJIREE.

[118] A. B. Temsamani, S. Kauffmann, S. Helsen, T. Gaens, and V. Driesen, “Physics-of-Failure (PoF) methodology for qualification and lifetime assessment of supercapacitors for industrial applications,” *Microelectronics Reliability*, vol. 88–90, pp. 54–60, Sep. 2018, doi: 10.1016/j.microrel.2018.06.084.

[119] F. H. Gandoman, E. M. Ahmed, Z. M. Ali, M. Berecibar, A. F. Zobaa, and S. H. E. Abdel Aleem, “Reliability evaluation of lithium-ion batteries for e-mobility applications from practical and technical perspectives: A case study,” *Sustainability (Switzerland)*, vol. 13, no. 21, Nov. 2021, doi: 10.3390/su132111688.

[120] T. Hu *et al.*, “Progress in the Regulation of Electrode/Electrolyte Interfacial Reactions toward High-voltage Aqueous Hybrid Capacitors,” May 01, 2021, *John Wiley and Sons Inc*. doi: 10.1002/batt.202000323.

[121] M. He, K. Fic, E. Frackowiak, P. Novák, and E. J. Berg, “Ageing phenomena in high-voltage aqueous supercapacitors investigated by in situ gas analysis,” *Energy Environ Sci*, vol. 9, no. 2, pp. 623–633, Feb. 2016, doi: 10.1039/c5ee02875b.

[122] C. Neto *et al.*, “Exploring the Carbon/Electrolyte Interface in Supercapacitors Operating in Highly Concentrated Aqueous Electrolytes,” *ACS Appl Mater Interfaces*, vol. 14, no. 39, pp. 44405–44418, Oct. 2022, doi: 10.1021/acsami.2c12010.

[123] A. Oz, D. Gelman, E. Goren, N. Shomrat, S. Baltianski, and Y. Tsur, “A novel approach for supercapacitors degradation characterization,” *J Power Sources*, vol. 355, pp. 74–82, 2017, doi: 10.1016/j.jpowsour.2017.04.048.

[124] W. Liu *et al.*, “Thermal characteristic and performance influence of a hybrid supercapacitor,” *J Energy Storage*, vol. 53, Sep. 2022, doi: 10.1016/j.est.2022.105188.

[125] Y. Dandeville, P. Guillemet, Y. Scudeller, O. Crosnier, L. Athouel, and T. Brousse, “Measuring time-dependent heat profiles of aqueous electrochemical capacitors under cycling,” *Thermochim Acta*, vol. 526, no. 1–2, pp. 1–8, Nov. 2011, doi: 10.1016/j.tca.2011.07.027.

[126] O. Munteshari, J. Lau, A. Krishnan, B. Dunn, and L. Pilon, “Isothermal calorimeter for measurements of time-dependent heat generation rate in individual supercapacitor electrodes,” *J Power Sources*, vol. 374, pp. 257–268, Jan. 2018, doi: 10.1016/j.jpowsour.2017.11.012.

[127] S. T. Bashir, L. Yang, J. J. Liggat, and J. L. Thomason, “Kinetics of dissolution of glass fibre in hot alkaline solution,” *J Mater Sci*, vol. 53, no. 3, pp. 1710–1722, Feb. 2018, doi: 10.1007/s10853-017-1627-z.

[128] M. Sun, X. Gao, Z. Zhang, C. Zou, D. Xin, and G. Geng, “Stepwise dissolution of silica surface in alkaline solution revealed by molecular modeling,” *Journal of the American Ceramic Society*, vol. 106, no. 11, pp. 6586–6601, Nov. 2023, doi: 10.1111/jace.19355.

[129] S. Saravanan and R. S. Dubey, “Synthesis of SiO 2 Nanoparticles by Sol-Gel Method and Their Optical and Structural Properties,” 2020.

[130] D. Cuhadaroglu and O. A. Uygun, “Production and characterization of activated carbon from a bituminous coal by chemical activation,” *Afr J Biotechnol*, vol. 7, no. 20, pp. 3703–3710, 2008, [Online]. Available: http://www.academicjournals.org/AJB

[131] S. Qiu, Y. Xu, X. Li, S. K. Sandstrom, X. Wu, and X. Ji, "Reinforced potassium and ammonium storage of the polyimide anode in acetate-based water-in-salt electrolytes," *Electrochem commun*, vol. 122, Jan. 2021, doi: 10.1016/j.elecom.2020.106880.

[132] J. H. Zhou *et al.*, "Characterization of surface oxygen complexes on carbon nanofibers by TPD, XPS and FT-IR," *Carbon N Y*, vol. 45, no. 4, pp. 785–796, Apr. 2007, doi: 10.1016/j.carbon.2006.11.019.

[133] C. Saka, "BET, TG-DTG, FT-IR, SEM, iodine number analysis and preparation of activated carbon from acorn shell by chemical activation with ZnCl2," *J Anal Appl Pyrolysis*, vol. 95, pp. 21–24, 2012, doi: 10.1016/j.jaap.2011.12.020.

[134] G. Zhou, C. Xu, W. Cheng, Q. Zhang, and W. Nie, "Effects of Oxygen Element and Oxygen-Containing Functional Groups on Surface Wettability of Coal Dust with Various Metamorphic Degrees Based on XPS Experiment," *J Anal Methods Chem*, vol. 2015, 2015, doi: 10.1155/2015/467242.

[135] H. Okada, H. Yamada, A. Yoshida, and A. Wakahara, "BL8A Investigation of Synchrotron Radiation Induced Etching of Polytetrafluoroethylene," 2003. [Online]. Available: https://www.researchgate.net/publication/242772527

[136] S. P. Asrafali, T. Periyasamy, S. C. Kim, and J. W. Lee, "Enhanced Wettability and Adhesive Property of PTFE through Surface Modification with Fluorinated Compounds," *Materials*, vol. 17, no. 13, Jul. 2024, doi: 10.3390/ma17133051.

[137] D. Pantea, H. Darmstadt, S. Kaliaguine, and C. Roy, "Electrical conductivity of conductive carbon blacks: Influence of surface chemistry and topology," *Appl Surf Sci*, vol. 217, no. 1–4, pp. 181–193, Jul. 2003, doi: 10.1016/S0169-4332(03)00550-6.

[138] M. Y. Bashouti, Y. Paska, S. R. Puniredd, T. Stelzner, S. Christiansen, and H. Haick, "Silicon nanowires terminated with methyl functionalities exhibit stronger Si-C bonds than equivalent 2D surfaces," *Physical Chemistry Chemical Physics*, vol. 11, no. 20, pp. 3845–3848, 2009, doi: 10.1039/b820559k.

[139] B. H. Park, M. H. Lee, S. B. Kim, and Y. M. Jo, "Evaluation of the surface properties of PTFE foam coating filter media using XPS and contact angle measurements," *Appl Surf Sci*, vol. 257, no. 8, pp. 3709–3716, Feb. 2011, doi: 10.1016/j.apsusc.2010.11.116.

[140] Y. Yi *et al.*, “Electrochemical corrosion of a glassy carbon electrode,” *Catal Today*, vol. 295, pp. 32–40, Oct. 2017, doi: 10.1016/j.cattod.2017.07.013.

[141] M. Z. Iqbal and U. Aziz, “Supercapattery: Merging of battery-supercapacitor electrodes for hybrid energy storage devices,” Feb. 01, 2022, *Elsevier Ltd*. doi: 10.1016/j.est.2021.103823.

[142] A. Shellikeri *et al.*, “Hybrid Lithium-ion Capacitor with LiFePO4/AC Composite Cathode-Long Term Cycle Life Study, Rate Effect and Charge Sharing Analysis,” 2018.

[143] D. Cericola, P. Novák, A. Wokaun, and R. Kötz, “Hybridization of electrochemical capacitors and rechargeable batteries: An experimental analysis of the different possible approaches utilizing activated carbon, Li4Ti5O12 and LiMn2O 4,” *J Power Sources*, vol. 196, no. 23, pp. 10305–10313, Dec. 2011, doi: 10.1016/j.jpowsour.2011.07.032.

[144] Z. Xiong *et al.*, “A High-Performance Dual-Ion Battery-Supercapacitor Hybrid Device Based on LiCl in Ion Liquid Dual-Salt Electrolyte,” *Adv Energy Mater*, vol. 12, no. 7, Feb. 2022, doi: 10.1002/aenm.202103226.

[145] L. Zhang, J. D. Zhang, and B. J. Xu, “High-rate performance of polyethylene glycol-modified Li4Ti5O12 anode materials,” *Results Phys*, vol. 19, Dec. 2020, doi: 10.1016/j.rinp.2020.103583.

[146] L. Persi, F. Croce, and B. Scrosati, “A LiTi 2 O 4-LiFePO 4 novel lithium-ion polymer battery,” *Electrochem commun*, vol. 4, pp. 92–95, 2002, [Online]. Available: www.elsevier.com/locate/elecom

[147] S. Kiani, H. Gharibi, S. Javadian, M. Zhiani, and H. Kashani, “The effect of the SEI layer on the electrochemical impedance in the graphite/ Li[Ni0.5Mn0.3Co0.2]O2 lithium-ion full cells,” *Appl Surf Sci*, vol. 633, Oct. 2023, doi: 10.1016/j.apsusc.2023.157638.

[148] - C Liu, W. G. Pell, B. E. Conway, and S. L. Roberson, “Behavior of Molybdenum Nitrides as Materials for Electrochemical Capacitors Comparison with Ruthenium Oxide,” 1998.

[149] H. Lindström *et al.*, “Li + Ion Insertion in TiO 2 (Anatase). 2. Voltammetry on Nanoporous Films,” 1997. [Online]. Available: https://pubs.acs.org/sharingguidelines